EXPERIMENTAL STUDIES OF SCALAR TRANSPORT AND MIXING IN A TURBULENT SHEAR FLOW

by

Amir Behnamian

Thesis submitted to the
Faculty of Graduate and Postdoctoral Studies
in partial fulfillment of the requirements
for the Doctorate in Philosophy degree in Mechanical Engineering

Ottawa-Carleton Institute for Mechanical and Aerospace Engineering
Faculty of Engineering
University of Ottawa

Abstract

High resolution, multi-sensor, hot/cold-wire measurements were made in passively heated, uniformly sheared turbulence in a wind-tunnel. Measurements were focused on terms that are important for modelling of the scalar probability density function (PDF) equation. Unlike previous studies, which considered a single combination of velocity and scalar fields at a time, in this study three different scalar fields were investigated in the same nearly homogeneous turbulence with three passively superimposed temperature fields, namely a transversely homogeneous temperature field with a uniform mean gradient, and two inhomogeneous temperature fields, the plume of a heated line source and a thermal mixing layer. The use of the same uniformly sheared flow allowed the isolation of the effects of scalar inhomogeneity and initial conditions by evaluating the results in the three scalar fields. Thus, the measurements covered a wide range of scalar field conditions and set the ground for a conclusive comparison. For the homogeneous scalar field, results conformed with the literature: the scalar PDF was essentially Gaussian; the conditional expectations of velocities upon the scalar value were approximately linear; and the conditional expectation of the scalar dissipation rate upon the scalar value was mildly anisotropic and had a shape that was similar to those of any of its three parts, which justifies the use of the streamwise part as a surrogate for the total. All these properties behaved very differently in two inhomogeneous scalar fields, the thermal mixing layer and the plume of a heated line source: the scalar PDFs were distinctly sub-Gaussian; the conditional velocity expectations were non-linear functions of the scalar value; and the conditional scalar dissipation rates were very strongly anisotropic, as well as depending on the scalar value in fashions that differed strongly from those of any of their three parts.

Acknowledgements

My most sincere thanks go to my advisor and mentor, Dr. Stavros Tavoularis. I would like to thank the staff of the University of Ottawa Mechanical Engineering Machine Shop, especially Leo Denner, John Perrins, Stan Weedmark, and Mike Burns. I would also like to thank my fellow graduate students, George Choueiri, Christina Vanderwel, Laura Haya Brown, Hussam Zahlan, Hassan Shaban, Armel Don, and Steffen Pentelow for all their friendship and the enjoyable time we spent during the past years. I also gratefully acknowledge the financial support of the Faculty of Graduate and Postdoctral Studies of University of Ottawa and the Natural Sciences and Engineering Research Council of Canada as well as Professor Tavoularis. I am grateful to Dr. Petar Vukoslavcevic for building the hot-wire/cold-wire probes in the early stage of this work. Avi Aharoni is gratefully acknowledged for his assistance in solving the technical challenges of the anemometer. Finally, I thank my wife, Golshid, for her unconditional support and love throughout these years.

Table of Contents

List of Tables

List of Figures

Nomenclature

A, B	RTD constants
A_i, B_i	modified King's law constants
A_{noz}	calibration jet nozzle exit area
c_p	specific heat of air under constant pressure
D_{ij}	turbulent diffusivities
d_w	wire/sensor diameter
E	input/output voltage
E_{th}	thermistor output voltage
H	humidity
H_{noz}	elevation difference between nozzle exit and plenum pressure tap in calibration jet
h	height of wind tunnel
F	cumulative distribution function
f	probability density function
f_k	Kolmogorov frequency
g	gravitational acceleration
I	current
I_p	cold-wire probe current
k	turbulent kinetic energy
L	representative lengthscale
$L_{\alpha\alpha,\beta}$	integral length scale
l_w	wire/sensor length
M	separation distance between the plates of shear generator
m_{ij}	turbulence anisotropy
n	order of moments
n_i	power constants of modified King's law

P	pressure
P_d	partial pressure of dry air
P_v	partial pressure of water vapour
p	pressure fluctuation
R	resistance
R_0	resistance at 0 °C
R_d	specific gas constant
R_f	flux Richardson number
R_g, R_s	amplifier resistances of cold-wire circuitry
Re	Reynolds number
$Re_{\lambda_{11}}$	Reynolds number based on the Taylor microscale
S^*	shear-rate parameter
T	temperature
T_h	temperature rise in thermal mixing layer
T_m	maximum temperature in the plume of a heated line source
T_r	reference temperature
T_w	hot sensor temperature
t	time
U_c	mean centreline velocity
U_g	terminal velocity
U_i	velocity
u_i	velocity fluctuation
V	velocity sample space
V_{eff}	effective velocity
w	half-width
X, Y	random variables
x_i	components of the position vector in the test section
x, y	fluctuation of random variable X, Y

Greek symbols

γ molecular diffusivity

Δ wire spacing

δ_{ij} Kronecker delta

ϵ rate of dissipation of turbulent kinetic energy

ϵ_{th} dissipation factor of thermistor

ϵ_{θ} scalar dissipation rate

ε instantaneous dissipation rate of turbulent kinetic energy

η Kolmogorov microscale

η_{θ} local temperature microscale

Θ scalar sample space

θ temperature fluctuation

λ_{11} Taylor microscale

μ dynamic viscosity of the fluid

ν kinematic viscosity of the fluid

ν_T turbulent viscosity

ξ dimensionless transverse coordinate in non-homogeneous scalar fields

ρ density of the fluid

τ_{ij} shear stress tensor

τ dimensionless turbulence development time/total mean strain

χ sample space of random variable X

ψ sample space of random variable Y

Superscripts

$'$ root mean square

Acronyms

2D	two-dimensional
3D	three-dimensional
CDF	cumulative distribution function
DNS	direct numerical simulation
GT	grid-generated nearly isotropic turbulence
HSF	homogeneous sheared flow
JPDF	joint probability density function
LES	large eddy simulation
LDV	laser Doppler velocimetry
OHR	over heat ratio
rms	root mean square
PDF	probability density function
PLS	plume of a heated line source
RTD	resistance temperature detector
TML	thermal mixing layer
USF	uniformly sheared flow
UTG	uniform mean temperature gradient

Chapter 1

Introduction

1.1 Turbulent mixing and scalar transport

One of the goals of investigations of scalar fields is to provide an insight into the mixing process. Dimotakis (2005) reviewed various levels of scalar mixing. Passive scalar mixing is the first level which does not affect the flow dynamics. In other cases, the dynamics of the flow and mixing are coupled; mixing of the temperature and salinity fields in large-scale ocean currents is an example in this category. A third type of mixing makes changes to the fluid(s) and is necessarily coupled to the flow dynamics; examples are flows with combustion and detonations.

Turbulence is the essential mechanism that enhances the extent of mixing of scalar fields. This mixing enhancement has many practical applications in combustion and flow processes that require rapid mixing of scalar fields within short distances. The traditional approach for such problems is to investigate the transport equations of velocity and scalar fields in terms of statistical moments with modelling for reacting flow with large density variation and non-linear reaction rate. An alternative to the traditional approach in which the transport equations of velocity and scalar fields are expressed in terms of the physical variables is the probability density function (PDF) method, which was developed in the 1960s and 1970s (Pope, 1985). In the PDF method, the exact transport equations for the PDFs of the velocity and scalar fluctuations are derived from the Navier-Stokes and scalar transport equations. PDF equations for more than one scalar can also be derived, representing thermochemical states of the fluid based on the selected scalar parameters (*e.g.*, mass fractions and enthalpy). One of the main advantages of PDF equations is that, in reacting flows, the transport equation can be treated without approximation. This makes it unnecessary to consider additional assumptions, for example to introduce the linearity assumption for a very fast or very slow reaction rate. Maintaining the advantages of the velocity and scalar PDF equations, the transport equation of the joint probability density function (JPDF) of velocity and scalar takes exactly into account, in a closed form, the effects of convection, reaction, body force and mean pressure gradient, for complex flows such as those with a variable density and non-linear reaction rates. Compared to conventional turbulent closures, the PDF methods also have many advantages for inert and constant-density flows. All terms in the PDF transport equations can be determined from PDFs which are functions of velocity sample space, scalar sample space, time, and space. Density and source terms are known functions of scalar sample space and mean pressure is calculated through the Poisson equation in terms of the PDF. However, to solve the PDF transport equations, one needs to model some conditional expectations. The existing models for conditional expectations are developed so as to force the PDF or JPDF of fluctuations to relax into a normal distribution (Pope, 1985). Relaxation to a normal distribution is justified by the fact that the effects of diffusion eventually smoothen the PDF (Pope, 2000).

1.2 Objective of this thesis

In PDF methods, the assumption of Gaussian or jointly Gaussian distributions for scalar PDFs or JPDFs is consistent with some but not all experimental evidence of previous scalar experiments, which considered a single combination of velocity and scalar fields, which makes it difficult for a conclusive discussion on the shape of PDFs and JPDFs. The few available scalar experiments in turbulent flows contradict each other. The main objective of the present study is to measure the scalar PDF and other statistical properties of the scalar in three different passive scalar fields in uniformly sheared flow (USF). In this configuration, the turbulence is nearly homogeneous and free of external intermittency and wall effects. The three scalar fields include a homogeneous one, created by superimposing a uniform mean temperature gradient (UTG) in the transverse direction, and two non-homogeneous scalar fields, a thermal mixing layer (TML) and the plume of a heated line source (PLS). The non-homogeneous scalar fields have fundamentally different characteristics: the former one is free of initial effects but the latter one is not. The use of the same USF and the three scalar fields allows us to isolate the effects of non-homogeneity of scalar fields and initial conditions on the shapes of PDFs, which has not been addressed in previous scalar experiments. A second objective is to conduct measurements of conditional expectations which appear in terms of the scalar PDF equation. Such measurements include the conditional expectations of the velocity and the scalar dissipation rate upon the scalar fluctuation value.

1.3 Methodology

The measurement of JPDFs and conditional expectations requires simultaneous velocity-scalar measurements and measurements of scalar derivatives in three directions. The experimental study of the small-scale characteristics of a scalar field necessitates the use of a measurement technique that is capable of resolving motions with the smallest dynamically significant time and length scales of the field under investigation. Among the three most popular local velocity measurement techniques, which are particle image velocimetry (PIV), laser Doppler velocimetry (LDV) and hot-wire anemometry (HWA), we chose HWA, as this technique has the highest temporal and spatial resolutions, as well as not requiring flow seeding, which would have been inconvenient for our open-circuit wind tunnel facility. Concerning scalar measurements, a resistance thermometer, known as a “cold-wire”, is able to resolve temperature fluctuations up to a few kHz. The basic idea behind this method, which initially was proposed by Corrsin (1947), is that for low overheats the cold-wire is insensitive to velocity fluctuations and responds only to temperature fluctuations. Following consideration of alternative approaches, it was decided to use hot-wire anemometry and cold-wire thermometry for simultaneous measurement of velocity-temperature statistics and multi-sensor cold-wire thermometry for direct measurements of the scalar derivative statistics.

1.4 Plan of the thesis

This thesis is prepared in the form of a manuscript-based thesis. A general background which covers relevant PDF transport equations is provided in Chapter 2. Chapter 3 contains a description of the apparatus, instrumentation and measurement procedures used in the experiments. Experimental results and their analysis and discussion are presented in Chapter 4 in the form of two manuscripts to be submitted to a refereed journal for possible publication. Finally in Chapter 5, a summary of the main results of the thesis is presented, with contributions of this work and recommendations for future research.

Chapter 2

Background

2.1 Statistical definitions

The cumulative distribution function (CDF), or distribution function (Papoulis, 1991), of a random variable X is defined as the probability that $X \leq \chi$, i.e.,

$$F_X(\chi) = P(X \leq \chi), \tag{2.1}$$

where χ is the sample space of fluctuating parameters (herein χ-space). As χ varies from $-\infty$ to ∞, the CDF changes from 0 to 1 as a non-decreasing function. The joint distribution function of two random variables X and Y is defined by

$$F_{XY}(\chi, \psi) = P(X \leq \chi, Y \leq \psi), \tag{2.2}$$

where ψ is in a sample space of fluctuating parameters (herein ψ-space).

The probability density function (PDF) of a random variable X is defined as the derivative of its distribution function

$$f_X(\chi) = \frac{dF_X(\chi)}{d\chi}. \tag{2.3}$$

It is easy to infer the following properties of a PDF

$$f_X(\chi) \geq 0 \tag{2.4}$$

$$f_X(-\infty) = f_X(+\infty) = 0 \tag{2.5}$$

$$\int_{-\infty}^{+\infty} f_X(\chi)\, d\chi = 1 \tag{2.6}$$

$$F(\chi \le X \le \chi + d\chi) = f_X(\chi) d\chi. \tag{2.7}$$

This approach is extended to define the joint probability density function (JPDF) of X and Y (assuming that $F_{XY}(\chi,\psi)$ is a continuous function and has partial derivatives up to order two)

$$f_{XY}(\chi,\psi) = \frac{\partial^2 F_{XY}(\chi,\psi)}{\partial\chi\partial\psi}. \tag{2.8}$$

The CDF of a random variable X conditioned on an event Y_1 for which $P(Y_1) > 0$ is defined as

$$F_X(\chi \mid Y_1) = P(X \le \chi \mid Y_1) = \frac{P((X \le \chi)\, Y_1)}{P(Y_1)}, \tag{2.9}$$

where $P((X \le \chi)\, Y_1)$ is the joint probability of the random variable X and an event Y_1. The PDF of a random variable X conditioned on an event Y_1 for which $P(Y_1) > 0$ is defined as

$$f_X(\chi \mid Y_1) = \frac{d}{d\chi} F_X(\chi \mid Y_1). \tag{2.10}$$

2.1.1 Moments of a random variable

The expectation of the random variable X, denoted by $E(X)$ or $\langle X \rangle$, is defined as

$$\langle X \rangle = \int_{-\infty}^{+\infty} \chi f_X(\chi)\, d\chi. \tag{2.11}$$

The variance of X, or its central moment of second order, is defined as

$$\left\langle (X - \langle X \rangle)^2 \right\rangle \equiv \left\langle x^2 \right\rangle = \int_{-\infty}^{+\infty} (\chi - \langle X \rangle)^2 f_X(\chi)\, d\chi. \tag{2.12}$$

The square root of the variance is called the standard deviation and is a measure of the width of the PDF.

In general, a central moment of nth order is defined as

$$\langle (X - \langle X \rangle)^n \rangle \equiv \langle x^n \rangle = \int_{-\infty}^{+\infty} (\chi - \langle X \rangle)^n f_X(\chi)\, d\chi. \tag{2.13}$$

To provide a full statistical description of the random variable under investigation, one needs to specify either the PDF or the complete set of moments of the random variable.

2.2 Governing equations of turbulent flows

The velocity, temperature, pressure, and concentration in turbulent flows may be considered as random variables due to the random nature of such flows. The Reynolds decomposition consists of separating each flow parameter into an average and a fluctuation (Pope, 2000). It is interesting to note that the Reynolds decomposition was proposed before development of the modern axiomatic foundations of probability theory by Kolmogorov (1933).

2.2.1 Mass and momentum transport equations

In the proposed research, the air flow can be considered as Newtonian and incompressible, with a negligible body force. For such a flow, the conservation of mass and the momentum balance can be expressed as follows

$$\frac{\partial U_i}{\partial x_i} = 0 \tag{2.14}$$

and

$$\frac{\partial U_i}{\partial t} + U_j \frac{\partial U_i}{\partial x_j} = -\frac{1}{\rho}\frac{\partial P}{\partial x_i} + \nu \frac{\partial^2 U_i}{\partial x_j \partial x_j}, \tag{2.15}$$

where ρ and ν are the density and kinematic viscosity of the fluid and i =1, 2, and 3 represent streamwise, transverse, and spanwise directions, respectively. These equations and the following ones are written in Cartesian tensor notation, for which the

Einstein summation convention applies to terms with repeated Roman indices. By applying Reynolds decomposition to the velocity as $U = \langle U \rangle + u$ and to the pressure as $P = \langle P \rangle + p$, the Reynolds-averaged equations are obtained. Angle brackets in these expressions denote ensemble averages for the flow parameters. For stationary and ergodic flows, ensemble averages would be equal to corresponding time averages. In the following, we will assume that the flows of interest are stationary and ergodic and so will use time averages, which are denoted by overbars. Under such conditions, Reynolds decomposition may be written as $U = \overline{U} + u$ and $P = \overline{P} + p$. The fluctuation terms u and p are considered to be random variables with zero means. Taking the averages of all terms in the previous equations, one gets continuity and momentum equations for the means as, respectively,

$$\frac{\partial \overline{U}_i}{\partial x_i} = 0, \tag{2.16}$$

$$\frac{\partial \overline{U}_i}{\partial t} + \overline{U}_j \frac{\partial \overline{U}_i}{\partial x_j} = -\frac{1}{\rho}\frac{\partial \overline{P}}{\partial x_i} + \nu \frac{\partial^2 \overline{U}_i}{\partial x_j \partial x_j} - \frac{\partial \overline{u_i u_j}}{\partial x_j}. \tag{2.17}$$

The term $\langle u_i u_j \rangle$ is the covariance tensor of velocity fluctuations and the last term on the right hand side of equation 2.17 represents transport of momentum fluctuations by turbulent velocity fluctuations. It has been known since the time of Osborne Reynolds that turbulence produces virtual mean stresses which are proportional to the covariances of velocity fluctuations (Taylor, 1935). The Reynolds stress anisotropy tensor is defined as

$$m_{ij} = \frac{\overline{u_i u_j}}{2k} - \frac{1}{3}\delta_{ij}, \tag{2.18}$$

where δ_{ij} is the Kronecker delta and $k = \frac{1}{2}\overline{u_i u_i}$ is the turbulent kinetic energy per unit mass.

One can easily derive the momentum equation for the velocity fluctuations by substituting Reynolds decomposition in equation (2.15) and subtracting equation (2.17) from that as follows

$$\frac{\partial u_i}{\partial t} + \overline{U}_j \frac{\partial u_i}{\partial x_j} + u_j \frac{\partial \overline{U}_i}{\partial x_j} + u_j \frac{\partial u_i}{\partial x_j} = -\frac{1}{\rho}\frac{\partial \overline{P}}{\partial x_i} + \nu \frac{\partial^2 u_i}{\partial x_j \partial x_j} + \frac{\partial \overline{u_i u_j}}{\partial x_j}. \tag{2.19}$$

This equation demonstrates that there is coupling between the means and the fluctuations. Multiplying equation (2.19) by u_i and averaging, one obtains the balance equation for the turbulent kinetic energy as

$$\begin{aligned}\frac{\partial k}{\partial t} + \overline{U}_j \frac{\partial k}{\partial x_j} = &- \overline{u_i u_j}\frac{\partial \overline{U}_i}{\partial x_i} + \frac{1}{\rho}\frac{\partial \overline{u_j p}}{\partial x_j} - \frac{1}{2}\frac{\partial \overline{u_j u_i u_i}}{\partial x_j} \\ &+ \nu \frac{\partial^2 k}{\partial x_j \partial x_j} + \nu \frac{\partial^2 \overline{u_i u_j}}{\partial x_i \partial x_j} \\ &- \frac{1}{2}\nu \overline{\left(\frac{\partial u_i}{\partial x_j} + \frac{\partial u_j}{\partial x_i}\right)\left(\frac{\partial u_i}{\partial x_j} + \frac{\partial u_j}{\partial x_i}\right)}.\end{aligned} \tag{2.20}$$

The physical significance of each term in equation (2.20) can be summarized (Tavoularis, 2005) as follows.

- The left-hand side represents the total rate of change of k.
- $-\overline{u_i u_j}\frac{\partial \overline{U}_i}{\partial x_j}$ is the rate of production of k, which is in most cases positive.
- $-\frac{1}{\rho}\frac{\partial \overline{u_j p}}{\partial x_j}$ is the rate of work of pressure fluctuation gradients.
- $-\frac{1}{2}\frac{\partial \overline{u_j u_i u_i}}{\partial x_j}$ is the turbulent diffusion of k by non-linear turbulent interactions.
- $\nu \frac{\partial^2 \overline{u_i u_j}}{\partial x_i \partial x_j}$ and $\nu \frac{\partial^2 k}{\partial x_i \partial x_j}$ are terms representing viscous diffusion of Reynolds stresses.
- $\frac{1}{2}\nu \overline{\left(\frac{\partial u_i}{\partial x_j} + \frac{\partial u_j}{\partial x_i}\right)\left(\frac{\partial u_i}{\partial x_j} + \frac{\partial u_j}{\partial x_i}\right)}$ is the rate of dissipation ϵ of k, which is always positive.

2.2.2 Uniformly sheared flow

In the present study, the coordinate axes x_1, x_2, and x_3 are aligned with the streamwise, transverse, and spanwise directions, respectively. For uniformly sheared flow

(USF) in a wind tunnel, the mean velocity field is ideally defined as

$$\overline{U}_1 = \frac{d\overline{U}_1}{dx_2} x_2 + \overline{U}_c, \tag{2.21}$$

$$\overline{U}_2 = 0, \tag{2.22}$$

$$\overline{U}_3 = 0, \tag{2.23}$$

where the origin of x_2 is on the centreline of the wind tunnel and $\overline{U}_c$ is the mean velocity of the centreline velocity. Two dimensionless parameters that characterise a USF are defined as follows.

$$\tau = \frac{x_1}{\overline{U}_c} \frac{d\overline{U}_1}{dx_2}, \tag{2.24}$$

$$S^* = \frac{d\overline{U}_1}{dx_2} \frac{(2k)}{\epsilon}, \tag{2.25}$$

τ is the dimensionless development time, which also represents the total strain experienced by the turbulence. S^* is the shear rate parameter, which is the ratio of the turbulence timescale to the timescale of the mean shear and represents the relative strength of the turbulence with respect to the production by mean shear.

In USF, velocity and pressure fluctuations are ideally statistically homogeneous in any plane perpendicular to the streamwise direction, whereas the turbulence is stationary. In USF the turbulent kinetic energy equation (2.20) is simplified to

$$\overline{U}_1 \frac{dk}{dx_1} \approx -\overline{u_1 u_2} \frac{d\overline{U}_1}{dx_2} - \epsilon. \tag{2.26}$$

This equation can only be valid approximately because the left-hand side is a function of x_2 while the right-hand side is not. This means that the x_2 dependence of $\overline{U}_1$ tends to destroy the lateral homogeneity.

2.3 Equations for passive scalar transport

2.3.1 General equations

Assuming that, for small temperature differences, the effects of buoyancy are negligible, a passive scalar field is governed by the advection-diffusion equation

$$\frac{\partial T}{\partial t} + U_j \frac{\partial T}{\partial x_j} = \gamma \frac{\partial^2 T}{\partial x_j \partial x_j}, \tag{2.27}$$

where γ is the scalar diffusivity. Equation (2.27) is a linear equation in T. The physical significance of each term can be summarized as follows.

- The left-hand side represents the total rate of change of T, which is the sum of temporal and convective rates of change.

- The right-hand side represents the molecular diffusion of the scalar.

Applying the Reynolds decomposition to the temperature as $T = \overline{T} + \theta$, and substituting this into equation 2.27 and averaging all terms, one can derive the balance equation for the mean scalar as

$$\frac{\partial \overline{T}}{\partial t} + \overline{U}_j \frac{\partial \overline{T}}{\partial x_j} = \frac{\partial}{\partial x_j} \left(\gamma \frac{\partial \overline{T}}{\partial x_j} - \overline{\theta u_j} \right). \tag{2.28}$$

The last term on the right-hand side of this equation is called the turbulent heat flux vector. This term introduces three additional unknowns (namely $\langle \theta u_1 \rangle$, $\langle \theta u_2 \rangle$, and $\langle \theta u_3 \rangle$), which makes this equation open even if the statistical properties of the velocity field were known. One can derive a transport equation for the temperature fluctuations by subtracting (2.28) from (2.27) as

$$\frac{\partial \theta}{\partial t} + \overline{U}_j \frac{\partial \theta}{\partial x_j} + u_j \frac{\partial \overline{T}}{\partial x_j} + \frac{\partial \theta u_j}{\partial x_j} - \frac{\partial \overline{\theta u_j}}{\partial x_j} = \gamma \frac{\partial^2 \theta}{\partial x_j \partial x_j}. \tag{2.29}$$

Noting that the mean of the temperature fluctuations is equal to zero ($\overline{\theta} = 0$), the balance equation for the second moment of scalar fluctuations is

$$\frac{\overline{\theta^2}}{\partial t} + \overline{U}_j \frac{\partial\overline{\theta^2}}{\partial x_j} = -2\overline{\theta u_j}\frac{\partial\overline{T}}{\partial x_j} - \frac{\partial\overline{\theta^2 u_j}}{\partial x_j} + \gamma\frac{\partial^2\overline{\theta^2}}{\partial x_j \partial x_j} - 2\gamma\overline{\frac{\partial\theta}{\partial x_j}\frac{\partial\theta}{\partial x_j}}. \tag{2.30}$$

The different terms in this equation have the following physical significance.

- The left-hand side represents the total rate of change of scalar variance.
- $-2\overline{\theta u_j}\frac{\partial\overline{T}}{\partial x_j}$ is the rate of production of scalar fluctuations, which is usually positive, by the interaction of turbulent heat flux with the mean scalar gradient.
- $-\frac{\partial\overline{\theta^2 u_j}}{\partial x_j}$ is the rate of turbulent transport of scalar variance by velocity fluctuations.
- $\gamma\frac{\partial^2\overline{\theta^2}}{\partial x_j \partial x_j}$ is molecular diffusion of the scalar.
- $-2\gamma\overline{\frac{\partial\theta}{\partial x_j}\frac{\partial\theta}{\partial x_j}}\left[= -2\overline{\varepsilon_\theta} = -2\epsilon_\theta\right]$ is the rate of destruction of scalar fluctuations, ϵ_θ, of $\overline{\theta^2}$.

2.3.2 Scalar transport equations in uniformly sheared turbulence

Assuming a stationary USF and neglecting the streamwise gradient compared to the transverse gradient, equation (2.30) reduces to

$$\overline{U}_1\frac{\partial\overline{\theta^2}}{\partial x_1} = -2\overline{\theta u_2}\frac{\partial\overline{T}}{\partial x_2} - \frac{\partial\overline{\theta^2 u_2}}{\partial x_2} + \gamma\frac{\partial^2\overline{\theta^2}}{\partial x_2^2} - 2\epsilon_\theta. \tag{2.31}$$

For a passive scalar field imposed on a stationary USF flow, in addition to the rate of production and destruction of scalar fluctuations, the rate of turbulent transport by velocity fluctuations and molecular diffusion affect the rate of change of scalar variance. For a scalar field with a uniform mean temperature gradient in USF, where the scalar and velocity fields are both transversely nearly homogeneous, equation 2.31 reduces to the following equation (Tavoularis & Corrsin, 1981*a*; Ferchichi & Tavoularis, 2002).

$$\overline{U}_1\frac{\partial\overline{\theta^2}}{\partial x_1} \approx -2\overline{\theta u_2}\frac{\partial\overline{T}}{\partial x_2} - 2\epsilon_\theta. \tag{2.32}$$

One of the advantages of the above equation is its similarity to the equation of turbulent kinetic energy in USF, equation (2.26), which introduces an analogy between the structures of the scalar field and of the velocity field.

Multiplying equation (2.15) by θ and equation (2.27) by u_i, adding and taking the mean and using the continuity equation, one can get the equation of turbulent heat flux (or temperature-velocity covariance) as

$$\begin{aligned}\frac{\partial\overline{\theta u_i}}{\partial t} + \overline{U}_j\frac{\partial\overline{\theta u_i}}{\partial x_j} = &- \frac{\partial\overline{\theta u_i u_j}}{\partial x_j} - \overline{u_i u_j}\frac{\partial\overline{T}}{\partial x_j} \\ &- \overline{\theta u_j}\frac{\partial\overline{U}_i}{\partial x_j} - \frac{1}{\rho}\ \overline{\theta\frac{\partial p}{\partial x_i}} \\ &+ \frac{\partial}{\partial x_j}\left(\gamma\ \overline{u_i\frac{\partial\theta}{\partial x_j}} + \nu\ \overline{\theta\frac{\partial u_i}{\partial x_j}}\right) \\ &- \left(\nu\gamma\ \overline{\frac{\partial u_i}{\partial x_j}\frac{\partial\theta}{\partial x_j}}\right).\end{aligned} \tag{2.33}$$

In the case of a statistically stationary USF with a 2D mean scalar field, the non-zero components of the previous equation may be reduced to the forms

$$\begin{aligned}\overline{U}_1\frac{\partial\overline{\theta u_1}}{\partial x_1} = &- \frac{\partial\overline{\theta u_1 u_2}}{\partial x_2} - \overline{u_1 u_2}\frac{\partial\overline{T}}{\partial x_2} - \overline{\theta u_2}\frac{\partial\overline{U}_1}{\partial x_2} - \frac{1}{\rho}\ \overline{\theta\frac{\partial p}{\partial x_1}} \\ &+ \frac{\partial}{\partial x_2}\left(\gamma\ \overline{u_1\frac{\partial\theta}{\partial x_2}} + \nu\ \overline{\theta\frac{\partial u_1}{\partial x_2}}\right) - \left(\nu\gamma\ \overline{\frac{\partial u_1}{\partial x_j}\frac{\partial\theta}{\partial x_j}}\right)\end{aligned} \tag{2.34}$$

and

$$\begin{aligned}\overline{U}_1\frac{\partial\overline{\theta u_2}}{\partial x_1} = &- \frac{\partial\overline{\theta u_2^2}}{\partial x_2} - \overline{u_2^2}\frac{\partial\overline{T}}{\partial x_2} - \frac{1}{\rho}\ \overline{\theta\frac{\partial p}{\partial x_2}} \\ &+ \frac{\partial}{\partial x_2}\left(\gamma\ \overline{u_2\frac{\partial\theta}{\partial x_2}} + \nu\ \overline{\theta\frac{\partial u_2}{\partial x_2}}\right) - \left(\nu\gamma\ \overline{\frac{\partial u_2}{\partial x_j}\frac{\partial\theta}{\partial x_j}}\right).\end{aligned} \tag{2.35}$$

2.3.3 Growth of a thermal mixing layer in USF

One can consider a USF which is stationary and two dimensional on the mean. By imposing a thermal mixing layer in which the streamwise gradient of any scalar statistical property is negligible compared to its transverse gradient and neglecting molecular diffusion compared to turbulent diffusion, the mean scalar transport equation (2.28) is reduced to

$$\overline{U}_1 \frac{\partial \overline{T}}{\partial x_1} \approx -\frac{\partial \overline{u_2 \theta}}{\partial x_2}. \tag{2.36}$$

Applying a gradient transport model to approximate the turbulent heat flux term (Sreenivasan *et al.*, 1982) and also considering that the transverse mean scalar gradient is the dominant component of $\frac{\partial \overline{T}}{\partial x_i}$, equation (2.36) may be simplified to

$$\overline{U}_1 \frac{\partial \overline{T}}{\partial x_1} \approx -D_{22} \frac{\partial \overline{T}}{\partial x_2}, \tag{2.37}$$

where D_{22} is the turbulent diffusivity, which is a function of the local scales of the turbulent velocity field. According to the gradient transport model, maximum production would occur at the location of the maximum temperature gradient. The mean shear can affect the solution in two different ways, first through the mean velocity and second through the turbulent diffusivity. If the solution is limited to a relatively narrow mixing layer, in which one may assume that the mean velocity is uniform, one may derive a self-similar solution for the mean temperature rise in the form (Ferchichi & Tavoularis, 1992)

$$\frac{\Delta \overline{T}\left(x_1, x_2\right)}{\Delta \overline{T}_h} = \frac{1}{2}\left[1 + erf\left(\xi\right)\right], \tag{2.38}$$

where $\Delta \overline{T}_h$ is the temperature difference between the warm and cool streams and ξ is a dimensionless transverse coordinate, defined as $\xi = [x_2 + x_{20}(x_1)]/w(x_1)$; in this expression, x_{20} is the displacement of the thermal mixing layer centre and the mixing layer width $w(x_1)$ is the distance between points at which the mean temperature rise is equal to 0.25 and $0.75\Delta \overline{T}_h$. Extensions of this analysis provide estimates for the temperature variance and the temperature-velocity covariance vector (Ferchichi

& Tavoularis, 1992).

2.3.4 Transport equation for the velocity-scalar PDF

The formulation of statistical balance equations for the turbulent velocity and for transported scalars (*i.e.*, the concentration of an admixture or temperature) in terms of their PDF and JPDF is an alternative to the more common approach, which is in terms of statistical moments. The transport equation of a velocity-scalar JPDF without a source term, neglecting gravity forces, and assuming constant density, has the following form

$$\rho\left[\left(\frac{\partial f_{u\theta}}{\partial t}+\overline{U}_j\frac{\partial f_{u\theta}}{\partial x_j}\right)-\left(\frac{\partial\overline{P}}{\partial x_j}\frac{\partial f_{u\theta}}{\partial U_j}\right)\right]=\frac{\partial\left[\left(-\overline{\frac{\partial\tau_{ij}}{\partial x_j}|V,\Theta}+\overline{\frac{\partial p}{\partial x_j}|V,\Theta}\right)f_{u\theta}\right]}{\partial U_j} - \frac{\partial^2\left[\left(\overline{\varepsilon_\theta|V,\Theta}\right)f_{u\theta}\right]}{\partial\Theta^2}, \tag{2.39}$$

where V is the velocity sample space (V-space), $\tau_{ij}=\mu\left(\frac{\partial u_i}{\partial x_j}+\frac{\partial u_j}{\partial x_i}-\frac{2}{3}\frac{\partial u_k}{\partial x_k}\delta_{ij}\right)$ and μ is the dynamic viscosity of the fluid (Williams, 1965; Swaminathan & Bray, 2011).

- The first term on the left-hand side is transport in physical space.
- The second term on the left-hand side is transport in velocity space by the mean pressure gradient.
- The first term on the right-hand side represents transport in velocity space by the viscous stresses and by the fluctuating pressure gradient.
- The second term on the right-hand side represents transport in Θ-space (scalar space) by the molecular fluxes.

The PDF approach has an advantage in reactive flows, because it can treat arbitrary chemical reactions exactly, whereas the moment approach requires the use of models. As can be seen in Eqn. 2.39, terms that represent convection, reaction and body force are in closed form and the mean pressure force can also be converted to a closed form using Poisson equation; nevertheless, terms that represent molecular processes and fluctuating pressure forces contain conditional expectations, which have to be modelled. Models of these terms have usually been tested in homogeneous turbulence with superimposed canonical scalar fields, in which velocity and scalar fluctuations may, under certain conditions, have a normal JPDF, in conformity with some experimental evidence.

2.3.5 Transport equation for the scalar PDF

An alternative approach to the solution of the velocity-scalar JPDF equation is the solution of the turbulent velocity equations by some approximate means, such as large eddy simulation (LES), together with solving the scalar PDF equation (Pope, 1985). Despite some known disadvantages of the scalar PDF equation by comparison to the JPDF equation (Pope, 1985), the former provides a suitable theoretical foundation for examining the statistical properties of a scalar field in turbulent flows. In particular, it allows one to focus on the statistical differences between different scalar fields embedded in the same turbulence, which is the topic of concern in the present study. Ferchichi (1998) derived the following transport equation for the PDF of temperature fluctuations directly from Eqn. 2.29 by taking the time derivative of the averaged "fine–grained" PDF (Lundgren, 1967).

$$\begin{aligned}\frac{\partial f_\theta}{\partial t} + \overline{U}_j \frac{\partial f_\theta}{\partial x_j} - \frac{\partial \overline{T}}{\partial x_j} \frac{\partial \left(\overline{u_j \mid \theta = \Theta} \; f_\theta \right)}{\partial \Theta} + \frac{\partial \left(\overline{u_j \mid \theta = \Theta} f_\theta \right)}{\partial x_j} + \frac{\partial \overline{\theta u_j}}{\partial x_j} \frac{\partial f_\theta}{\partial \Theta} \\ = \gamma \frac{\partial^2 f_\theta}{\partial x_j \partial x_j} - \frac{\partial^2 \left(\overline{\epsilon_\theta \mid \theta = \Theta} f_\theta \right)}{\partial \Theta^2},\end{aligned} \tag{2.40}$$

where Θ is the sample space of the temperature field (Θ-space). The physical significances of the different terms in Eqn. 2.40 and the corresponding terms in Eqn. 2.29 are as follows.

- $\frac{\partial f_\theta}{\partial t} + \overline{U}_j \frac{\partial f_\theta}{\partial x_j}$: this term is the total rate of change of temperature PDF and corresponds to $\frac{\partial \theta}{\partial t} + \overline{U}_j \frac{\partial \theta}{\partial x_j}$.
- $\frac{\partial \overline{T}}{\partial x_j} \frac{\partial \left(\overline{u_j | \theta = \Theta} f_\theta \right)}{\partial \Theta}$: this term is the turbulent transport of the temperature PDF by the mean temperature gradient in Θ-space and corresponds to $u_j \frac{\partial \overline{T}}{\partial x_j}$.
- $\frac{\partial \left(\overline{u_j | \theta = \Theta} \ f_\theta \right)}{\partial x_j}$: this term is the turbulent transport of temperature PDF in physical space and corresponds to $\frac{\partial \theta u_j}{\partial x_j}$.
- $\frac{\partial \overline{\theta u_j}}{\partial x_j} \frac{\partial f_\theta}{\partial \Theta}$: this term is the transport of the temperature PDF by the gradient of turbulent heat flux in the Θ–space and corresponds to $\frac{\partial \overline{\theta u_j}}{\partial x_j}$.
- $\gamma \frac{\partial^2 f_\theta}{\partial u_j \partial u_j}$, $\frac{\partial^2 \left(\overline{\varepsilon_\theta | \theta = \Theta} \ f_\theta \right)}{\partial \Theta^2}$: these terms are the molecular diffusion of the temperature PDF in the physical space and the molecular diffusion of the temperature PDF in Θ-space; they correspond to $\gamma \frac{\partial^2 \theta}{\partial x_j \partial x_j}$.

Like the JPDF equation, the scalar PDF equation contains conditional expectations, which need to be modelled. However, instead of a conditional fluctuating pressure gradient term, the scalar PDF includes a turbulent transport term, which contains the conditional velocity expectation $\overline{u_i | \theta = \Theta}$ (Pope, 2000). A common modelling assumption is to assume that $\overline{u_i | \theta = \Theta}$ is a linear function of Θ, which would be true if the velocity-scalar JPDF were jointly normal. Models that account for the effects of the molecular diffusion term, which contains the conditional expectation of scalar dissipation rate upon the scalar fluctuations $\overline{\varepsilon_\theta | \theta = \Theta}$, are required to close Eqn. 2.40 too. These models, referred to as mixing models, usually have a limited scope, which is to produce a JPDF with realistic first and second order moment evolutions (Pope, 1985).

Ferchichi & Tavoularis (2002) showed that, for a USF with a uniform mean temperature gradient in which the velocity and the temperature fields are transversely nearly homogeneous, equation 2.40 could be simplified to the following form

$$\overline{U}_j \frac{\partial f_\theta}{\partial x_j} = \frac{\partial \overline{T}}{\partial x_j} \frac{\partial \left(\overline{u_j \mid \theta = \Theta} \ f_\theta \right)}{\partial \Theta} - \frac{\partial^2 \left(\overline{\varepsilon_\theta \mid \theta = \Theta} \ f_\theta \right)}{\partial \Theta^2}. \tag{2.41}$$

Additionally, if one assumes that (a) the conditional expectations of the velocity fluctuations are linearly related to the value of the scalar; (b) the scalar dissipation rate and the scalar value are statistically independent; and (c) the scalar PDF in a stationary turbulent flow is self-preserved, the only acceptable solution of equation 2.41 is the Gaussian function. Ferchichi & Tavoularis (2002) demonstrated that these assumptions were approximately satisfied in a USF with a uniform mean temperature gradient.

2.4 Lengthscales

One of the features of all turbulent flows is the wide range of lengthscales they contain. One way to characterize spatial structures is to investigate the spatial correlation tensor. The typical separation distance over which a component of the spatial correlation tensor approaches zero is a measure of the macroscopic lengthscale of the turbulent flow in a particular direction. These lengthscales, known as integral lengthscales, are comparable to geometrical scales of the apparatus. Using one point measurement and Taylor's frozen flow approximation, one can define the streamwise integral lengthscale for the case of a statistically stationary process as

$$L_{11,1} \approx \overline{U}_1 \int_0^\infty \frac{\overline{u_1(t)u_1(t+\tau)}}{\overline{u_1^2(t)}} d\tau. \tag{2.42}$$

where $\tau = t_2 - t_1$ is the time lag. The same approach can be applied to the scalar field to define the streamwise scalar integral lengthscale as

$$L_{\theta,1} \approx \overline{U}_1 \int_0^\infty \frac{\overline{\theta_1(t)\theta_1(t+\tau)}}{\overline{\theta_1^2(t)}} d\tau. \tag{2.43}$$

The smallest eddy sizes in a turbulent flow are characterized by the Kolmogorov microscale $\eta = (\nu^3/\epsilon)^{1/4}$. By analogy to the velocity field, the local temperature microscale is defined as $\eta_\theta = (\gamma^3/\epsilon)^{1/4}$. It characterizes the smallest significant scale of the scalar field, at which the scalar differences are smeared out by molecular effects.

The Taylor microscale is an intermediate lengthscale. The streamwise Taylor microscale is defined as

$$\lambda_{11} = \sqrt{\frac{\overline{u_1^2}}{\overline{(\partial u_1/\partial x_1)^2}}}. \tag{2.44}$$

By analogy to the velocity field, the Corrsin microscale is defined as

$$\lambda_{\theta 1} = \sqrt{\frac{\overline{\theta^2}}{\overline{(\partial \theta/\partial x_1)^2}}}. \tag{2.45}$$

Using Taylor's approximation, the Taylor and Corrsin microscales can be estimated from temporal derivatives, which can be conveniently measured with a single probe. The corresponding expressions are

$$\lambda_{11} = \overline{U}_1 \sqrt{\frac{\overline{u_1^2}}{\overline{(\partial u_1/\partial t)^2}}}, \tag{2.46}$$

$$\lambda_{\theta 1} = \overline{U}_1 \sqrt{\frac{\overline{\theta^2}}{\overline{(\partial \theta/\partial t)^2}}}. \tag{2.47}$$

A turbulence Reynolds number that describes the strength of turbulence activity is defined as

$$Re_\lambda = \frac{\sqrt{\overline{u_1^2}}\ \lambda_{11}}{\nu}. \tag{2.48}$$

Chapter 3

Literature review

3.1 Uniformly sheared turbulence

Experimental studies of the structure of turbulent flows can be mostly categorized in two different groups: those of inhomogeneous and those of homogeneous turbulent flows. Wakes, jets, boundary layers, channel flows and atmospheric turbulence are some well-known examples of inhomogeneous turbulence, which is also anisotropic. On the other hand, grid turbulence is considered as nearly homogeneous and isotropic. A case of nearly homogeneous but anisotropic flow is uniformly sheared turbulence.

The first attempt to generate a USF was conducted by Rose (1966) using a grid consisting of parallel rods with variable spacing to produce a velocity gradient. This flow suffered from non-uniform length scales. Afterward, Champagne *et al.* (1970) used equally spaced parallel channels with transversely varying porosity, followed by flow-separating plates. They were able to produce USF with nearly uniform scales. Additional experimental studies of USF are the following.

- Harris *et al.* (1977) studied USF with greater shear rate and a longer development time than Champagne et al., in the same wind tunnel.

- Tavoularis & Corrsin (1981*a*) used hot-wire anemometry to study the properties of USF with a superimposed uniform mean temperature gradient in a wind tunnel. They modified the shear generator of the Harris *et al.* (1977) to achieve higher turbulent intensities. They measured temperature fluctuation utilizing resistance thermometers (cold-wires).

- Rohr *et al.* (1988) studied USF generated by deviding the cross section in 9 channels and injecting fluid at a different flow rate in each channel. For velocity measurement, they used hot-films.

- Tavoularis & Karnik (1989) used hot-wire anemometry to document the effect of the shear value on USF in a wind tunnel at moderate Re_λ. The shear generator was based on the Tavoularis & Corrsin (1981*a*) design.

- De Souza *et al.* (1995) used LDV to study USF in a high speed wind tunnel. They used a perforated plate with variable porosity followed by a flow separator to produce turbulent Re number of the order of 10^3.

- Garg & Warhaft (1998), using hot-wire anemometry, investigated the small scale characteristics of the USF in the range of $156 \leq Re_\lambda \leq 390$. They used the Tavoularis & Corrsin (1981*a*) design for their shear generator in their wind tunnel.

- Ferchichi & Tavoularis (2000) used hot-wire anemometry to study the effect of the turbulent Reynolds number on the fine structure of USF in the same facility as Karnik & Tavoularis (1987) with a turbulent Reynolds number up to 660.

- Shen & Warhaft (2000, 2002) and Warhaft & Shen (2002) used an active grid followed by a screen shear generator to study the effects of high turbulent Reynolds number up to 1000 on the small scales. In particular, they studied the higher order structure functions and mixed structure functions using hot-wire anemometry.

- Kislich-Lemyre (2002) used LDV and flow visualisation to study the large-scale structure of USF produced by a perforated plate in a water tunnel.

- Gylfason *et al.* (2004) studied intermittency, pressure and acceleration statistics from hot-wire measurements in wind-tunnel turbulence in USF for the range $452 \leq Re_\lambda \leq 877$. They used the same set-up as Shen & Warhaft (2000) to produce USF.

- Isaza *et al.* (2009) investigated the large-scale velocity statistics of USF. They used both an active and a passive grid to produce USF with different initial value of the shear parameter. They also used hot-wire anemometry for their velocity measurements.

- Vanderwel & Tavoularis (2011), expanded on the work of Kislich-Lemyre using PIV and flow visualization to quantitatively study the large-scale structure of USF in a water tunnel with a turbulent Reynolds number around 150.

Alternative methods of generating the uniform shear including curved screens, or tapered honeycombs are described by Dunn & Tavoularis (2007).

The main time-averaged characteristics of the USF can be highlighted as follows:

- The Reynolds stresses and turbulent kinetic energy grow exponentially in USF (Tavoularis, 1985).

- It is observed that the exponential growth only begins after a sufficient development time has been achieved ($\tau \gtrsim 5$, Tavoularis & Karnik (1989)).

- The magnitudes of the non-zero Reynolds stresses are ordered as $\langle u_1^2 \rangle > \langle u_3^2 \rangle > \langle u_2^2 \rangle > -\langle u_1 u_2 \rangle$. The reason is that the streamwise normal stress receives energy directly from the mean shear but the others receive energy indirectly from the streamwise component through pressure-strain rate covariance terms.

- The previous studies also measured the integral length scale L_{11} and Taylor's microscale λ_{11}. The integral length scale is observed to consistently grow from a starting value, which is comparable to the spacing of the elements in the shear generating apparatus.

Moreover, several direct numerical simulation (DNS) studies investigated the HSF within relatively small ranges of turbulent Reynolds number and short development times. These include the studies by Rogers & Moin (1987), Adrian & Moin (1988), Lee *et al.* (1990), Kida & Tanaka (1994), and Isaza & Collins (2009). The DNS results established a close correspondence between the turbulence structure and the evolution rate in HSF and those in USF. DNS have also determined the temporal evolutions of the entire velocity and vorticity fields. These studies identified coherent structures in HSF, which were confirmed by the experimental observations of Kislich-Lemyre (2002) and Vanderwel & Tavoularis (2011) in USF. Among DNS studies, the results of Rogers & Moin (1987) and Adrian & Moin (1988) clearly identified the presence of hairpin vortices in HSF. Lee *et al.* (1990) and Kida & Tanaka (1994) investigated the instantaneous structure of HSF and showed that it is organized into coherent turbulent structures. Isaza & Collins (2009) discussed the asymptotic behaviour of large-scale turbulence in HSF. A limitation of DNS is that they are restricted to relatively low Reynolds numbers.

3.2 Passive scalar fields

Generating a temperature fluctuation field, as a passive scalar, is one of the prevalent experimental approaches to investigate the small scale structure of scalar fields in turbulent flows. Warhaft (2000) published an extensive review on passive scalars in turbulence. This review focuses on the cascade phenomenology, the deviation from local isotropy assumption in the inertial and dissipation ranges and its the dependence of local anisotropy on internal intermittency. One of the addressed issues in that review was about non-Gaussianity of the PDF of the scalar fluctuations in some experimental results. Dimotakis (2005) also provides an overview of turbulent mixing at different levels and the existing experimental, theoretical, and computational challenges.

3.2.1 Passive scalar fields in different turbulent flows

The earlier study of Tavoularis & Corrsin (1981*a*) in USF with a mean temperature gradient showed that, in addition to Gaussianity of the scalar and velocity statistics, the velocity-scalar joint PDF is also jointly Gaussian. They used round heating rods right after the flow separator to produce temperature field at a turbulent Reynolds number up to 266. This flow has been re-examined by Ferchichi & Tavoularis (2002) with the same range of Reynolds number but the focus was on the PDF of the scalar and velocity fields. Their heating system was made of Nicrome ribbons mounted on a wooden frame and placed at a distance downstream of the shear generator. They showed that the conditional expectations of the velocity fluctuations were linearly related to the scalar value and the scalar dissipation rate was statistically independent of the scalar. They also supported their results with a theoretical analysis using PDF formulation (Pope, 1985). Their results were consistent with the results of Tavoularis & Corrsin (1981*a*).

In the 1980s and early 1990s, there were several experimental studies of thermal mixing layers in grid turbulence. LaRue *et al.* (1981) and LaRue & Libby (1981) produced a thermal mixing layer by heating half of their grid. Ma & Warhaft (1986) investigated a similar flow with a mandolin and a toaster to produce the mixing layer. Both experiments suggested zero value of the skewness of the temperature fluctuations at the centre of the thermal mixing layer and peaks near the edges. The kurtosis showed small sub-Gaussianity (~ 2.8). In this flow, the thermal mixing layer is a transversely non-homogeneous scalar field and the grid turbulence provides nearly isotropic velocity field, which is also nearly homogeneous on a transverse plane.

Ferchichi & Tavoularis (1992) studied the evolution of a thermal mixing layer in USF. The results showed that the mean temperature field reached a quasi-asymptotic state and the thermal mixing layer approximately maintained an error-function-like profile (like grid turbulence experiments) with a width that grew almost linearly. Their theoretical predictions of the thermal mixing layer width and temperature fluctuation statistics agreed with their measurements. However, they did not report any PDF.

Karnik & Tavoularis (1989) investigated diffusion from a heated line source in a USF with a turbulent Reynolds number up to 360. As expected, the reported joint PDF of velocities were nearly Gaussian. On the other hand, the PDF of the temperature fluctuations showed a measurable deviation from the Gaussian behaviour, with a skewness that increased with increasing distance from the centreline. However, the velocity-temperature correlation coefficient $\langle \theta u_i \rangle / \left(\langle \theta^2 \rangle \langle u_i^2 \rangle \right)^{1/2}$ on the centreline is around zero due to the approximate symmetry of the mean temperature field. Whether the non-Gaussianity of temperature fluctuations at the centreline was related to zero correlation of the temperature and velocity fluctuations was not investigated in these experiment. The joint PDF of velocity-scalar also indicated an increasing deviation from a Gaussian behaviour away from the centreline. In this configuration, the scalar field is transversely inhomogeneous whereas the velocity field is transversely nearly homogeneous.

Sinai & Yakhot (1989) derived theoretically an exact closed-form solution for the scalar PDF of a homogeneous decaying scalar field with no mean gradient and a statistically stationary turbulent field. They showed that this solution would reduce to a Gaussian PDF if the conditional scalar dissipation were independent of the scalar value. Based on Sinai & Yakhot's solution, Ching (1993) presented a closed solution for the PDF of temperature fluctuations using a fluctuation-dissipation assumption. Ching explained that the use of this assumption might be justified by considering the universal characteristics of turbulence fluctuations. However, the validity of this assumption for a forced thermal field remained unclear. Ching derived various types of PDF shapes depending on the conditional expectation of dissipation rate. For example, a power-law behaviour of conditional expectation of dissipation rate would result in a stretched-exponential PDF and a constant conditional expectation of dissipation rate would give a Gaussian PDF.

Pope & Ching (1993) obtained an exact expression for the PDF of any measured quantity in a general stationary process in terms of conditional expectations of time derivatives of the property under investigation. Their expression indicated that the conditional expectations of both the time derivative squared and of the second time derivative influenced the shape of the PDF, including its tails. They also showed that Ching's fluctuation-dissipation assumption corresponds to the case when the expectation of the second time derivative of the scalar conditioned upon scalar value is a linear function of the scalar value. Using the Chicago convection data (Castaing *et al.*, 1989), they plotted the conditional expectation of the second time derivative of the scalar against the scalar value which indeed showed linearity. One should note, however, that the calculation of the second time derivative from experimental results is subjected to higher experimental uncertainty. In this regard, it is also notable that the two conditional expectations that appear in equation (2.40), i.e., the conditional expectations of velocity and dissipation rate upon the scalar value, originate from the transport equation of the scalar field, whereas the conditional expectation of the second time derivative mentioned by Pope & Ching (1993) has no connection to the transport equation of the scalar field and it is valid for any stationary random process.

The previous analytical studies motivated several experimental studies. Jayesh & Warhaft (1992) examined the scalar PDF and the conditional dissipation in a grid-generated turbulence with a uniform mean temperature gradient. Their measurements were conducted over the range $60 \leq Re_l \leq 1100$, where the Reynolds number Re_l was based on the integral length scale and the standard deviation of velocity fluctuations. For $Re_l > 70$, all PDF showed exponential tails. These authors found significant positive values of the correlation between the mean scalar fluctuations and the scalar dissipation rate when exponential tails occurred. This means that the conditional scalar dissipation rate was not independent of the scalar value. Jayesh & Warhaft (1992) argued that dependency of the statistics of the scalar dissipation rate and the scalar fluctuations was the result of some large and rare fluctuations, which produced exponential tails of the scalars.

Gylfason & Warhaft (2004) addressed the truncation effects in the temperature statistics (PDF) caused by limited dimensions of their experimental apparatus with respect to the integral length scales of the flow. They used three different grids to produce flows with different integral length scales. By investigating the PDF of temperature, they inferred that rare fluctuations were able to arrive at the measuring point from far transverse positions towards upstream when the integral length scale was sufficiently small compared to the width of the tunnel. For the largest ratio of the integral length scale to the wind tunnel width, they observed sub-Gaussian PDF of the temperature fluctuations.

Anselmet *et al.* (1994) studied the joint statistics of a passive scalar and their dissipation rate in a boundary layer and a jet. They showed that, in regions where the temperature skewness factor was nearly zero, the correlation coefficient was also very small, and the assumption of independence was fully justified. They concluded that the main parameter influencing the joint statistics of temperature and its dissipation rate was the asymmetry of temperature fluctuations, which was different in each of their flows. Mi *et al.* (1995) investigated the joint statistics between temperature and its dissipation rate components in the self-preserving region of a slightly heated round jet. The results pointed out that the assumption of statistical independence between the dissipation rate and the fluctuations appears to be more closely approximated in their turbulent round jet than in a turbulent plane jet. Mi (2006) presented some experimental results for the correlation between non-Gaussian statistics of a scalar and its dissipation rate in wake and jet flows and concluded that the independence assumption, often used in combustion modelling, is appropriate only in flow regions in which the scalar PDF is close to a Gaussian one. The previous studies did not report any results on the conditional expectation of velocity components upon the scalar value.

As it is inferred from equation (2.40), the conditional expectation of the velocity upon the scalar also plays a role in the transport of the scalar. Li & Bilger (1994) presented experimental results on the conditional mean transverse velocity across a turbulent scalar mixing layer. Their results showed that the conditional mean transverse velocity is approximately a linear function of the scalar fluctuations at the centre of the scalar mixing layer and is strongly non-linear at the edge of the mixing layer. Feng *et al.* (2007) investigated the velocity conditioned on a conserved scalar in a confined liquid rectangular jet using simultaneous PIV and PLIF. The joint velocity-scalar PDF was not Gaussian in their flow and the PDF of the conserved scalar was accurately described by a beta-type PDF. They stated that the conditional mean velocity was a linear function of the scalar value when it was close to its local mean value. Their report is consistent with the Jayesh & Warhaft (1992) observation of large and rare fluctuations, which are responsible for the exponential tails of the scalar

PDF.

Lavertu & Mydlarski (2005), Lepore & Mydlarski (2011) and Germaine *et al.* (2014) performed a series of scalar experiments by inserting a heated line source across a fully developed flow in a channel with an aspect ratio of approximately 18. In these experiments, both the velocity and the scalar fields were inhomogeneous. Lavertu & Mydlarski (2005) investigated a two-dimensional PLS by placing the line source across the width (*i.e.*, the long dimension) of the channel, whereas Lepore & Mydlarski (2011) generated a three-dimensional scalar field by placing the source across the height of the channel. The results of both studies showed that, far downstream of the line source, the scalar PDF was nearly Gaussian, both in the channel centre and close to the wall. Germaine *et al.* (2014) measured the conditional expectations of the scalar dissipation in the two-dimensional PLS in the channel flow and found that all three components of the scalar dissipation rate depended strongly on the temperature fluctuation value.

3.2.2 Numerical models

The recent review of Haworth (2010) discussed progress in PDF methods and particular physical models for modelling conditional expectations. In equation (2.39), the conditional expectations correspond to viscous stresses, the fluctuating pressure gradient, and scalar molecular fluxes. In this case, assuming a passive scalar, the conditional expectations of the viscous stresses and fluctuating pressure gradient upon the velocity and scalar would be independent of the scalars and can be modelled by generalized Langevin models (Pope, 2000). In the scalar PDF equation, the conditional expectation terms are those corresponding to turbulent velocity fluctuations and scalar molecular fluxes (Haworth, 2010). The effects of molecular diffusion appear in terms of scalar molecular fluxes or equivalently the conditional expectation of scalar dissipation rate, equations (2.40) and (2.39). This conditional expectation exists at both PDF equations for velocity-scalar and scalar. The models for the effects of molecular diffusion (or equivalently models for conditional expectation of scalar dissipation rate) are called mixing models. Some common mixing models include the interaction by exchange with the mean model (IEM) by Villermaux & Devillon (1972) and the linear mean-square estimation model (LMSE) by Dopazo & O'Brien (1974). These two models are independent of velocity value, however, several other models which depend on velocity value have been proposed (Fox, 1996). A common assumption of these mixing models is that the PDF of conserved scalars should relax to normal distributions in statistically homogeneous systems. This assumption has been supported by some experimental results (Tavoularis & Corrsin, 1981*a*; Ferchichi & Tavoularis, 2002). The models contain certain adjustable coefficients which have been evaluated from experimental and/or DNS data (Haworth, 2010). As an example, a new mixing model, called the shadow-position mixing model (SPMM), is introduced by Pope (2013). The performance of this model is tested against a scalar mixing layer in which it is assumed that in the center of the layer the Gaussian estimate can be expected to be accurate.

3.2.3 Anisotropy and intermittency of scalar fields

The departure from local isotropy at moderate Reynolds numbers is very evident in second order moments of scalars (Warhaft, 2000). The variation in the slope of the passive scalar spectra in different flows confirms this departure (Warhaft, 2000). It is notable that for scalar field in shear flows, there is a slower evolution of the spectral slope toward $-5/3$ (Sreenivasan, 1991) compared to similar scalar fields in grid turbulence experiments (Mydlarski & Warhaft, 1998). Budwig *et al.* (1985) and Tong & Warhaft (1994) for grid turbulence and Sreenivasan & Antonia (1977) for shear flow found that $\left\langle (\partial\theta/\partial x_2)^2 \right\rangle \approx 1.4 \left\langle (\partial\theta/\partial x_1)^2 \right\rangle$. This was contrary to the isotropy assumption for small scales, which postulates that $\left\langle (\partial\theta/\partial x_2)^2 \right\rangle = \left\langle (\partial\theta/\partial x_1)^2 \right\rangle$. In grid turbulence, this small scale anisotropy at the second order is independent of Re_λ (Mydlarski & Warhaft, 1998).

At the third order moments, the local isotropy assumption for the scalar field is broken down entirely. This breakdown depicts a direct effect of the large scale structures on motions with inertial and dissipation scales. The scalar derivative skewness $\left\langle(\partial\theta/\partial x_1)^3\right\rangle / \left\langle(\partial\theta/\partial x_1)^2\right\rangle^{3/2}$, which should be zero by local isotropy assumption, has been found to take values of the order of one as Reynolds number increases. Sreenivasan & Antonia (1977) found characteristic ramp-cliff structures in the temperature signal of a heated turbulent jet. The skewness caused by these structures appears to be constant for both shear flows and grid turbulence although the dependence of the skewness on Re_λ has not yet been systematically studied for a specific shear flow. The analysis of structure functions in a heated jet by Antonia & Van Atta (1978) showed a clear scaling range for the odd-order structure functions in the longitudinal direction, which should be zero due to local isotropy assumption at high Reynolds number. This illustrates that the anisotropy is not restricted solely to the dissipation range.

Sreenivasan & Tavoularis (1980) investigated the skewness of longitudinal temperature derivatives with different combinations of linear mean temperature gradients in various uniformly sheared flows. The magnitude of the skewness of the longitudinal temperature derivatives was non-zero only when both the mean velocity and temperature fields contained large scale non-uniformity. Their results confirmed that the non-zero value of the temperature derivative skewness in shear flows, such as the heated jet of Antonia & Van Atta (1978), was not consequence of large-scale intermittency of those flows. Tavoularis & Corrsin (1981*a*) and Ferchichi & Tavoularis (2002) showed that the skewness of the temperature derivatives has non-zero values in both the longitudinal and transverse directions in a USF with a mean temperature gradient. Their experiments were conducted in the narrow turbulent Reynolds number range $200 \leq Re_\lambda \leq 250$.

Budwig *et al.* (1985) and Tong & Warhaft (1994) examined the skewness of the temperature derivatives in a grid turbulence with an imposed uniform mean temperature gradient for a turbulent Reynolds number up to 130 and they found that the skewness was non-zero in the direction of the mean temperature gradient. These two sets of experiments had one fundamental difference. In the former experiment, the temperature gradient was in the streamwise direction along that the velocity field was inhomogeneous. In the latter experiment, the temperature gradient was in the transverse direction where the velocity field was isotropic. Both studies reported that the skewness of the temperature derivatives was approximately constant with an absolute value close to 1.5. Mydlarski & Warhaft (1998) used an active grid and a uniform mean temperature gradient for Re_λ up to 731. They measured the skewness of the transverse temperature derivative and concluded that it is independent of Reynolds number. It is important to notice that in the presence of a large scale temperature non-uniformity in shear flows, the skewness of both the longitudinal and the transverse temperature derivatives show non-zero values. However, in grid turbulence there is only skewness in the transverse direction (*i.e.* the direction of the mean temperature gradient).

These experimental results were supported by the numerical results of Holzer & Siggia (1994), which showed ramp-cliff structures in the scalar field in which mean temperature gradient were embedded in a two dimensional purely Gaussian velocity field. This suggested that the ramp-cliff structure could be an inherent characteristic of scalar fields.

Finally, much of the evidence about scalar intermittency is collected by investigating fourth order moments of the scalar derivatives. The combined results of the both shear-flow data (Sreenivasan & Antonia, 1997) and grid turbulence scalar experiments (Mydlarski & Warhaft, 1998; Tong & Warhaft, 1994) showed that the kurtoses of the temperature derivative in the longitudinal and transverse directions increase with Re_λ.

3.3 Data convergence

The convergence of the fluctuating statistics is a crucial issue in this study. The following is a brief review of recent literature, with focus on the convergence of the velocity and temperature statistics. Garg & Warhaft (1998) used 8×10^5 samples as a typical length of their velocity time series in a USF. The sampling rate were set at twice the low-pass filter cut-off frequency. The measurements for the PDF were spaced at about an integral scale apart to provide statistical independence and a typical length of a record was about 123000 samples. Derivative statistics were determined for a wire spacing that was between 2 and 3 Kolmogorov microscales. The results in this study showed that the derivative PDF to the third order were not fully converged for the case with a turbulent Reynolds number of about 150.

Shen & Warhaft (2000) used $10^7 - 10^8$ data points to measure high-order velocity derivative moments in a USF. To obtain 10^8 data points, they collected data over 8 hours, while monitoring the airflow temperature to ensure its constancy. Measurements of parameters in the inertial range converged better than derivative statistics. They used 10^7 data points for PDF and 10^6 point for each point in the structure function. They argued that a sensor separation distance 5η was proper for measuring $\partial u_1/\partial x_1$ and $\partial u_1/\partial x_2$, because the dissipation spectrum peaks at about $x_2/\eta \approx 10$ (Mydlarski & Warhaft, 1998). Their results showed no convergence problem for the third to fifth moments, while the sixth and seventh moments had a large uncertainty.

Gylfason & Warhaft (2004) used $8\times10^6 - 2\times10^8$ samples for measuring the statistics of longitudinal temperature derivatives and 4×10^5 data points for transverse statistics in grid turbulence with a uniform mean temperature gradient. They also used 8×10^6 data points for their velocity field. For the transverse statistics, the sampling rate was set at 400Hz in all of their measurements. This low frequency was used to obtain independent data points for the determination of moments.

In summary, the convergence analysis in the previously mentioned studies has shown that data sets with population sizes of the order of 10^8 samples were fully converged to the third and fourth order derivative statistics. These studies also suggest that derivative data sets with less than 10^6 samples are not appropriate for the analysis of the third and fourth order moments due to incomplete convergence (Garg & Warhaft, 1998).

3.3.1 Summary

The previous literature review has indicated that, although there are a great deal of experimental results on scalar transport, previous experiments were mostly performed in different experimental facilities at different turbulent Reynolds numbers and using different measurement methodologies; these differences tend to introduce an uncertainty in the comparison of results. More specifically, it was found that there is no experimental study that specifically and systematically investigates the effects of scalar inhomogeneity on the transport and the fine scale structure of scalar fields in turbulent flows. In summary, we have identified the following issues that have not been resolved adequately and seem to be worth further study.

- The current consensus among scalar PDF modellers is that scalar fluctuations would have a Gaussian PDF in the centres of scalar mixing layers, but this assumption has not been fully supported by the available experimental data. Moreover, the source of non-Gaussianity, when it exists, has not been identified.

- Scalar fluctuations in the centres of passively generated scalar plumes are known to have measurable non-Gaussianity, but an adequate explanation for this fact is lacking.

- The shapes of previously measured expectations of velocity components, conditioned upon the scalar value, have been inconsistent. In some cases, the edges of these expectations had very large uncertainties, as a result of the relatively small populations of collected samples.

- The shapes of the conditional expectations of the scalar dissipation rates and their dependence on the scalar field characteristics also remain uncertain. Most published studies do not report simultaneous measurements of all three components of the dissipation rate, and in some cases the spatial and temporal resolutions of the scalar derivative measurement techniques were not completely adequate. The question whether a single component of the scalar dissipation rate can act as a surrogate of the total, particularly in inhomogeneous scalar fields, remains without a satisfactory answer.

The previous issues have been investigated systematically in this study. All experiments were conducted in the same turbulent field, which is nearly homogeneous but highly anisotropic. Three different scalar fields with different levels of complexity (one homogeneous and two inhomogeneous) were superimposed passively on a USF at a fixed turbulent Reynolds number. This let us, in particular, to eliminate the effects of turbulence inhomogeneity and external intermittency and to separate the effect of scalar inhomogeneity from the effect of scalar initial conditions.

Chapter 4

Experimental facilities, instrumentation and measurement procedures

4.1 Wind tunnel

All experiments were conducted in the open-circuit wind tunnel at the Fluid Dynamics Laboratory, University of Ottawa (see fig. 4.1). This wind tunnel had a 16:1 contraction and a test section with a height h = 0.305 m and a length of $16.6h$. The width of the test section was fixed at $1.5h$ for an upstream length of $2h$, following which it was increased linearly to compensate partially for boundary layer growth so that the centreline velocity would be approximately constant.

Air filters (Camfill Farr, 30/30) were placed at the inlet of the wind tunnel to remove particles suspended in the oncoming air. The particle removal ratio of the filter was 82 % for 8.4 μm particles and decreased linearly to 10 % for 0.5 μm particles. The flow was produced by a mixed flow fan (Woods, model 63Mx, 630 mm

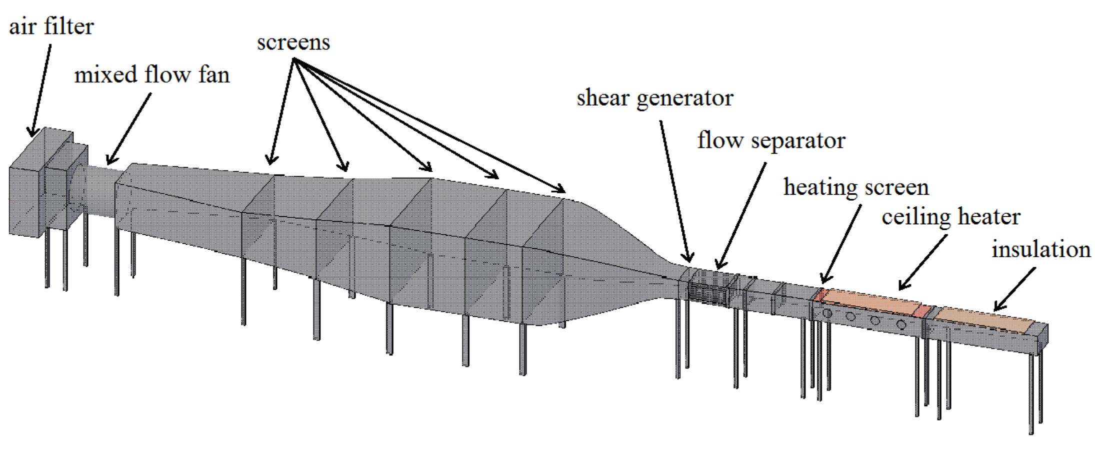

Figure 4.1: The open-loop wind tunnel facility.

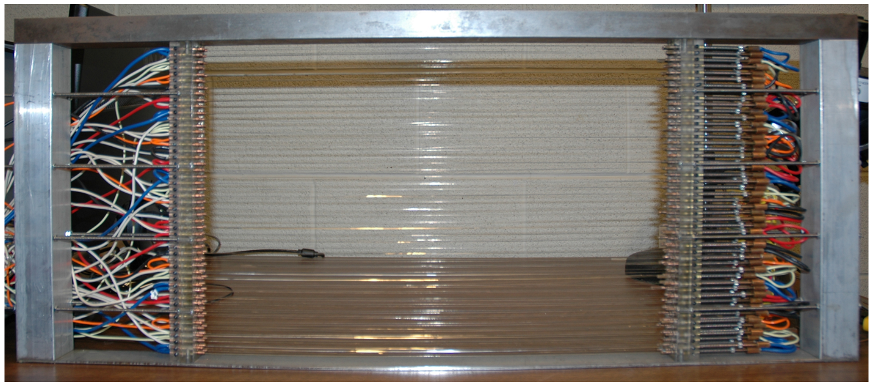

Figure 4.2: Heater

diameter), operated by an electric motor with a variable frequency drive (Mitsubishi Electric Inverter, Model FR-D700). A LabVIEW interface was developed to control the motor speed, the traversing system positioning, and the data acquisition during measurements. The unobstructed wind tunnel could operate at a maximum velocity of about 30 m/s and a turbulence intensity of less than 0.5 %. The pressure drop along the contraction was monitored at all times to detect possible variations of the wind-tunnel velocity during measurements.

A turbulent flow with a nearly uniform shear was generated by the same shear generator/flow separator apparatus used by Tavoularis & Karnik (1989), Ferchichi & Tavoularis (2000) and Ferchichi & Tavoularis (2002). The shear generator consisted of an array of 12 parallel channels, each containing a number of screens with different solidities. It was followed by a flow separator, comprising additional unobstructed lengths of the same parallel channels, which straightened the stream and ensured uniformity of the initial length scales. The height of each channel, including the half-thicknesses of the separating plates on either of its sides, was $M = 25.4$ mm.

Passive heating of the flow was provided by a screen consisting of 49 pairs of electrically heated ribbons (0.1 mm ×0.8 mm) of Nichrome alloy spaced by 6.1 mm in the transverse direction (Fig. 4.2). Each pair of ribbons was separated by 9 mm in the streamwise direction such that the downstream ribbon was in the wake of the upstream one; this arrangement was designed as to allow the injection of as much heat as possible into the flow without introducing significant flow disturbance. The

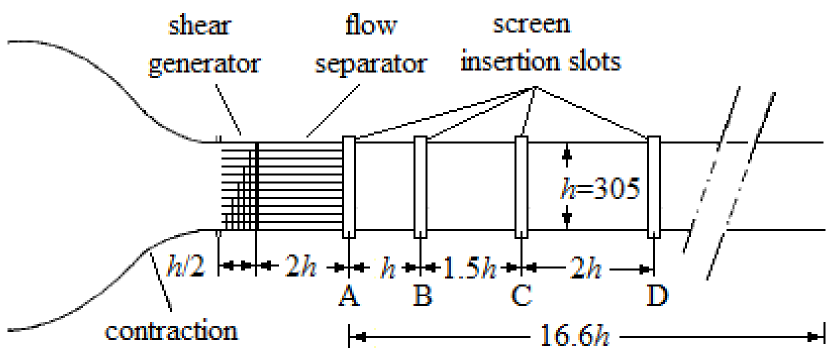

Figure 4.3: The positions of insertion slots.

insertion slots for the heating screen are shown in Fig 4.3.

The test section was equipped with a 3-axis traversing system, capable of travelling in the streamwise and vertical directions throughout the test section; spanwise traversing was also possible at specific locations that coincided with the screen insertion slots (Fig. 4.3). Probes were traversed in the transverse direction with the use of a linear positioning device with a resolution of 0.005 mm. Streamwise traversing of the probes was done manually along a traversing system with a resolution of 0.5 mm. Additional information on wind tunnel components is provided by Karnik & Tavoularis (1987).

4.2 Probe repair equipment and calibration facilities

Probe repair equipment: The sensors of hot-wire and cold-wire probes were extremely fragile and occasionally were broken or burnt during probe handling or during measurements. The repairs of hot-wire and cold-wire probes were conducted by the author using a spot welding apparatus (Dantech 55A12/13). Welding energy was discharged through an electrode from a welding generator (Dantec 55A12), capable of discharging up to 300 mJ of electric energy in 100, 200 or 400 μs. It was found that setting the welder to discharge 40-60 mJ in 200 μs worked well for welding 2.5 μm Tungsten hot-wire sensors, whereas discharging 20-30 mJ in 100 μs was proved to be the best welding settings for 0.63 μm 90%Pt/10%Rh sensors used for cold-wires.

Before welding, the tips of the cold-wire prongs were polished carefully with microcut silicon carbide grinding paper (1200/P2500). The same grinding paper was used first to sharpen the tip of the welder electrode to less than 30 μm across; this was followed by polishing this tip with a polish pad (Struers MD Chem, 0.04 μm) to remove all possible impurities from it. Such a sharpened and polished tip was capable of pressing the 0.63 μm wire to the prong surface. A 0.05 μm colloidal silica solution was also used during the polishing procedure.

Calibration jet: This facility has been described in detail by Bailey (2006). Low turbulence, uniform airflow, generated by a nozzle unit (Dantec 55DH5), was used for velocity calibration of hot-wires. The unit had a circular plenum with an area of 2827 mm^2 and was equipped with four interchangeable nozzles having exit areas 120, 60, 24 and 12 mm^2. Air velocities that ranged up to Mach 1 could be generated, depending on the nozzle being used. For directional calibration of the hot-wire probes, only the 120 mm^2 nozzle was used, giving a maximum exit velocity of approximately 35 m/s with an area ratio of 22.8. A 689 kPa (100 psi) compressed air line was used as an air source. The velocity at the exit plane of the jet was calculated from the pressure difference ΔP (in Pa) along the nozzle using the Bernoulli equation

$$U_{noz} = \frac{A_{noz}}{1 - (A_{noz}/2800)} \left(\frac{2\Delta P}{\rho} - 2gH_{noz} \right)^{0.5}, \tag{4.1}$$

where A_{noz} is the nozzle exit area in mm^2, ρ is the air density in kg/m^3, and H_{noz} = 0.085 m is the elevation difference between the nozzle exit and the plenum pressure tap. The calibration jet was equipped with a rotary table for directional calibration of the hot-wire probes. Angular position was adjusted using two rotary tables (Velmex B5990TS) driven by stepper motors (Vexta PK245-01AA), which were controlled by a motor controller (Velmex NF90). Positioning resolution with these rotary tables was nominally 0.01°, however, the positioning uncertainty was 0.05° because of backlash within the rotary tables (Bailey, 2006).

The calibration jet flow could be heated with the use of a resistance heater mounted upstream of the nozzle inlet and powered by a variable transformer. This

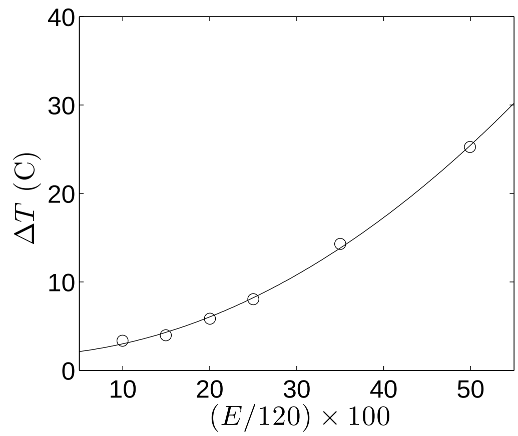

Figure 4.4: Air temperature rise across the heated calibration jet vs. input voltage of the resistance heater in Volt for a jet velocity of 7.5 m/s; solid line: $\Delta T = 0.0086V^2 + 0.046V + 1.7$.

capability was used for calibrating thermistors and cold wires and for determining the resistance-temperature relationship of hot wires. A representative variation of air temperature rise in the jet vs. the transformer voltage is plotted in Fig.4.4.

Ultra cryostat circulator: An Ultra Cryostat Circulator unit (Colora, Model KT90S) was used to maintain the compressed air temperature constant during the calibration of thermistors. The unit had a bath of antifreeze coolant (a glycol solution); the temperature of the bath was kept below ambient by the cooling system of the unit with a resolution of 0.01 K. The circulating pump of the unit maintained uniform temperature throughout the bath. The compressed air, which was passed through a 12 m long copper coil immersed in the bath, reached the calibration jet inlet with a temperature variation that was less than 0.2 K during the calibration of thermistors.

4.3 Data acquisition systems

UEI data acquisition system A UEI PD2 MFS-8-300/16 PowerDAQ acquisition card was used at the early stage of measurements performed in this study. This card could perform simultaneous sampling of up to eight analogue input channels. It was capable of performing analogue-to-digital conversion with a resolution of 16-bit at up to 300 kHz for a single channel or 37.5 kHz for all eight channels. Input voltage ranges were user selectable as either 0-5 V, 0-10 V, 5 V or 10 V.

NI PCI-6143 data acquisition system Two NI PCI-6143 acquisition systems were used for the majority of measurements. The devices were capable of performing simultaneous analogue to digital conversions with 16-bit resolution for up to eight channels. A maximum sampling rate of 250 kHz per channel was possible with these cards. The range of input voltages was from -5 to 5 V. The analogue signals were fed to the data acquisition cards using two shielded connector blocks (NI BNC-2110). The blocks also provided the capability of sharing the start clocks and the sample clocks of the cards externally using a BNC cable. This capability was used to synchronize the two NI PCI-6143 cards when synchronization was required. The data acquisition cards were also capable of being internally connected through a RTSI bus cable to share their internal clocks.

NI cDAQ-9171 data acquisition system A NI cDAQ-9171 1-slot USB chassis was used with a four-channel analogue input module NI 9217 to run and acquire the analogue signal of a 100 Ω RTD sensor. The maximum sampling rate was up to 400 Hz per channel. This data acquisition system had a 24-bit resolution with a 50/60 Hz noise rejection module and was capable of operating both 3- and 4-wire RTDs.

4.4 Pressure, reference temperature and air density measurement

Pressure: Two pressure transducers were used in the course of this study. The first one (Furness Controls, Model FCO332) had a selectable range between either 0 to 250 Pa or 0 to 2500 Pa and the second one had a range from 0 to 50 Pa; both of them had a specified uncertainty of 0.025% of the full range. The former transducer was used with a Pitot tube for calibration of the cross-wires and the latter one was used to measure pressure difference along the wind tunnel (16:1) contraction for monitoring the speed of the wind tunnel during the measurements. Both pressure transducers provided analogue outputs in the range 0 to 5 V and were also equipped with digital

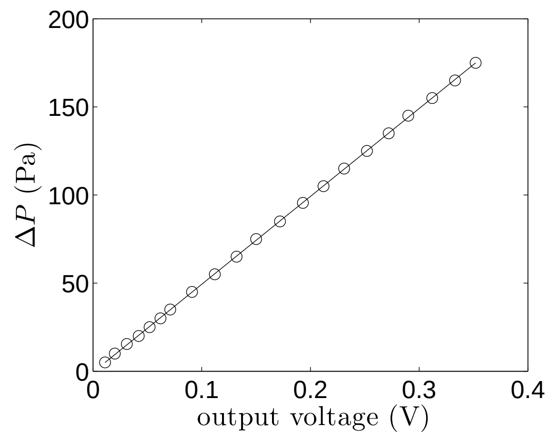

Figure 4.5: Typical pressure transducer calibration curve; solid line: the best fit to the experimental data using linear least-squares method.

displays. A typical calibration curve of the first pressure transducer for the range 0 to 250 Pa is shown in fig. 4.5.

Reference temperature measurement: The mean temperature upstream of the heating screen was monitored with the use of a platinum resistance temperature detector (RTD, Model 29348-T01-B-48, RDF Corp.), precision-calibrated and embedded in a micro-capsule made of stainless steel with 1.67 mm diameter. The thermistors (see the next section) used in this study were calibrated against this RTD in the calibration jet. The reported time constant of the RTD was 0.4 s at 0.91 m/s water flow. The excitation current of the data acquisition system that operated the RTD was 1 mA, which is much lower than the maximum permissible current of 5 mA for negligible self-heating. The manufacturer measured the resistance of the RTD in an oil bath for the range between 0 to 100°C with 1°C increments. The best fit was represented by the equation $R = R_0(1 + A(T - B(T/100)(T/100 - 1)))$, where R is the resistance of the RTD in Ohm, T is the temperature in °C, R_0=100.01 Ω is the resistance of the RTD at 0 °C, A =0.003852, and B=1.522592. The specified uncertainty of the RTD was 0.1 K.

Air density: A weather forecast board was used to measure the density of ambient air. The board had a digital pressure sensor (BOSCH, model BMP085) to measure the local ambient pressure with a specified uncertainty of 100 Pa. The local ambient temperature and humidity were measured using a digital sensor (SENSIRION, Model SHT1x) with manufacturer-specified uncertainties of 0.3 °C and 2 %, respectively. The air density ρ was calculated using the equation $\rho = P_d/(R_d T) + P_v/(R_v T)$ where T is measured at the tunnel inlet, P_d is the partial pressure of dry air, P_v is the partial pressure of water vapour, R_d is the specific gas constant for dry air equal to 287.058 J/(kgK), and R_v is the gas constant for water vapour, equal to 461.495 J/(kgK). P_v was calculated using the following equation (Jones, 1995)

$$P_v = H \times 610.78 \times 10^{7.5T/(T+237.3)} \tag{4.2}$$

where H is the humidity and T is in °C. The partial pressure is $P_d = P - P_v$, where P is the ambient pressure measured using the pressure sensor. The sampling rate of the weather forecast board was 0.2 Hz.

4.5 Thermistor thermometry

Thermistor probes: Two glass thermistor mini-probes, (EPCOS B57540 series 10 kΩ 1% RAD), shown in Fig. 4.6, were used in the course of this study. Thermistors

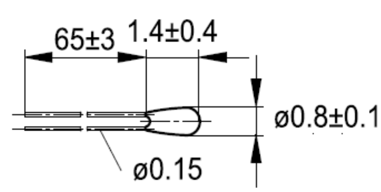

Figure 4.6: Sketch of the glass thermistor. All dimensions are in mm.

were used to measure the local mean temperature of the flows for two purposes (i) calibration of cold-wire probes (either in-situ calibration in heated flows or calibration in the jet) and (ii) correction of hot-wire readings for the variation of the flow temperature, using a modified King's law (Tavoularis, 2005). The thermal cooling time constant of the thermistor probes was lower than 1 s. The dissipation factor ϵ_{th} of the thermistors was 0.4 mW/K. For operation with an excitation current of $i_{excitation} \simeq$

50 μA provided by home-made circuitry, the self-heating of the thermistors was about 0.06 °C, as calculated from the following equation:

$$\Delta T_{self\_heating} = (RI^2)_{thermistor} / \epsilon_{th}. \tag{4.3}$$

Thermistor circuitry: An existing custom-made circuit, shown in fig. 4.7, was modified to run thermistors and provide output amplification in the range from 0 to 5 V. The resistors of the bridge were changed to power the 10 kΩ probes and also a voltage follower was added before the bridge to prevent voltage drop due to the current draw. The gain and the offset were adjusted by the two adjustable resistors R_9 and R_{10}, respectively.

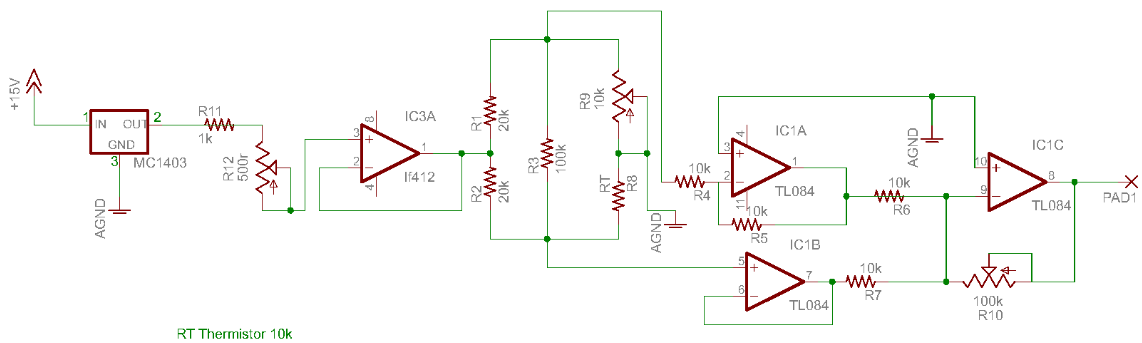

Figure 4.7: Thermistor circuit.

Calibration method: The output voltage of the thermistor circuit was calibrated against the pre-calibrated RTD in the calibration jet. To bring the temperature of the compressed air below the ambient temperature, the compressed air was passed through a 12 m copper coil which was placed in a bath of glycol solution cooled by the Ultra Cryostat Circulator unit (see Sec. 4.2); and then the flow was passed through the resistance heater, which adjusted the temperature to the desired level. One of the main advantages of this arrangement was that the inlet flow temperature of the jet was sufficiently stable (with less than 0.2°C) to be measured accurately by the pre-calibrated RTD, which had a relatively slow temporal response. The circuit output E_{th} in Volt could be described by the expression $T = 0.9376E_{th}^2 + 14.4934E_{th} + 54.1510$ where T is the air temperature in °C. The thermistors were calibrated at a flow speed

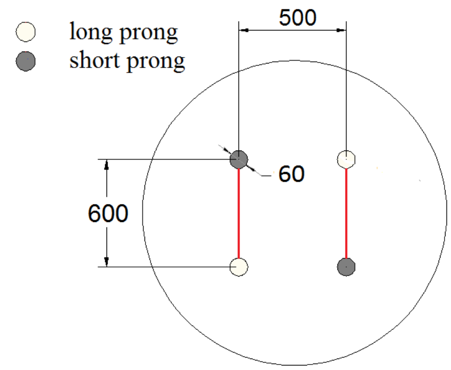

Figure 4.8: Sketch of the cross-wire probe. All dimensions are in μm.

of 7.5 m/s, which was comparable to the velocity at which the measurements were performed. Readings of the thermistors were compared with the reading of the RTD at different velocities in the wind tunnel and the difference was found to be less than 0.1 °C; this shows that self-heating of the thermistors was indeed negligible. The resolution of the thermistors, which was limited only by the electronic noise of the circuitry, was 0.01°C.

4.6 Hot-wire anemometry

Hot-wire probe: A cross-wire probe was used for velocity measurements in this investigation. This probe was custom-built, with a 0.6 mm separation distance between the prongs of each sensor and a 0.5 mm separation distance between the planes of the two sensors (Fig. 4.8). The tips of the prongs were tapered to 60 μm diameter. Sensors were made from 2.5 μm Tungsten wire welded onto the probe prongs and had a length of approximately 0.85 mm, which resulted in a length-to-diameter ratio of $l_w/d_w = 340$. The recent study of Li *et al.* (2004) showed that for sensors made of Tungsten wire conduction effects would be negligible for $l_w/d_w \geq 270$. The total resistance of each prong and lead wire for each sensor was 4.4 Ω and the cold resistances of the sensors were found to be in the range of 18.0 to 20.0 Ω, with the actual values varying for individual sensors.

Circuitry: The hot-wires in this study were operated by constant temperature circuits (A.A. Lab, model AN-1003), capable of operating at both 1:1 and 1:10 bridge ratios for sensors with maximum operating resistances of 99.9 Ω and 9.99 Ω, respectively. The frequency response of the anemometer depended on the probes used, with an upper cut-off frequency of up to 50 kHz, achievable through adjustment of circuit capacitance and inductance. The anemometer units had output signal conditioning, in the form of adjustable output gain and offset as well as an analogue filter with a selectable cutoff frequency, consisting of two double-pole low-pass filters. Due to the high impedance of the hot-wire sensors in this study, the feedback circuit of the anemometer was set to oscillations. Following previous attempts by Bailey (2006), it was determined that the frequency response of the circuit could be altered to restore circuit stability by changing capacitor C31 and C32 on the anemometer circuit (Manual, 1996). Through trial and error, it was found that by replacing the existing 2.2 nF and 0.1 nF capacitors with an 0.82 nF and 10 nF capacitors, respectively, the circuit oscillations were eliminated and a high frequency response was maintained.

Calibration method: The relation between the anemometer bridge output E_i and the effective cooling velocity V_{eff} was determined using the modified King's law (Tavoularis, 2005)

$$\frac{E_i^2}{T_{wi} - T_\infty} = A_i + B_i V_{effi}^{n_i}, \tag{4.4}$$

where i indicates the individual sensor, T_w is the sensor temperature, and T_∞ is the free-stream temperature. The calibration of the cross-wire was performed using the effective angle method, originally proposed by Bradshaw (1971). The detailed procedure of the calibration method has been described by Holloway (1989), Browne *et al.* (1989) and Bruun (1995). In this method, a yaw calibration was performed after each sensor repair to determine the effective angle of the individual sensor. It is noted that before yaw calibration the probes were run for more than one hour at 10 m/s with 1.5 OHR and checked for any possible wire stretch or deficiencies in the welding. In the course of measurements, except for possible initial stretches after welding, it was found that the wires kept their orientation until burnout or physical

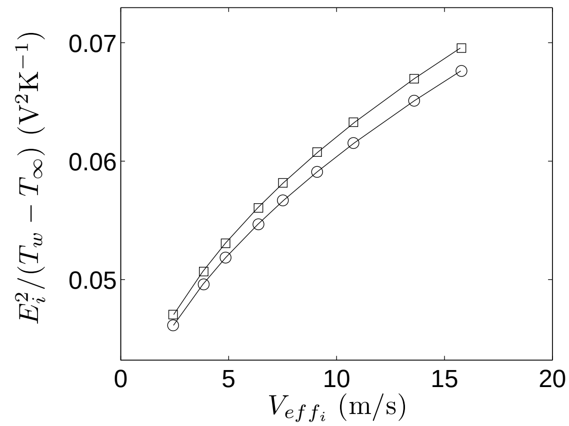

Figure 4.9: A typical calibration curve of the cross-wire. ○: sensor 1; □: sensor 2; solid lines: fitted curve using modified King's law.

damage. After yaw calibration, a velocity calibration was performed to determine the calibration constants, A_i, B_i and n_i before each measurement run. A set of representative calibration curves for the cross-wire sensors is shown in Fig. 4.9, with modified King's laws fitted to the data by least square fitting.

4.7 Cold-wire thermometry

Four-wire probe: A custom designed, quadruple cold-wire probe (fabricated by Auspex) was used to measure the temperature derivatives. The length and arrangement of the sensors are shown in Fig. 4.10. Lead resistance for each sensor was in the range 5.2 to 5.5 Ω. The sensors were made of 0.63 μm 90%Pt/10%Rh wire, having resistances in the range 260 to 310 Ω. The length-to-diameter ratios for each pair of parallel sensors were l_w/d_w = 635 and 730, respectively. The parallel sensors with the smaller separation were used to measure the temperature derivatives in the transverse direction (which was also the direction of the mean temperature gradient), while the parallel sensors with the larger separation were used to measure spanwise derivatives.

Circuitry: Four constant-current circuits, like the one shown in Fig.4.11, were used to power the cold-wire probes. The constant-current circuit, designed by S. Marineau-Mes, consisted of the following five blocks.

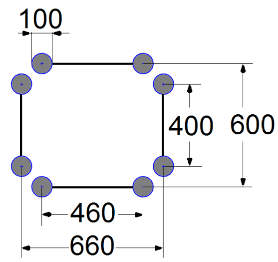

Figure 4.10: Sketch of the four-wire probe. All dimensions are in μm.

- **Block A**, which provided a precision voltage reference for the circuit. The Analog Devices AD586 chip was a precision 5 V voltage reference at a relatively low noise level (approximately 100 nV/Hz$^{1/2}$). A single-pole low-pass filter was connected to the voltage reference output.

- **Block B**, which generated a reference voltage in the 0-5 V range and provided a constant-current source for the probe. Analysis showed that the current to the probe was given by $i_p = -V_a/R$, where R is a 2 kΩ resistor. Thus the current through the probe was in the range $0 - 2.5$ mA. The current used in this study was 0.15 mA.

- **Block C**, which is similar to block B, except that instead of the probe it has a 100 Ω resistor. This value was proper for the 1 μm (90%Pt/10%Rh), which had a resistance near 100 Ω. For the 0.63 μm wires this resistor was replaced with a 300 Ω resistor, as necessary to balance the circuit. The advantage of this arrangement was that drift and noise in the reference voltage would be tracked by both the probe and the offset circuit identically, thus leading to common mode rejection.

- **Block D**, which represents the instrumentation amplifier. The Analog Devices AMP-01 was a low-noise precision amplifier. The overall gain could be varied from 0.1 to 1000 with a minimum dynamic response of 26 kHz for the highest gain. A proper combination of the resistors R_s and R_g provided a desired gain, as listed in the table inserted in Fig. 4.11.

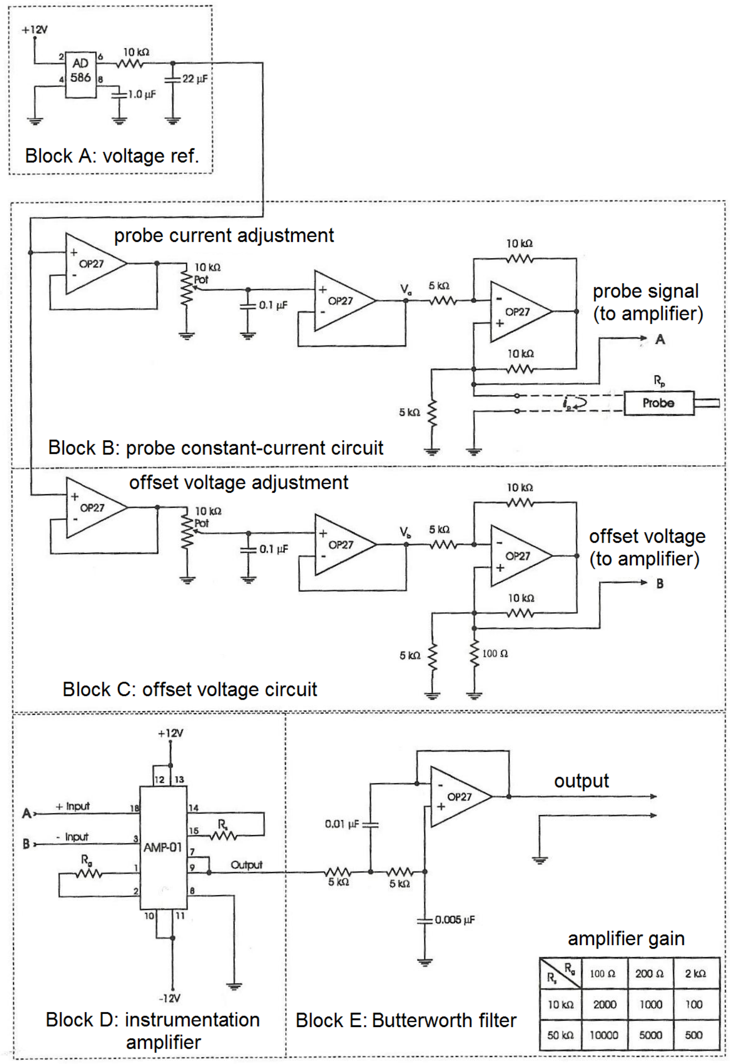

Figure 4.11: Constant-current circuit for cold-wire probes (S. Marineau-Mes, 1997).

- **Block E**, which is a second-order Butterworth filter, intended to eliminate aliasing effects when sampling the output signal. The corner frequency of the circuit could be changed by replacing the capacitors of the filter. In this study, the cut-off frequency of the filter was set at 8 kHz using 4.7 pF capacitors.

Calibration method: The outputs of the cold-wire circuits were calibrated against a pre-calibrated thermistor in the calibration jet. This preliminary calibration was performed to examine the overall performance of the sensors. As shown in Fig. 4.12 calibration results were fitted well by linear expressions. It was verified that the

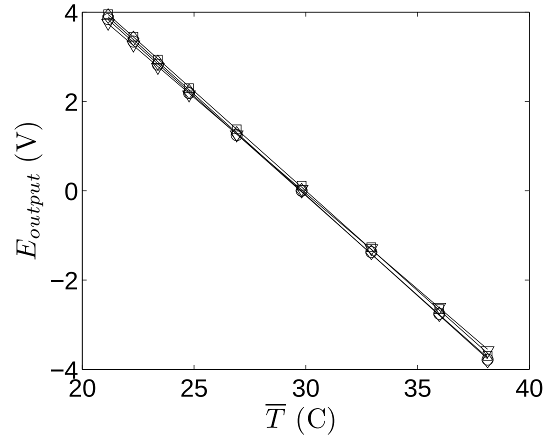

Figure 4.12: Typical calibration curves of the quadruple cold-wire probe; ∘: wire 1; □: wire 2; ⋄: wire 3; △: wire 4, solid lines: linear least squares fits.

cold-wire outputs did not show any measurable sensitivity to the mean velocity for velocity range considered in this study. After a preliminary calibration, an in-situ calibration was performed in the heated flow during each test. For in-situ calibration, both the cold-wire probe and the thermistor were mounted on the traversing system at the same level. A cathetometer with a resolution of 0.05 mm was used to ensure that the tips of the cold-wire and the thermistor were at a same horizontal plane. As the final step of calibration, the outputs of the cold-wires were calibrated against the thermistor for different mean temperatures across the scalar fields. All cold-wires and the associated electronic circuits were calibrated at the same time to minimize relative errors in the calibration of the sensors. To eliminate the effects of drift in the cold-wire output, which is unavoidable because of the high amplification gain used, only temperature fluctuations were measured with cold wires, whereas the local mean temperature was measured by the thermistor. Thus, the instantaneous local temperature value was represented by the sum of a mean, measured by the thermistor as a time average, and a mean-free fluctuation, measured by a cold-wire.

4.8 Simultaneous velocity-temperature measurements

Three-wire probe: A custom-made three-wire probe (by Dr. Petar Vukoslavčević) consisting of a cross-wire and a cold-wire was used for simultaneous point-measurement of the fluctuating velocity-temperature statistics. A sketch of the probe is shown in Fig. 4.13. The temperature sensor was placed so that it was slightly upstream of the middle of the cross-wire to reduce thermal interference from the hot-wires. Vukoslavcevic & Wallace (2002) showed that, for velocities higher than 2.5 m/s and a 0.5 mm separation distance between the cold and hot sensors, the effects of hot-wire sensors on the temperature sensor were negligible. In their study, the hot-wire sensors of the three-wire probe were made of 90%Pt–10%Rh, for which the wire temperature exceeded 300 °C even for the relatively low overheat ratio (OHR) of 1.5. Mydlarski & Warhaft (1998) used 0.5 mm spacing between their hot (3.05 μm tungsten wire) and cold (0.63 μm 90 %Pt–10 %Rh) sensors in a flow with a Batchelor microscale η_θ = 0.3 mm. In their study, the tungsten wires were operated at an OHR of 1.8, which resulted in a temperature rise of about 200 °C. For the previous estimates, the wire temperatures were calculated by assuming that the thermal resistivity coefficient α_r was 0.0048 for tungsten and 0.0016 for 90%Pt–10%Rh wires, as specified by Sigmund Cohn Corp.

In the present study, we chose Tungsten for the cross-wires rather than a platinum alloy. The temperature rise of the Tungsten sensors was estimated to be lower than 150 °C for the overheat ratio of 1.5 used in this study; this value is much lower than the temperature rise that Pt–alloy wires would have, if such were used instead. In order to achieve higher sensitivity to velocity variations, it would have been desirable

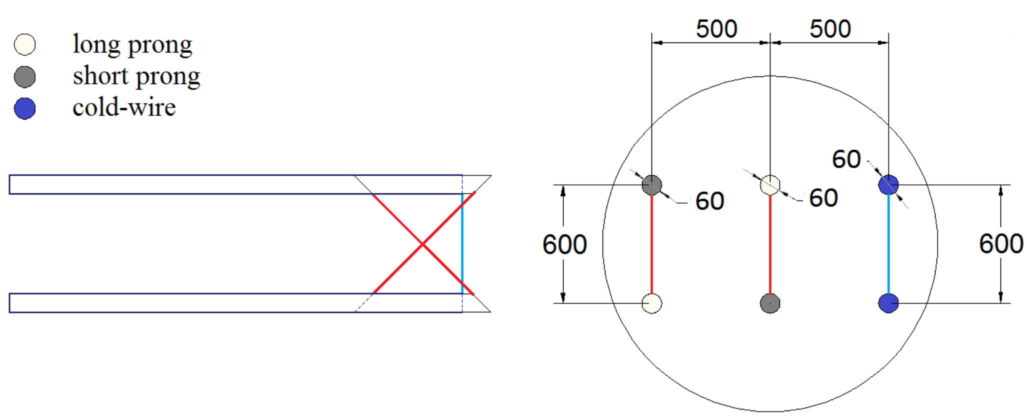

Figure 4.13: Sketch of the three-wire probe. All dimensions are in μm.

Table 4.1: Combined resistance of the prongs and lead wires for the three-wire probe.

prong number	1	2	3	4	5	6
resistance in Ω	7.9	8.1	8.3	7.9	8.0	8.1

to operate the sensors at a higher OHR, but this was avoided because it was found during preliminary tests that, for OHR higher than 1.5, the resistance of the wires changed after some use. The resistances of the welded wires were in the range from 18 to 20 Ω following each repair. The combined resistances of the prongs and lead wires, measured before welding, have been listed in table 4.1. The cold-wire was made of 0.63 μm 90%Pt–10%Rh material. The sensors had $l_w/d_w \simeq 950$ and resistances ranging from 335 to 360 Ω following each repair. To ensure that the current flowing to the hot-wires in the three-wire probe did not affect the reading of the cold-wire, the mean and higher order moments of the temperature signal were compared in heated flows with the hot-wires switched on and off and were found to have no measurable difference.

Circuitry and calibration method: The same circuitries and the same calibration procedures, as those described in the Sec. 4.6 and Sec. 4.7, were used to run and calibrate the cross-wire and the cold-wire of the three-wire probe.

4.9 Measurement procedures and uncertainties

4.9.1 Measurement procedures

The mean temperature upstream of the heating screen, monitored with the use of an RTD, was subtracted from all other measured temperatures to provide the reported temperature rises, which were insensitive to room temperature fluctuations. Additionally, a thermistor probe was mounted on the traversing system at the same level as the three-wire probe and was used to measure the local mean temperature at each measurement location downstream of the heater. The hot-wire signals were corrected for variations of the mean temperature, measured by the local thermistor, and for instantaneous temperature fluctuations, measured with the cold wire, with the use of a modified King's law (Tavoularis, 1983, 2005).

The hot- and cold-wire signals were low pass filtered at 10.4 and 8 kHz, respectively, and sampled simultaneously at a rate of 22 kHz. The filtered signals were digitized using a 16-bit National Instrument (PCI 6143) data acquisition system. Before processing, the time series were filtered digitally using a double-pass, seventh-order, Butterworth, low-pass filter, with a cut-off frequency that was adjusted at each location to the local Kolmogorov frequency $f_k = \overline{U}_1/(2\pi\eta)$. For example, at the high speed region of the USF with $\overline{U}_1 = 11$ m/s, the Kolmogorov frequency was estimated to be about 7.0 kHz. Time series consisting of 5.5×10^5 samples were recorded for calculating time-averaged profiles, whereas longer ones, consisting of 1.1×10^8 samples, were recorded separately for calculating PDF and conditional expectations. Each of the latter time series extended over 83 min and was divided into 2.5×10^3 segments. Each segment was long enough to represent adequately the longest time scales of turbulent motion (namely, more than 200 times the velocity integral time scale) and short enough not to be influenced by possible wind tunnel speed fluctuations, hot/cold-wire voltage drift and room temperature variations. For example, non-stationarity of room temperature is accounted by computing averages in such segments of sufficient but not excessive duration.

4.9.2 Velocity fluctuation measurement uncertainty

The spatial filtering effects of hot-wire probes have been extensively investigated for wall-bounded flows (Smits *et al.*, 2011) using a Nano-Scale Thermal Anemometry Probe (NSTAP). Ashok *et al.* (2012) performed a similar investigation in grid turbulence and showed that spatial filtering in the near wall region of a wall-bounded flow is remarkably similar to the filtering seen in grid turbulence, in spite of the anisotropy of turbulence in wall-bounded flows. In their study, they discussed the effects of the spatial filtering on the estimates of the variance, dissipation rate, Kolmogorov length scale, integral length scale, and power spectrum of velocity fluctuations. They showed that the ratio l_w/η scales the spatial filtering of the variance of longitudinal velocity fluctuation very well. Their results suggested that the filtering is quite evident at high as well as low wavenumbers, but for $l_w/\eta < 2$ the effects of spatial filtering on estimates of the variance, dissipation rate and Kolmogrov length scale would be negligible, whereas the spectra would be unaffected when $l_w/\eta < 5$.

In the present study, the ratio l_w/η always remained below 3.4. The effect of spatial filtering on estimates of the variance, dissipation rate, integral and Kolmogrov length scales was estimated to be less than 5 %, as estimated in accordance with the Ashok *et al.* (2012) study. Temporal filtering was not expected to be an issue in the present study, as hot-wires were operated in a constant temperature mode (Li, 2004, 2006), with additional use of the optional high frequency compensation circuitry provided by the anemometer manufacturer.

4.9.3 Measurement uncertainty of temperature fluctuations

The operational amplifiers used in the cold-wire circuits (section 4.7) provided r.m.s. signal to noise ratios of above 50 in all long-run measurements. The equivalent rms temperature fluctuation measured by the cold wire in the unheated flow was about 0.001 K in the course of measurements. Assuming that the noise was independent of temperature fluctuations so that the noise and temperature fluctuation contributions to the signal could be added in the mean square, one may determine that the noise effect on the measurement of temperature was entirely negligible, so that no correction would be necessary.

For an accurate measurement of temperature fluctuations, the cold-wire sensors should have sufficient temporal and spatial resolution to capture the small scale characteristics of the temperature fields. The temporal resolution of a cold-wire is mainly determined by the frequency response of the circuit, the convective velocity of the flow, and the thermal response of the wire itself, which depends on the wire material, diameter and length. LaRue *et al.* (1975) showed that a new 0.63 μm Pt wire had a

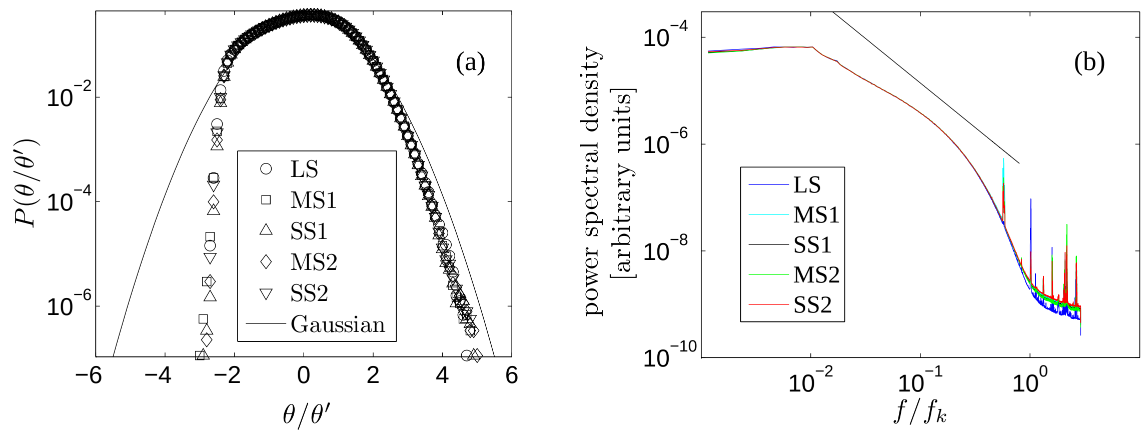

Figure 4.14: (a) PDF of temperature fluctuations and (b) temperature spectra at the centre of the PLS measured simultaneously by all five cold-wire sensors; black solid line represents -5/3 slope; f_k represents the local temperature microscale.

roll-off frequency of approximately 5 kHz in a flow with a speed of 7.5 m/s. For cold-wires with $l_w/d < 1500$, end conduction would be a significant source of error for the measurement of temperature fluctuations (Browne & Antonia, 1987). Consequently, attempts to improve the spatial resolution of cold-wire probes by using shorter sensors would result in an increase in the end conduction error. To achieve a sufficiently large l_w/d while also keeping the sensor length within an acceptable range, we used wires with a diameter of 0.63 μm, as thinner wires would be extremely difficult to mount to the prongs and operate in the flow. In the present study, we used five 90%Pt–10%Rh cold-wire sensors. They all had a diameter of 0.63 μm but three different lengths: one longer sensor (LS) in the three-wire probe with $l_w/d_w = 950$, a pair of intermediate–length parallel sensors (MS1 and MS2) in the quadruple-wire probe with $l_w/d_w = 730$ (used to measure the transverse temperature derivative) and a pair of shorter sensors (SS1 and SS2) with $l_w/d_w = 635$ (used to measure the spanwise temperature derivative). As a first comparison of the performances of all cold–wires, Figure 4.14 shows frequency spectra and PDFs of scalar fluctuations measured simultaneously by all five sensors in the centre of the plume of a heated line source at $x_1/h = 10$. The forms of the PDFs were almost the same (figure 4.14a). All spectra collapsed (figure 4.14b) except at frequencies near the Kolmogorov frequency, where the LS sensor measured

Table 4.2: Ratios of moments of the temperature and its temporal derivative measured by cold-wires of two different lengths at the centre of the plume ($x_1/h = 10$).

n	2	4	6
$\frac{(\overline{\theta^n})_{LS}}{(\overline{\theta^n})_{SS}}$	1.01	1.03	1.08
$\frac{\left(\overline{(\partial\theta/\partial t)^n}\right)_{LS}}{\left(\overline{(\partial\theta/\partial t)^n}\right)_{SS}}$	0.96	0.91	0.79

values that were somewhat lower than those measured by the shorter sensors, in agreement with findings by Mydlarski & Warhaft (1998). A spike occurred in the scalar spectra at a frequency of about 3 kHz. Such spikes have also been encountered in previous experimental and analytical studies (Tavoularis, 1978; Tatarskii *et al.*, 1992; Mydlarski & Warhaft, 1998). Warhaft (2000) attributed this spectral spike to the Fourier transform and postulated that its presence in the spectra does not affect the second-order structure functions (Warhaft 2000). Insight into this phenomena, which is essentially analytic, is provided by Lohse & Muller-Groeling (1996) for the velocity field. However, further investigation is required to address this issue in temperature fields which is beyond the scope of this study. Table 4.2 shows that ratios of the second, fourth and sixth moments of the temperature measured by the longer and shorter sensors increased with moment order. This trend may be attributed to end conduction effects, which are stronger for the shorter sensor, in agreement with the findings of Mydlarski & Warhaft (1998). In any case, the difference for the temperature variance was 1%, which is negligible for the present purposes. To keep errors at the lowest possible level, only temperature statistics measured by LS will be reported in the following chapters.

4.9.4 Measurement uncertainty of temperature derivatives

Figure 4.15 shows that differences among time derivative spectra measured by all sensors of the four-wire probe at the centre of the plume at $x_1/h = 10$ were negligible. This is an indication that the frequency responses of all four sensors were close

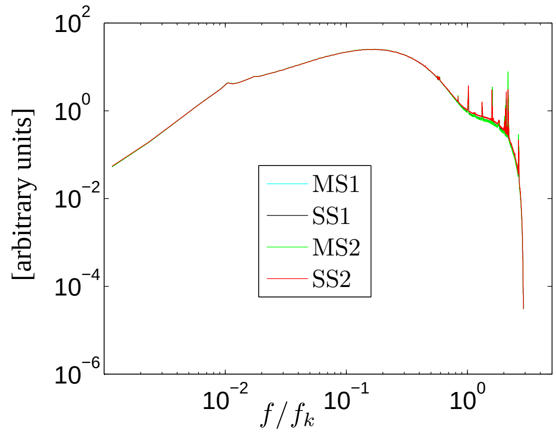

Figure 4.15: Spectra of the temperature time derivative measured by the four sensors of the four-wire probe.

to each other, so differences between the time constants of the four sensors may be neglected. Moreover, all signals were digitally filtered at the Kolmogorov frequency, which was comparable to the estimated cut-off frequency of the sensors, so that any differences in sensor time constants would have negligible effects on the measurements (Tavoularis & Corrsin, 1981*b*). For example, the Kolmogorov frequency at the location of measurements was about 4.8 kHz, which was slightly lower than the estimated cut-off frequency of the cold-wire sensors in our study, which was typically 5 kHz for a new 0.63 μm 90%Pt/10%Rh sensor in a stream with a velocity of 7.5 m/s.

Mydlarski & Warhaft (1998) showed that the dominant source of error for the temporal derivative of temperature fluctuations was the spatial resolution, and not end conduction effects. Our findings are in agreement with this observation, as Table 4.2 shows that ratios of the second, fourth and sixth moments of the temporal derivative measured by the longer sensor and one of the shorter sensors decreased with moment order. To keep errors at the lowest possible level, only temperature derivative statistics measured by SS and MS will be reported in the following chapters.

Estimates of the temperature dissipation rate measurement error due to the length of the cold-wire sensors can be obtained from the theoretical analysis of Wyngaard (1971). Considering that a typical value of η_θ for the present temperature fields was about 0.3 mm, one may calculate the typical values l_w/η_θ = 1.3, 1.5 and 2 for the SS, MS, and LS, respectively, from which one may estimate that the LS would resolve up to 90% of the scalar dissipation rate and the sensors of the four-wire probe (MS and SS) would be able to resolve up to approximately 95% of the scalar dissipation rate. The reported results will be corrected for this error.

To keep errors in measurements of the spatial temperature derivatives as low as possible, all sensors of the four-wire probe were inspected under a microscope for straightness and parallel positioning prior to the experiments. To evaluate the effect of electronic noise, velocity sensitivity of cold-wire sensors and other undesirable influences on the measurements of spatial velocity derivatives, we compared measurements of these derivatives in the unheated and heated flows. The mean square value in the unheated flow was subtracted from that in the heated flow to provide a noise-corrected value, under the assumption that "noise" and temperature fluctuations were uncorrelated. Some typical examples of the magnitude of these corrections are as follows. The values of rms temperature derivatives $\sqrt{\overline{(\partial\theta/\partial x_i)^2}}$ were typically 3.5 K/m in unheated flows or unheated regions of the three scalar fields. The ratios of the rms temperature derivatives at the centre of the TML to corresponding values in the unheated flow were about 43, so the noise-correction in this case was less than 0.1% and could be neglected. The same ratios were approximately 6 at a position in the TML where the temperature rise was about 0.1 K; in this case, the corrected mean square temperature derivatives were 3% lower than the uncorrected values.

The effect of wire spacing Δx on the accuracy of temperature derivatives measured by parallel sensors has been studied by several investigators. Antonia & Mi (1993) showed that this effect on $\overline{(\partial\theta/\partial x_i)^2}$ would be negligible for $\Delta x/\eta < 3$. Tong & Warhaft (1994) also showed that for $1 < \Delta x/\eta < 3$ the shapes of the PDF of derivatives and their their skewnesses and kurtoses were insensitive to Δx, but for $\Delta x/\eta \geq 3$ the skewness and kurtosis tended to diminish with increasing Δx. The values of $\Delta x/\eta$ for our four-wire probe were 2.4 and 2.6. To test the consistency between temperature derivatives measured by the two pairs, we compared measurements at the centre of the TML taken with the probe in one orientation and those taken with the same probe rolled by 90° about its streamwise axis. Figure 4.16 shows that the PDF of scalar derivatives

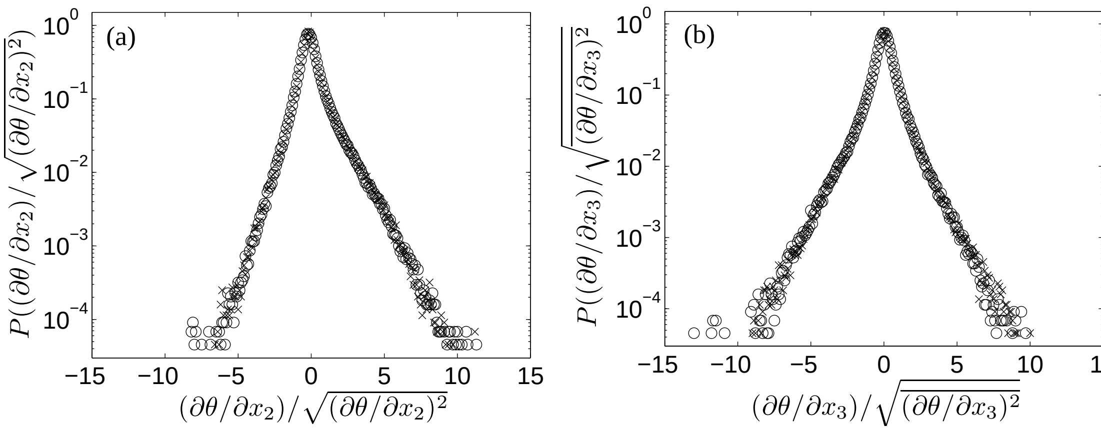

Figure 4.16: PDF of $\partial\theta/\partial x_i$ normalized by its standard deviation for the two different spacing between the parallel wires of the 4-wire probe (a) transverse direction, and (b) the spanwise direction; ×: $\Delta/\eta = 2.4$ and ∘: $\Delta/\eta = 2.6$.

Table 4.3: Ratios of temperature derivative variances measured by the two pairs of cold-wire sensors.

$\overline{(\partial\theta/\partial x_2)^2}_{90}/\overline{(\partial\theta/\partial x_2)^2}$	$\overline{(\partial\theta/\partial x_3)^2}_{90}/\overline{(\partial\theta/\partial x_3)^2}$
0.98	1.02

$\partial\theta/\partial x_i$ measured by the two wire pairs essentially coincided. Table 4.3 shows that the temperature derivative variances measured by the two pairs of sensors were within 2% from each other; such precision is well within the measurement uncertainty of the sensor spacing, determined with the use of the microscope. During the same tests, the correlations between the temperature and its first derivatives in the transverse and spanwise directions were also found to be the same for the two pairs. These results demonstrate that there was no significant qualitative difference between the assumed and the actual probe geometries and that the ratio of spacings of the two wire pairs was represented accurately by the used value of 1.1.

Chapter 5

Results

This chapter consists of two manuscripts intended to be submitted for publication in journals. In the first manuscript, the effects of scalar field inhomogeneity on the probability density functions and velocity conditional expectations are investigated using three different scalar fields superimposed on a uniformly sheared flow. The scalar fields cover wide range conditions to set a ground for a conclusive comparison. The effects of scalar discrepancies are isolated by using the same turbulent flow in the three scalar fields. In the second manuscript, the fine structure of the scalar fields as well as the conditional expectations of the scalar dissipation rate are presented and discussed.

5.1 Passive scalar transport and mixing in uniformly sheared turbulence

This section contains a draft for a manuscript, entitled "Measurements of scalar probability density functions and velocity conditional expectations in uniformly sheared turbulence", which is intended to be submitted for publication in the Journal of Fluid Mechanics.

Under consideration for publication in J. Fluid Mech. 1

Measurements of scalar probability density functions and velocity conditional expectations in uniformly sheared turbulence

A. Behnamian, S. Tavoularis †

Department of Mechanical Engineering, University of Ottawa, Ottawa, Ontario, Canada

(Received —)

The statistical properties of the velocity and scalar fields were measured simultaneously in nearly-homogeneous, uniformly sheared turbulence with three passively superimposed temperature fields, namely a transversely homogeneous temperature field with a uniform mean temperature gradient (UTG), a thermal mixing layer (TML) and the plume of a heated line source (PLS). In the UTG, the temperature probability density function (PDF) was Gaussian and the conditional velocity expectations were linear functions of the temperature value, whereas in the TML and the PLS the temperature PDF were sub-Gaussian and the conditional velocity expectations were non-linear. The results are interpreted in the light of the effects of scalar inhomogeneity, bounding values and initial conditions.

Key Words: Turbulence, Homogeneous Turbulence, Uniformly Sheared Flow, Homogeneous Shear Flow, Turbulent Mixing, Mixing and Dispersion

---

1. Introduction

The formulation of statistical balance equations for the turbulent velocity and transported scalars (*e.g.*, the concentration of an admixture and temperature) in terms of their probability density functions (PDF) and joint probability density function (JPDF) is an alternative to the more common approach, which is in terms of statistical moments. Although both approaches lead to open hierarchies of equations, the PDF approach has an advantage in reactive flows, because it can treat arbitrary chemical reactions exactly,

† Email address for correspondence: stavros.tavoularis@uottawa.ca

whereas the moment approach requires the use of models. In the velocity and scalar JPDF transport equation, terms that represent convection, reaction and body force are in closed form and the mean pressure force can also be converted to a closed form; nevertheless, terms that represent molecular processes and fluctuating pressure forces contain conditional expectations, which have to be modelled. Models of these terms have usually been tested in homogeneous turbulence with superimposed canonical scalar fields, in which velocity and scalar fluctuations may, under certain conditions, have a jointly normal JPDF, in conformity with some experimental evidence. An alternative approach to the solution of the velocity-scalar JPDF equation is the solution of the turbulent velocity equations by some approximate means, together with a solution of the scalar PDF equation (Pope 1985). Like the JPDF equation, the scalar PDF equation contains conditional expectations, which need to be modelled. However, instead of a conditional fluctuating pressure gradient term, the scalar PDF includes a turbulent transport term, which contains the conditional velocity expectation $\overline{u_i|\theta = \Theta}$, where u_i is the velocity fluctuation, θ is the scalar fluctuation and Θ is the sample-space variable for the scalar values (Pope 2000). A common modelling assumption is to assume that $\overline{u_i|\theta = \Theta}$ is a linear function of Θ, which would be true if the velocity-scalar JPDF were jointly normal. Despite some known disadvantages of the scalar PDF equation by comparison to the JPDF equation (Pope 1985), the former provides a suitable theoretical foundation for examining the statistical properties of a scalar field in turbulent flows. In particular, it allows one to focus on the statistical differences between different scalar fields embedded in the same turbulence, which is the topic of concern in the present investigation.

The shapes of the scalar PDF and the velocity-scalar conditional expectations in turbulent flows under different conditions have been subjects of many theoretical, experimental and computational investigations. Most fundamental studies have considered passive scalar fields, so that the turbulence would be decoupled from scalar variations. To further reduce the complexity of this problem, much research has focussed on statistically simple velocity and scalar fields, particularly on configurations in which the velocity fluctuations, and in some cases also the scalar fluctuations, would be approximately homogeneous. Nearly homogeneous turbulent fields that have been generated successfully in wind- and water-tunnels include grid-generated, nearly isotropic turbulence (GT), and uniformly sheared flow (USF), which has a strongly anisotropic turbulence structure. Nearly homogeneous temperature fields have also been superimposed passively on the turbulence by the injection of a small amount of heat from electrically heated elements inserted in the flow; these include cases in which the mean temperature was uniform on transverse planes and the temperature fluctuations decreased downstream, and cases with a linear transverse profile (*i.e.*, having a uniform mean temperature gradient; such flows will be referred to as UTG), which generated continuously temperature fluctuations. Similar heating methods have been used to superimpose inhomogeneous temperature fluctuation fields on homogeneous turbulence. Among such cases, of particular interest in the present study are thermal mixing layers (TML) between two streams with different mean temperatures and plumes generated by thin heated elements placed across the flow and acting essentially as scalar line sources (PLS). The available literature on relevant experimental studies of the scalar PDF and the velocity-scalar conditional expectations will be respectively summarized in the following two paragraphs.

The few available measurements of a scalar PDF in nearly homogeneous turbulence have been contradicting each other. In an early study of a GT with UTG (Venkataramani & Chevray 1978), the scalar PDF was found to be moderately non-Gaussian with a slight positive skewness and a flatness that was slightly lower than the Gaussian value of 3. In other experiments in GT with UTG, the scalar PDF was found to have exponential tails when a conventional grid was used (Jayesh & Warhaft 1991, 1992) and a sub-Gaussian shape when an active grid was used (Mydlarski & Warhaft 1998; Mydlarski 2003). Gylfason & Warhaft (2004) conducted scalar experiments in UTG superimposed on GT by three different grids (a “small” regular grid, a “large” regular grid and an active grid) and concluded that the integral length scale of the turbulence would need to be sufficiently small, by comparison to the tunnel width, for rare large scalar fluctuations to arrive at the measuring position from large upstream transverse separations, thus producing an exponential scalar PDF. Gylfason & Warhaft (2004) showed that this condition was not satisfied in the active grid case; in this case, the scalar PDF was found to be sub-Gaussian, as large fluctuations were clipped by the maximum and minimum temperatures at the tunnel walls. In USF with a UTG, the scalar PDF was found to be essentially Gaussian (Tavoularis & Corrsin 1981; Ferchichi & Tavoularis 2002). In a TML superimposed on GT by heating half of the grid (LaRue & Libby 1981), the scalar PDF was distinctly non-Gaussian, even at the TML centre, whereas in a TML generated by a heating screen that was far upstream or downstream of the turbulence-generating grid (Ma & Warhaft 1986), the scalar PDF was slightly sub-Gaussian in the TML centre and increasingly non-Gaussian away from it (Warhaft 2000). In a study of a TML in USF (Ferchichi & Tavoularis 1992), which did not present measurements of the scalar PDF, the temperature fluctuation skewness was found to be zero on the TML centre and to increase monotonically in magnitude on either side. One of the earliest experimental determinations of the scalar PDF was the one performed by Uberoi & Corrsin (1952) in a PLS embedded in GT; they observed that the PDF at the centre of the plume was nearly Gaussian far downstream of the source. In a conserved PLS in GT (Li & Bilger 1996), the scalar PDF skewness was found to be slightly positive near the centre of the plume and to increase in magnitude towards the edges. Similarly, in a PLS embedded in USF (Karnik & Tavoularis 1989), the scalar PDF was nearly Gaussian at the location of the mean temperature peak, but it became increasingly skewed as the distance from the peak location increased. The scalar PDF is known to be even more complex in some inhomogeneous turbulent flows. On the far-field centreline of the wake of a heated cylinder, the scalar PDF had an exponential tail towards the cold side and a Gaussian tail towards the warm side (Kailasnath *et al.* 1993). In a heated jet, the scalar PDF relatively close to the orifice was skewed, with an extended tail on the cold side and a nearly Gaussian warm side, but in the far field this PDF became approximately Gaussian (Tong & Warhaft 1995). More recently, Lavertu & Mydlarski (2005), Lepore & Mydlarski (2011) performed a series of scalar experiments by inserting a heated line source across a fully developed flow in a channel with an aspect ratio of approximately 18. In these experiments, both the velocity and the scalar fields were inhomogeneous. Lavertu & Mydlarski (2005) investigated a two-dimensional PLS by placing the line source across the width (*i.e.*, the long dimension) of the channel, whereas Lepore & Mydlarski (2011) generated a three-dimensional scalar field by placing the source across the height of the channel. The results of both studies showed that, far downstream of the line source, the scalar PDF was nearly Gaussian, both in the channel centre and close to the wall.

Measurements of velocity conditional expectations have also produced inconsistent results concerning the linearity of this property. In GT with a UTG, the velocity conditional expectations were found to be approximately linear in cases in which the scalar PDF was not strongly non-Gaussian (Venkataramani & Chevray 1978; Mydlarski 2003); unfortunately, authors that reported scalar PDF with exponential tails (Jayesh & Warhaft 1991, 1992; Gylfason & Warhaft 2004) did not provide measurements of velocity conditional expectations. Similarly, in USF with a UTG, where the velocity-temperature JPDF was

Gaussian, the velocity conditional expectations were approximately linear (Ferchichi & Tavoularis 2002). In GT with a reactive scalar mixing layer, the conditional mean transverse velocity was approximately a linear function of scalar value near the mixing layer centre, but strongly non-linear towards the edges (Li & Bilger 1994). In a heated jet, the velocity conditional expectations were nearly linear, except at locations with large negative temperature fluctuations (Tong & Warhaft 1995). In a confined rectangular water jet containing dye as a passive scalar, the conditional mean velocities were approximately linear at a location that was 30 jet diameters downstream of the jet orifice (Feng *et al.* 2007). Finally, in a confined wake, the conditional transverse velocity variation was found to be approximately linear, but the variation of the conditional streamwise velocity was non-linear (Feng *et al.* 2008).

As indicated by the previous discussion, available experimental evidence has been insufficient to clarify conclusively the shapes of the scalar PDF and the velocity conditional expectations and their dependence upon the turbulence and scalar field properties. As a strategy towards enhancing our insight on these issues, it seems appropriate to consider a series of different scalar fields in the same turbulent flow; by increasing the complexity of the scalar field, one would be able to elucidate the effects of the scalar initial condition and mean scalar variation, while keeping the transporting mechanism characteristics fixed. To avoid further complications, it seems advisable to examine, at least in the initial phase, nearly homogeneous turbulence.

The objective of the present research is to further investigate experimentally the shapes of the scalar PDF and the conditional expectations of the velocity components in USF with three different passively superimposed scalar fields. USF is a very appropriate environment for studying the fundamentals of turbulent mixing, as it is free of complications arising from turbulence inhomogeneity, the proximity of walls and external intermittency; moreover, like most practical flows and unlike GT, USF is subjected to turbulence production, which induces strong turbulence anisotropy. Our choices of scalar fields were made as to allow us to examine separately and in combination the effects of scalar inhomogeneity and those of initial conditions, namely the extent by which local scalar fluctuations could be traced back to the apparatus that generated each scalar field. The following three cases were considered: a) UTG, in which the scalar field was both homogeneous and free of initial effects; b) a TML, in which the scalar field was inhomogeneous but also free of initial effects; and c) a PLS, in which the scalar field was both inhomogeneous and subjected to initial effects. In addition to measurements reported in this article, we have also conducted high resolution measurements of the scalar fine structure and conditional expectations of the scalar dissipation rate in the same flow and for the same scalar fields, but we will present these results in a separate article. We hope that our results will advance our understanding and modelling capability of passive scalar transport and mixing in turbulent shear flows and help resolve some of the controversies that have appeared in the literature concerning the scalar PDF equation.

2. Apparatus and experimental procedure

All experiments were conducted in an open loop wind tunnel which has been described in detail by Karnik & Tavoularis (1987). The test section had a height $h = 305$ mm, a width equal to $1.5h$ and a length equal to $16.6h$ (see figure 1). Uniform mean shear was generated by a *shear generator*, comprising an array of 12 parallel channels, each containing a number of screens with different solidities, followed by a *flow separator*, comprising additional unobstructed lengths of the same parallel channels, which straightened the stream and imposed uniformity of the initial length scales; the height of each channel, including the half-thickness of the separating plates on either of its sides, was $M = 25.4$ mm. Passive heating of the flow was provided by a screen consisting of 49 pairs of electrically heated ribbons (0.1 mm$\times$0.8 mm) of Nichrome alloy spaced by 6.1 mm in the transverse direction. Each pair was arranged such that the downstream ribbon was in the wake of the upstream one; this arrangement was designed as to allow the injection of as much heat as possible into the flow without introducing significant flow disturbance. As discussed by Karnik & Tavoularis (1989), the thickness of ribbons was small enough for the possibility of vortex shedding from these ribbons to be ruled out. Each desired initial mean temperature profile was generated by adjusting manually the electric current through each pair of ribbons. The UTG was generated by gradually increasing the current through each pair of ribbons from the bottom to the top of the wind tunnel cross-section. The TML was generated by heating electrically the ribbons in the upper half of the screen, while compensating for the fact that the mean velocity increased upwards. The PLS was generated by heating a single pair of ribbons that was located near the wind tunnel centreline. A considerable length of the upper wall of the test section was covered by a foil made of copper, which was heated electrically to a temperature that

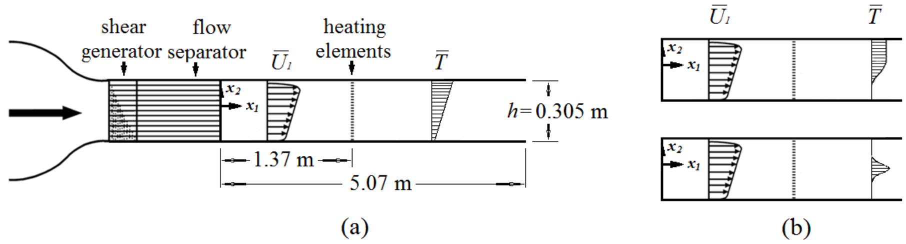

Figure 1: Schematic diagram of the experimental facility showing mean velocity and mean temperature profiles: (a) USF with UTG and (b) USF with TML (top) and USF with PLS (bottom). The origin of the coordinate system is $0.075h$ above the centreline of the test section.

was approximately equal to the local flow temperature, thus minimizing heat losses from the warmer part of the flow.

A three-sensor probe, consisting of a hot-wire pair in a cross-wire configuration and a cold-wire, was used for simultaneous velocity and temperature measurements. The separations between neighbouring sensor planes were 0.5 mm. Platinum-plated Tungsten wires with a diameter of 2.5 μm and a length to diameter ratio of 340 were spot-welded to the cross-wire prongs and operated at a constant overheat ratio of 1.5; for all measurements, the sensor length was smaller than 2.4 times the local Kolmogorov microscale. The cold-wire sensor was made of a 90% Pt – 10% Rh alloy; it had a diameter of 0.63 μm and a length to diameter ratio of about 950, and was operated at a constant current of 0.15 mA, which was sufficiently small for the velocity contamination of the cold-wire signals to be negligible; the cold-wire length was in all cases smaller than twice the local temperature microscale $\eta_\theta \equiv (\gamma^3/\epsilon)^{1/4}$, where γ is the thermal diffusivity. The -20 dB cut-off frequency for fresh cold-wires was estimated with the use of the square-wave test to be about 5 kHz, which is consistent with values given by LaRue *et al.* (1975) and Lemay *et al.* (2003). The hot- and cold-wire signals were low pass filtered at 10.4 and 8 kHz, respectively, and sampled simultaneously at a rate of 22 kHz. The filtered signals were digitized using a 16-bit National Instrument (PCI 6143) data acquisition system. Before processing, the time series were filtered digitally using a double-pass, seventh-order, Butterworth, low-pass filter, with a cut-off frequency that was adjusted at each location to the local Kolmogorov frequency. Time series consisting of 5.5×10^5 samples were recorded for calculating time-averaged profiles, whereas longer ones, consisting of 1.1×10^8 samples, were recorded separately for calculating some PDF and conditional expectations. Each of the latter time series extended over 83 min and was divided into $5,000$ segments. Each segment was long enough to represent adequately the longest time scales of turbulent motion (namely, roughly 200 times the velocity integral timescale) and short enough not to be influenced by possible wind tunnel speed fluctuations, hot/cold-wire voltage drift and room temperature variations. Alternate segments were discarded so that the remaining $2,500$ segments were statistically independent of each other. PDF and conditional expectations were first calculated separately for each of the latter segments and then the values for all these segments were ensemble averaged to provide the reported results. In particular, the room temperature variation is accounted by commuting in blocks

The mean temperature upstream of the heating screen was monitored with the use of a platinum RTD (29348-T01-B-48, RDF Crop.), precision-calibrated by the manufacturer and embedded in a micro-capsule made of stainless steel with 1.67 mm diameter. The upstream flow temperature was subtracted from all other measured temperatures to provide the reported temperature rises, which were insensitive to room temperature fluctuations. Additionally, a glass thermistor mini-probe (EPCOS B57540, 10 kΩ 1% RAD), with 0.8 mm diameter and a time constant that was lower than 1 s, was mounted on the traversing system at the same level as the three-wire probe and was used to measure the local mean temperature at each measurement location. The circuitries of the RTD and the thermistor provided low enough excitation currents so that the self-heating of the mean temperature probes was essentially negligible during the measurements. The hot-wire signals were corrected for variations of the mean temperature, measured by the local thermistor, and for instantaneous temperature fluctuations, measured with the cold wire, with the use of a modified King's law (Tavoularis 1983, 2005). The cross-wire was calibrated in a calibration jet using the effective angle method (Browne *et al.* 1989). The cold-wire voltage was calibrated in-situ in the heated flow against the mean temperature measured by the thermistor probe.

3. Mean characteristics of the turbulence and the scalar fields

3.1. *The velocity field*

The characteristics of the USF in the absence of the heating screen have been documented in earlier reports in the same facility by Karnik & Tavoularis (1987), Tavoularis & Karnik

(1989), and Ferchichi & Tavoularis (2000). The insertion of the heating screens resulted in a slight reduction of the mean shear and production of some additional small-scale turbulence, which was expected to decay before the measuring section. The heating screen was inserted at a position with $x_1/h = 4.5$, where the dimensionless turbulence development time (or total mean strain of the flow) was

$$\tau = \int_0^{x_1} \frac{1}{\overline{U}_{1c}} \frac{d\overline{U}_1}{dx_2} dx_1 \approx 5.8. \tag{3.1}$$

Figure 2a shows representative mean profiles of the streamwise velocity at four positions downstream of the heater, with the heater in place but without heating. These profiles were fitted well by lines; the standard deviation of the difference between the measurements and the corresponding linear fit decreased downstream to about 1.8% at $x_1/h = 10$. The centreline mean velocity varied by less than 1% in the range $7 \leqslant x_1/h \leqslant 10$. Figure 2b shows representative transverse profiles of the time-averaged streamwise and transverse turbulent intensities and the shear stress correlation coefficient in the unheated and heated flows. This figure demonstrates that the effects of heating were very small; the small differences in the profiles of the stresses may be attributed to minor changes of the performance of the shear generator between measurements in the different flows, particularly in its lower half which contained several fine screens and/or fibreglass sheets. In agreement with previous studies (Tavoularis 1985; Vanderwel & Tavoularis 2011), which showed that for $5 < \tau$ in USF the turbulence would be fully developed, we also found that all stresses downstream of the screen increased at approximately exponential rates. The evolution of the turbulent kinetic energy, $k = \frac{1}{2}\overline{u_i u_i}$, illustrated in figure 2c, could be fitted by the exponential expression

$$k = k_0 \; e^{a\tau} \; , \tag{3.2}$$

where $a \simeq 0.11$ and $k_0 = 4.5 \times 10^{-2}$ m^{2}s^{-2}. The value of growth exponent was close to those in previous experiments in USF generated in wind (Karnik & Tavoularis 1989) and water tunnels (Vanderwel & Tavoularis 2011). As shown in figure 2d, the Reynolds stress anisotropies, defined as

$$m_{ij} = \frac{\overline{u_i u_j}}{2k} - \frac{1}{3}\delta_{ij} \tag{3.3}$$

were essentially constant along the x_1 axis in the range of interest.

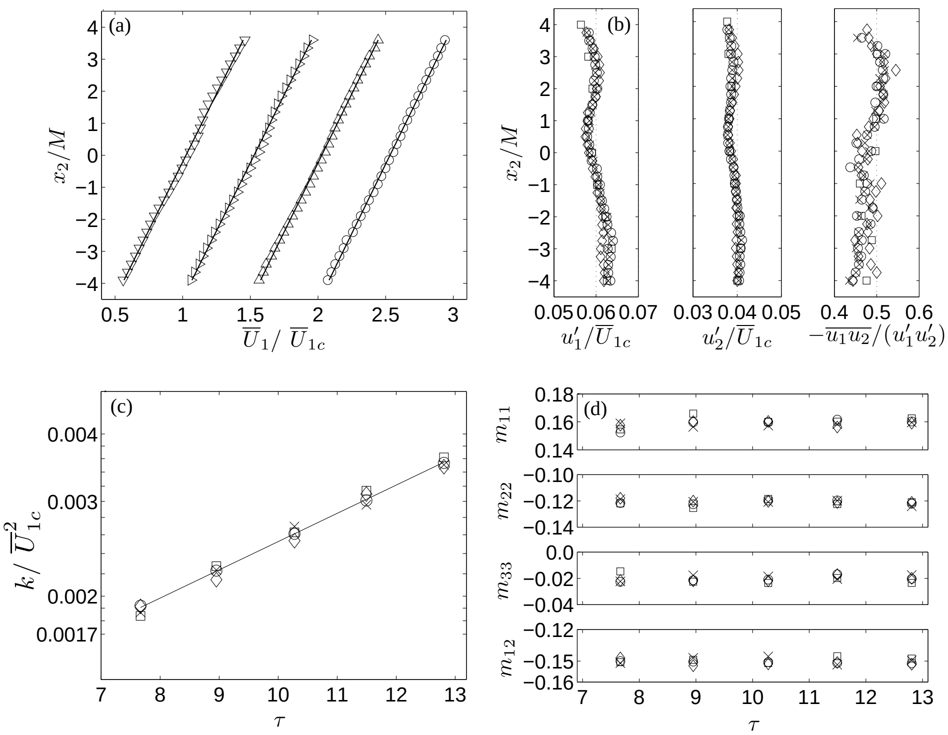

Figure 2: (a) Transverse profiles of the dimensionless mean velocity in the unheated flow with the heating screen in place; ▽: $x_1/h = 7$; ▷: $x_1/h = 8$; △: $x_1/h = 9$; ○: $x_1/h = 10$; solid lines represent linear least square fitting; for clarity, each of the three most downstream plots has been shifted to the right from the previous plot by half unit. (b) Transverse profiles of the streamwise and transverse turbulent intensities and the shear stress correlation coefficient at x_1/h=10. (c) Streamwise evolution of the turbulent kinetic energy; solid line indicates fitted exponential expression. (d) Streamwise evolution of the Reynolds stress anisotropies. Symbols for (b)–(d) are as follows. ○: unheated flow; □: UTG, ◇: TML, ×: PLS.

$\overline{U}_1$	$\frac{h}{\overline{U}_1}\frac{d\overline{U}_1}{dx_2}$	k	m_{11}	m_{22}	m_{33}	m_{12}	$L_{11,1}$	λ_{11}	η	ϵ	Re_λ
ms^{-1}	-	$\mathrm{m^2s^{-2}}$	-	-	-	-	mm	mm	mm	$\mathrm{m^2s^{-3}}$	-
7.48	1.28	0.19	0.16	-0.12	-0.02	-0.15	41	6.8	0.25	0.93	195

Table 1: Characteristic properties of the velocity field at $x_1/h = 10$, $x_2/M = 0$.

The streamwise velocity integral timescale T_{11} was measured by integrating the corresponding autocorrelation function in each time series segment to its first zero and then ensemble averaging the values in all 2.5×10^3 segments. The streamwise integral length scale was determined with the use of Taylor's frozen flow approximation as $L_{11,1} = \overline{U}_1 T_{11}$.

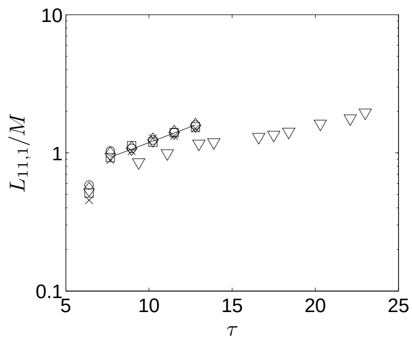

Figure 3: Downstream evolution of the streamwise integral lengthscale; □: UTG, ⋄: TML, ×: PLS; ▽: measurements by Ferchichi & Tavoularis (2002); solid line represents a segment of 3.4.

Figure 3 shows the streamwise integral lengthscale growth. Within a limited range, the results could be fitted by the exponential expression

$$\frac{L_{11,1}}{M} = 0.39\ e^{0.11\tau}. \tag{3.4}$$

The presently measured values of $L_{11,1}$ were somewhat larger than values reported by Ferchichi & Tavoularis (2002); the difference is attributed to differences in length scale reduction of the oncoming flow by the screens, which were different in the two studies. The integral lengthscale that is most relevant to scalar transport is the transverse scale $L_{22,2}$. This scale was too difficult to measure in the present facility, but it may be estimated from the ratio $L_{22,2}/L_{11,1} \simeq 0.56$, which was measured with the use of particle image velocimetry in fully developed USF in a water tunnel (Vanderwel & Tavoularis 2014); thus, we will consider that, at $x_1/h = 10$ in the present flow, $L_{22,2} \simeq 23$ mm.

The streamwise Taylor microscale was measured as

$$\lambda_{11} = \overline{U}_1 \left[\frac{\overline{u_1^2}}{\overline{(\partial u_1/\partial t)^2}} \right]^{1/2} . \tag{3.5}$$

The turbulent kinetic energy dissipation rate ϵ was estimated from the mean turbulent kinetic energy equation (simplified for USF), as the difference between turbulent kinetic energy production by the mean shear and convection by the mean flow. Then the Kolmogorov microscale was calculated as $\eta = (\nu^3/\epsilon)^{1/4}$.

Representative values of the main time-averaged properties of the velocity field are presented in table 1. The turbulence Reynolds number $Re_\lambda = u_1'\lambda_{11}/\nu$ was 195, which is large enough for the flow to be considered fully turbulent. Measured energy spectra

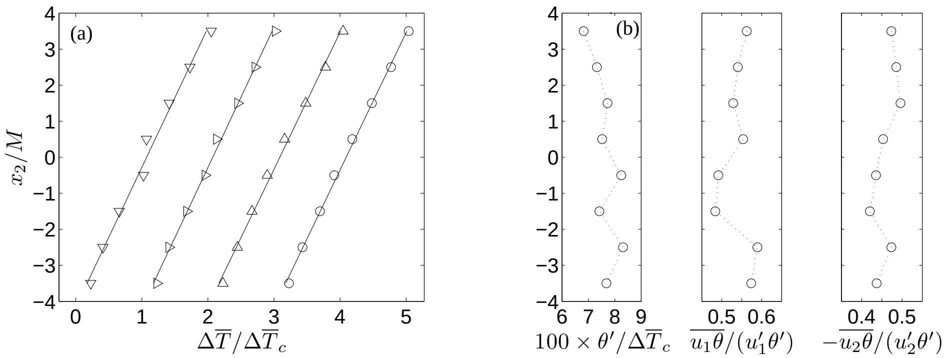

Figure 4: Representative temperature measurements in the UTG field. (a) Transverse profiles of the mean temperature; ▽: $x_1/h = 7$; ▷: $x_1/h = 8$; △: $x_1/h = 9$; ○: $x_1/h = 10$; solid lines represent a linear least square fitting; for clarity, each of the three most downstream plots has been shifted to the right from the previous plot by a half unit. (b) Transverse profiles of the normalised standard deviation of the temperature fluctuations and the turbulent heat flux coefficients at $x_1/h = 10$.

were generally in agreement with previous results in USF experiments at comparable turbulent Reynolds numbers (Ferchichi & Tavoularis 2000; Garg & Warhaft 1998). The one-dimensional power spectrum of the streamwise velocity fluctuations had an inertial subrange for streamwise wavenumbers κ_1 in the range $4 \times 10^{-3} \lesssim \kappa_1\eta \lesssim 10^{-1}$; within this range, the spectrum, when plotted in logarithmic axes, decreased with a slope of -1.57, which is only slightly smaller than the Kolmogorov value of $-5/3$.

3.2. *The homogeneous temperature field*

Representative values of some important time averaged properties of the three scalar fields are listed in table 2. Figure 4 shows transverse profiles of the mean temperature rise $\Delta\overline{T}$, normalized by $\Delta\overline{T}_c = 0.70$ K, the normalised temperature standard deviation and the streamwise and transverse turbulent heat flux coefficients for the UTG case. The non-linearity of the mean temperature profiles was very small and non-uniformities of the three latter properties had standard deviations that were lower than 6%. In summary, the inhomogeneity of the present UTG field was significantly lower than those in previous studies in the same facility and elsewhere. The temperature variance grew at the same rate as the turbulent kinetic energy and could be represented well by the exponential expression $\overline{\theta^2}/\Delta\overline{T}_c^2 = (1.6 \times 10^{-3})e^{0.11\tau}$, in conformity with previous UTG experiments in USF.

	$\Delta\overline{T}$ K	$d\overline{T}/dx_2$ Km^{-1}	$\theta'/\Delta\overline{T}$ -	$\overline{u_1\theta}/u_1'\theta'$ -	-$\overline{u_2\theta}/u_2'\theta'$ -	$L_{\theta 1}/L_{11,1}$ -	$\lambda_{\theta 1}/\lambda_{11}$ -
UTG ($x_2 = 0$)	0.70	7.9	0.080	0.52	0.45	0.54	0.65
TML (at A)	1.00	28.0	0.34	0.49	0.42	0.55	0.60
PLS (at C$'$)	0.45	12.7	0.23	0.41	0.38	0.51	0.60

Table 2: Characteristic properties of the temperature fields at $x_1/h = 10$

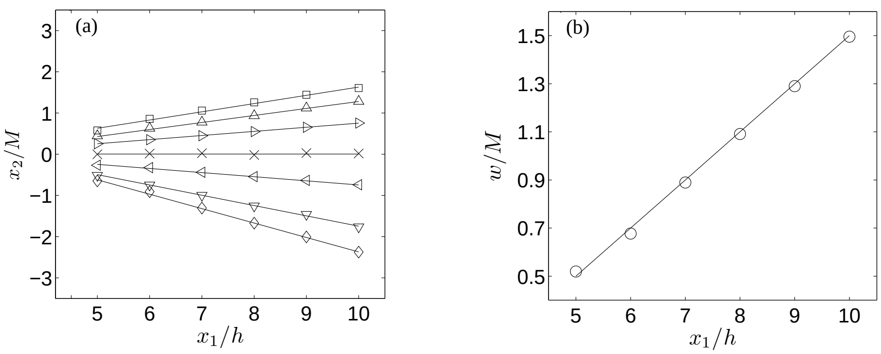

Figure 5: (a) Typical isotherms on the TML vertical centreplane; $\Delta\overline{T}/\Delta\overline{T}_h$ = 0.95(□), 0.90(△), 0.75(▷), 0.50(×), 0.25(◁), 0.10(▽) and 0.05(◇). (b) Streamwise evolution of the TML width.

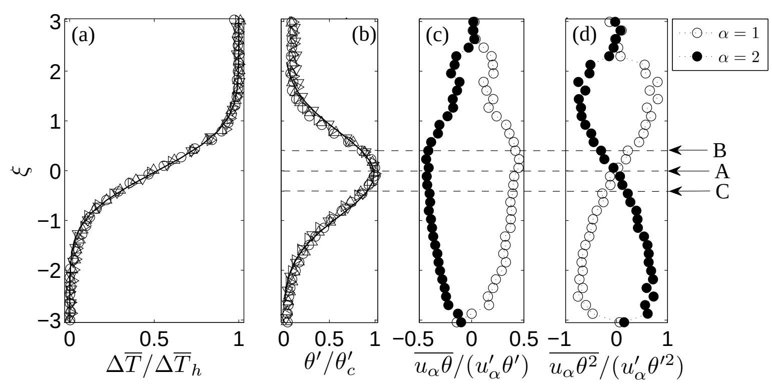

Figure 6: Transverse variations of time-averaged properties in the TML. (a) Mean temperature; ▽: $x_1/h = 7$; ▷: $x_1/h = 8$; △: $x_1/h = 9$; ○: $x_1/h = 10$; solid line represents a fitted error function. (b) Standard deviation of temperature fluctuations, normalised by its peak value; symbols as in (a); solid line represents a fitted Gaussian function. (c) Turbulent heat flux coefficients at $x_1/h = 10$. (d) Triple correlation coefficients at $x_1/h = 10$. Repeated Greek indices are not summed.

3.3. *The thermal mixing layer*

The upper half of the heating screen was heated such as to produce a thermal mixing layer between a heated stream having a nearly uniform temperature rise of $\Delta\overline{T}_h = 2.00$ K and an unheated stream. The development of this TML was consistent with the one that has been documented in detail by Ferchichi & Tavoularis (1992). As shown in figure 5a, the mean isotherms evolved linearly in the streamwise direction, such that the 50% isotherm remained parallel to the test section axis but the TML penetrated deeper into the low-velocity side than the high-velocity side. The TML width, defined as the distance between the 75% and 25% isotherms, grew linearly as $w/M = 0.20(x_1/h) - 0.49$ for $5 \leqslant x_1/h \leqslant 10$ (figure 5b). When plotted *vs.* the dimensionless transverse coordinate $\xi = (x_2 - x_{20})/w$, the mean temperature evolved in a self-similar manner (figure 6a) and could be fitted well by the error function $\Delta\overline{T}/\Delta\overline{T}_h = 0.5[1 + erf(\xi)]$ (Ferchichi & Tavoularis 1992). The position of the 50% isotherm was $x_{20} \approx 0$ for $5 \leqslant x_1/h \leqslant 10$. The temperature fluctuations also evolved in a self-similar manner. Their transverse profiles could be fitted well by a Gaussian function, except at the warm edge, where some small (less than 8% of the peak value θ'_c at $x_1/h = 10$) residual temperature fluctuations, introduced by the heated screen, persisted downstream (figure 6b). The peak temperature fluctuations decreased linearly with distance from the screen as $\theta'/\Delta\overline{T}_h = -2.8 \times 10^{-3}(x_1/h) + 0.198$ for $7 \leqslant x_1/h \leqslant 10$. The location of the peak temperature fluctuations essentially coincided with the inflection point of the local mean temperature profile, where the mean temperature gradient was maximum. The streamwise and transverse heat flux coefficients peaked at the TML centre (figure 6c), whereas the triple correlation coefficients crossed zero at that location (figure 6d). For convenience in the discussion, we have identified three special locations across the TML (figure 6d): point A, which is the TML inflection point or TML centre, and points B and C, which are on either side of the centre at distances of about $0.7L_{22,2}$ from it; points B and C were defined for comparisons with the PLS (see next subsection).

3.4. *The plume of a line source*

A single pair of ribbons (at $x_2 = 0$) was heated to generate a thermal plume, as described in section 2. The present PLS was consistent with the one reported by Karnik & Tavoularis (1989). The mean isotherms evolved linearly in the streamwise direction (figure 7a). The locus of the peak mean temperature $\Delta\overline{T}_m$ was shifted towards the low–

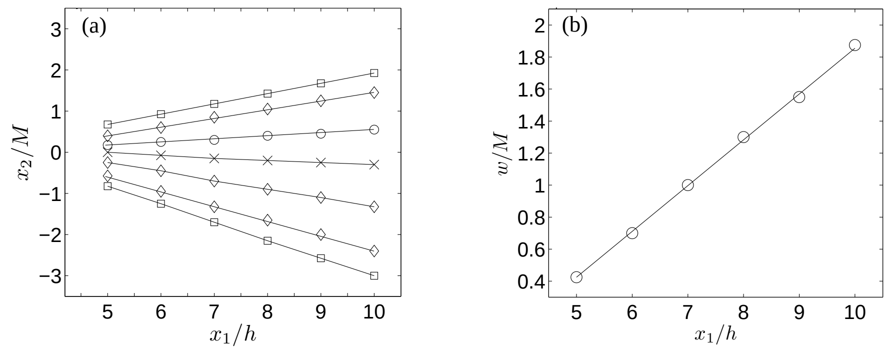

Figure 7: (a) Typical isotherms on the PLS vertical centreplane; $\Delta\overline{T}/\Delta\overline{T}_m$ = 1.0($\times$), 0.5($\circ$), 0.25($\diamond$) and 0.1($\square$) (b) Streamwise evolution of the PLS width.

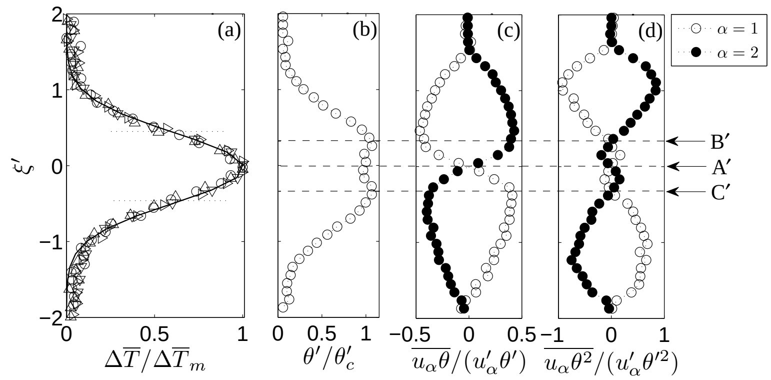

Figure 8: Time-averaged transverse profiles in the PLS. (a) mean temperature rise; symbols as in figure 6; the solid line represents a fitted Gaussian function, with its inflection points marked by dotted lines. (b) Standard deviation of temperature fluctuations at $x_1/h = 10$. (c) Turbulent heat flux coefficients at $x_1/h = 10$. (d) Triple correlation coefficients at $x_1/h = 10$.

velocity side and the heated fluid penetrated deeper into the low-velocity side than the high-velocity side; this is attributed to the fact that, at each downstream measuring plane, the diffusion time $x_1/\overline{U}_1$ decreased upwards, so that the scalar had more time to spread in the low velocity region. The PLS width w, defined as the distance between points at which the temperature rise was 50% of the local peak value, grew linearly as $w/M = 0.29(x_1/h) - 1.02$ for $5 \leqslant x_1/h \leqslant 10$ (figure 7b).

Transverse profiles of the mean temperature rise, the standard deviation of the temperature fluctuations, the turbulent heat flux coefficients and triple velocity-temperature correlation coefficients have been plotted in figure 8 vs. the dimensionless transverse coordinate $\xi = (x_2 - x_{20})/w$, where the position of the mean peak x_{20} evolved streamwise

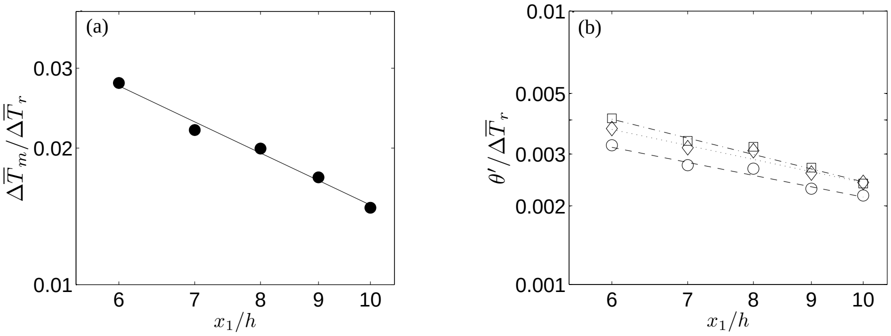

Figure 9: a) Streamwise development of the normalized peak mean temperature rise in the PLS (●); solid line is a fitted power law. b) Streamwise development of the normalized standard deviation of the temperature fluctuations in the PLS; $\theta'_c/\Delta\overline{T}_r(\circ)$, $\theta'_{ph}/\Delta\overline{T}_r(\Box)$, $\theta'_{pl}/\Delta\overline{T}_r(\diamond)$; lines represent fitted power laws.

following the relationship $x_{20}/M = 5.8 \times 10^{-2}(x_1/h) - 0.28$ for $5 \leqslant x_1/h \leqslant 10$. The mean temperature rise profiles appeared to be nearly Gaussian with the exception of the edge regions. The decay of the peak mean temperature is shown in figure 9a. The values were scaled with the reference temperature rise $\Delta\overline{T}_r = P/(\rho c_p \delta h \overline{U}_{1c}) = 40.6$ K, where P is the power per unit length supplied to the pair of heated ribbons that produced the plume, ρ is the air density, c_p is the specific heat of air under constant pressure (both properties were evaluated at ambient temperature) and δh is the ribbon thickness (Karnik & Tavoularis 1989). For $6 \leqslant x_1/h \leqslant 10$, the decay of the peak mean temperature rise could be approximated by the power law $\Delta\overline{T}_m/\Delta\overline{T}_r = 0.191(x_1/h)^{-1.11}$. Three special locations have been marked across the PLS. Point A$'$ is the location of the mean temperature peak and points B$'$ and C$'$ are the locations of the two inflection points of the mean temperature profile. It is noted that the distance between point A$'$ and either of the two other points was approximately $0.7L_{22,2}$; this was the reason for choosing points B and C in the TML, as described earlier.

The temperature fluctuation profile in the range $4.5 < x_1/h < 5$ was single–peaked, but further downstream it became double–peaked. The standard deviations of the temperature fluctuations at the PLS centre θ'_c and at the two peaks θ'_{ph} and θ'_{pl}, could, respectively, be fitted by the power laws $\theta'_c/\Delta\overline{T}_r = 1.48 \times 10^{-2}(x_1/h)^{-0.82}$, $\theta'_{ph}/\Delta\overline{T}_r = 2.74 \times 10^{-2}(x_1/h)^{-1.03}$ and $\theta'_{pl}/\Delta\overline{T}_r = 1.92 \times 10^{-2}(x_1/h)^{-0.88}$, in the range $7 \leqslant x_1/h \leqslant 10$ (figure 9b) The decrease of the peak on the high–velocity side was somewhat faster than that on the low–velocity side so that, although closer to the source $\theta'_{ph} > \theta'_{pl}$, at

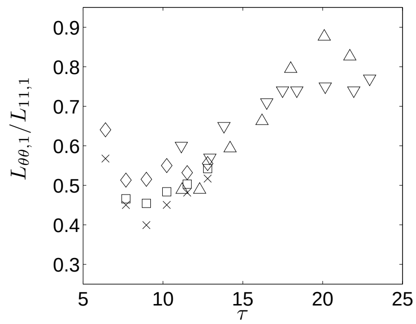

Figure 10: Ratio of integral length scales, symbols as figure 3.

$x_1/h = 10$ the peaks had approximately the same values. The complexity of the evolution of the θ' profile indicates that this property was not self–similar, in spite of the near self-similarity of the mean profiles.

Both turbulent heat flux coefficient profiles in the PLS had zeros at point A$'$ and extrema at points B$'$ and C$'$. In contrast, the triple correlation coefficients had zeros at approximately all these three points and local extrema in–between. The variations of the heat fluxes and the triple correlations in the PLS were very different from those in the TML; this observation indicates that the scalar fluctuation fields in the TML and the PLS had distinct features in spite of some similarities in the mean profiles.

3.5. *On the passivity of the temperature fields*

The passivity of the scalar field was investigated by comparing velocity statistics and spectra in the unheated and the three heated flows. The standard deviation of the transverse velocity in the heated flows was always within 3% of the value in the unheated flow. In addition, the term $g(\overline{u_2\theta})/\overline{T}$ (g is the gravitational acceleration), which represents production by buoyancy in the turbulent kinetic energy equation, was less than 0.3% of the dissipation rate in all cases considered. The flux Richardson number $R_f \equiv \frac{g(\overline{\theta u_2})/\overline{T}}{\overline{u_1 u_2}\ \partial \overline{U}_1/\partial x_2}$ (Tavoularis & Corrsin 1981), which represents the ratio of the buoyancy term and the production term, was of the order of 0.001 in the present scalar fields; such values are much smaller than 0.2, which is an approximate upper limit for buoyancy effects to be considered negligible.

3.6. *The temperature integral lengthscale*

The streamwise integral lengthscale $L_{\theta\theta,1}$ of the temperature fluctuations was measured in a manner similar to the one used for measuring $L_{11,1}$. The evolutions of the ratio

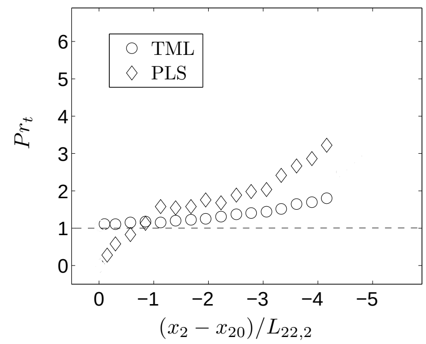

Figure 11: Turbulent Prandtl number across the non-homogeneous scalar fields at $x_1/h = 10$.

$L_{\theta\theta,1}/L_{11,1}$ for the three present scalar fields, as well as for the fields studied by Ferchichi & Tavoularis (2002) and Karnik & Tavoularis (1989) in the same facility are shown in figure 10. Despite the differences in heating methods, all data are consistent and show a downstream decrease of this ratio near the heaters ($\tau \leqslant 9$), followed by a monotonic increase towards an asymptote of about 0.8 very far downstream (not reachable in the present experiments).

3.7. *The turbulent Prandtl number*

The turbulent Prandtl number

$$Pr_t = \frac{-\overline{u_1 u_2}/(d\overline{U}_1/dx_2)}{-\overline{\theta u_2}/(d\overline{T}/dx_2)}. \tag{3.6}$$

is a customary measure of the analogy between heat and momentum transport in non-isothermal turbulent flows. Values of this parameter have been reported in many previous studies to be not too far from the ideal value of 1. In the present UTG, $Pr_t \approx 1.1$, which is consistent with the measurements of Tavoularis & Corrsin (1981) in the same type of flow. For the two inhomogeneous scalar fields, the turbulent Prandtl number was calculated from smooth fits to the corresponding profiles of mean temperature and heat flux. In view of the approximate antisymmetry or symmetry of the TML and PLS mean profiles, only the lower halves of these profiles will be considered here. The calculated transverse variations of Pr_t are shown in figure 11. Values near the edges of these flows have not been presented, as subjected to large uncertainties. Moreover, no value has been given for the centre of the PLS, where Pr_t would be indeterminate. In the TML, the value of Pr_t increases mildly from the centre towards the edge, exceeding considerably, but not excessively, the value measured in the UTG. In the PLS, Pr_t follows a similar, but much

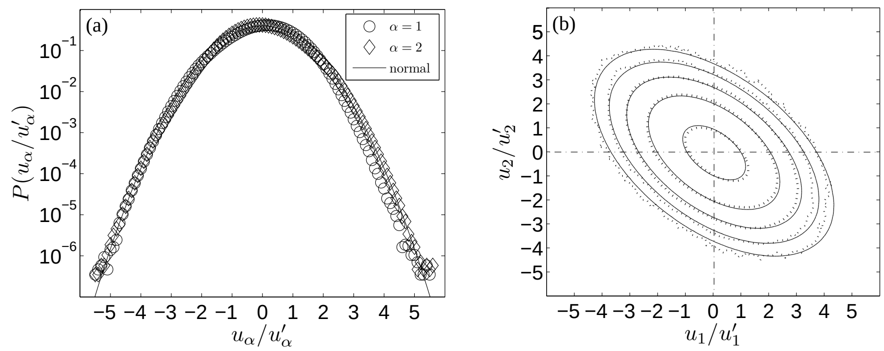

Figure 12: (a) PDF of the velocity fluctuations, (b) JPDF of the streamwise and transverse components of velocity fluctuations; dashed lines have been fitted to measured contours with values (from the outer one towards the inner one) equal to 0.00001, 0.0001, 0.001, 0.01 and 0.1; solid lines indicate the corresponding contours of a jointly Gaussian PDF with the same correlation coefficient as the measurements.

stronger, trend, exceeding the UTG value by several times near the plume's edge. It is of interest to note that in the central PLS region $Pr_t < 1$; this is consistent with the inapplicability of gradient transport in this region, where large temperature fluctuations are remnants of the initial heating. A possible cause for the large values of Pr_t in the outer regions of both the TML and the PLS is the external intermittency of the scalar fields, which effectively reduces the level of local heat flux, in contrast to the velocity field, which is not subjected to such intermittency. Apparently, this effect is stronger for the PLS, which is generated by a single heating source, than the TML, which receives heat from several sources.

In summary, the present results have demonstrated that the turbulent Prandtl number in non-isothermal homogeneous turbulence would be not constant when the scalar field is intermittent and its value may also be strongly influenced by initial effects.

4. PDF, JPDF and conditional expectations

4.1. *Velocity PDF and JPDF*

The PDF and JPDF of the streamwise and transverse velocity fluctuations are shown in figure 12. They were all nearly Gaussian, in agreement with previous USF experiments (Tavoularis & Corrsin 1981; Ferchichi & Tavoularis 2000, 2002). At $x_1/h = 10$, the skewness and flatness factors of the streamwise component were respectively -0.05 and 3.09; those of the transverse component were -0.11 and 3.11. All these values are compatible

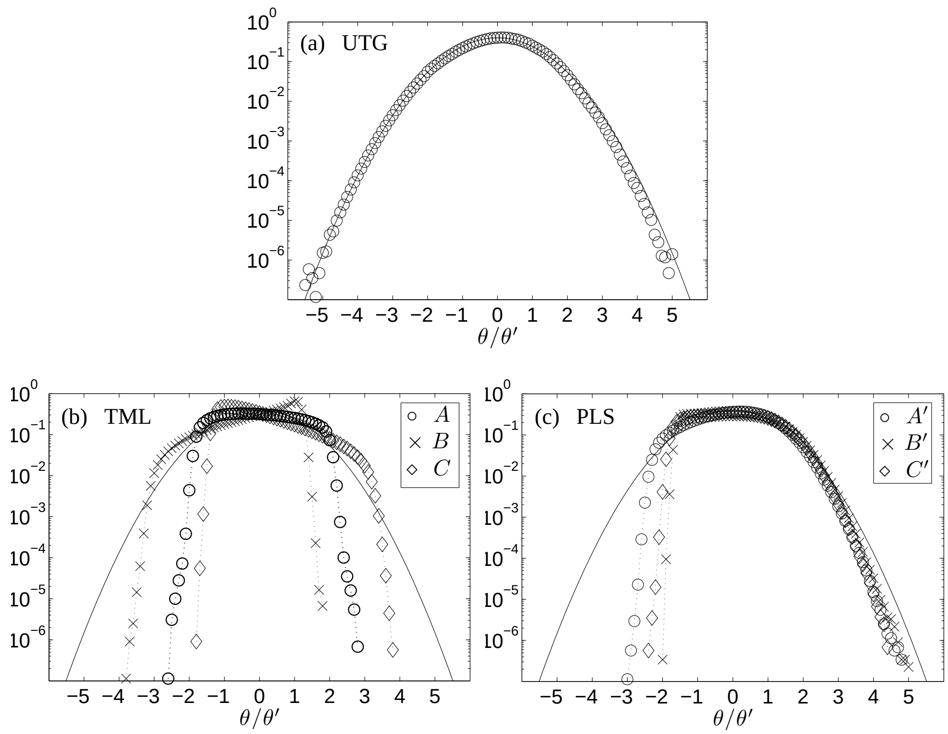

Figure 13: PDF of scalar fluctuations in the three scalar fields; solid lines represent the normal PDF.

with relatively mild deviations from Gaussianity, which may be neglected in the general context of this study.

4.2. *The scalar PDF*

PDF of the temperature fluctuations at locations of interest in the three scalar fields are presented in figure 13 and the corresponding skewness and flatness factors are listed in table 3. It is immediately apparent that the temperature PDF was essentially Gaussian in the UTG field, but distinctly non-Gaussian in the TML and the PLS. It is also interesting to note that, at some locations in the TML and the PLS, the skewness or the flatness factor happened to be not very different from the Gaussian values, despite the visibly strong non-Gaussianity of the corresponding PDF. This observation demonstrates that the use of skewness or flatness factors alone as indicators of scalar Gaussianity may lead to erroneous conclusions. Comparisons of the extreme local instantaneous temperatures (namely the highest, θ_{max}, and lowest, θ_{min}, measured temperature values) and the extreme mean temperature rises $\Delta\overline{T}_{hot}$ and $\Delta\overline{T}_{cold}$ across the wind-tunnel test section

	UTG	TML			PLS		
		A	B	C	A′	B′	C′
S	-0.19	-0.03	-0.97	0.89	-0.06	0.34	0.18
F	3.1	2.1	3.3	3.2	2.5	2.4	2.3

Table 3: Skewness and flatness factors of the scalar PDF.

are shown for all scalar fields in table 4. $\Delta\overline{T}_{cold}$ was the unheated stream temperature for all cases, whereas $\Delta\overline{T}_{hot}$ was the highest mean temperature across the UTG profile, the mean temperature of the heated stream for the TML and the peak mean temperature for the PLS profile.

UTG field: Previous literature has suggested that scalar Gaussianity in UTG fields may be the result of clipping of the scalar field by the wind tunnel walls (Warhaft 2000; Gylfason & Warhaft 2004). Unlike flows downstream of active grids, which are mixed very thoroughly, the core of the present USF was not affected by wall effects. As evidence for this assertion, consider that at the centre of the present UTG case the normalised mean temperature differences from the temperatures of the unheated (near the bottom wall) and strongest heated (near the top wall) streams were $(\Delta\overline{T}_{cold} - \Delta\overline{T})/\theta' = -14.5$, and $(\Delta\overline{T}_{hot} - \Delta\overline{T})/\theta' = 13.0$ (see table 4). As figure 13 shows, temperature values at the UTG centre were confined approximately within the range $\Delta\overline{T} \pm 5.5\theta'$, which means that no fluid from either of the two near-wall regions ever penetrated the UTG centre. The distances between the upper and lower bounds of the local temperature fluctuation range from the corresponding highest or lowest mean temperature in the wind tunnel are too large to be attributed to heat conduction from warmer to cooler air alone (the effect of heat conduction will be discussed in a following section). In support of this assertion, we also note that the transverse integral lengthscale $L_{22,2}$ was smaller than 8% of the test section height, which effectively eliminates the possibility that near-wall fluid would ever reach the wind-tunnel centreline. Additionally, all selected measurement locations in the three scalar fields were sufficiently close to the centreline to be free of wall effects.

TML field: At all three locations in the TML, the PDF shapes were strongly sub-Gaussian. At the TML centre (point A), the anti–symmetry of the mean scalar profile resulted in a nearly symmetric PDF and a near–zero skewness, but sub-Gaussianity was revealed by the low flatness. On the two sides off–centre of the TML (points B and

	UTG	TML			PLS		
		A	B	C	A′	B′	C′
$(\Delta\overline{T}_{cold} - \Delta\overline{T})/\theta'$	-14.5	-3.0	-5.0	-2.1	-6.6	-4.2	-4.4
θ_{min}/θ'	- 5.5	-2.6	-3.8	-1.8	-3.0	-2.0	-2.4
$(\Delta\overline{T}_{hot} - \Delta\overline{T})/\theta'$	13.0	3.0	2.0	5.2	0.0	1.5	1.4
θ_{max}/θ'	5.0	2.7	1.8	3.8	4.8	5.0	4.5
$(\Delta\overline{T}_{hot} - \Delta\overline{T}_{cold})/\theta'$	27.5	6.0	7.0	7.3	6.6	5.7	5.8
$(\theta_{max} - \theta_{min})/\theta'$	10.5	5.3	5.6	5.6	7.8	7.0	6.9

Table 4: Normalised mean temperature differences and extreme local temperature values at the points of interest in the three scalar fields.

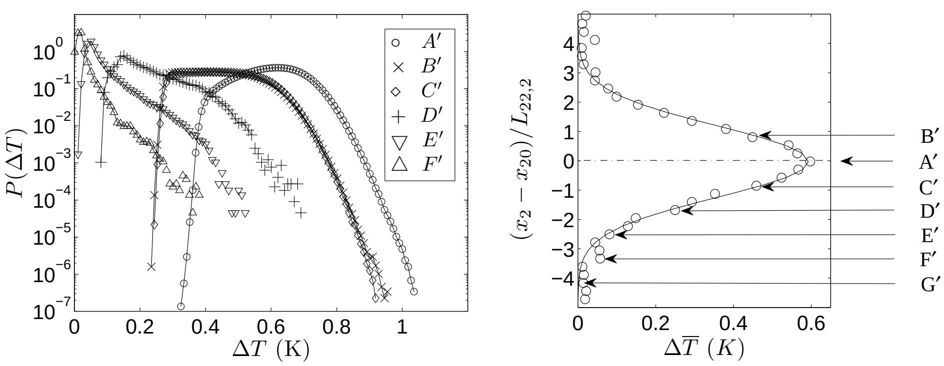

Figure 14: PDF of temperature rise in the PLS (left plot) at different locations along the mean temperature rise profile (right plot); x_1/h=10.

C), the PDF were visibly asymmetric and had relatively large skewnesses of opposite signs; perhaps surprisingly, the flatnesses were only slightly higher than the Gaussian value of 3, a fact that seems not to have much physical significance but to be specific to the distribution of large fluctuations in this field. At point A, the lowest and highest instantaneous temperature values were close but not equal to the cold and hot stream temperatures. One may possibly attribute these differences to heat conduction between an eddy that originated in one of those streams and the surrounding fluid. This issue will be further discussed in a following section. This assertion is compatible with the measurements at the other two points in the TML. At point B, which was towards the warm stream side, the highest measured temperature value was also just below the warm stream temperature, whereas the lowest temperature value was much higher (in terms of local temperature standard deviations) than the cold stream temperature. The opposite observations can be made for point C, which was towards the cold stream.

	$(x_2 - x_{20})/L_{22,2}$	$\Delta\overline{T}$ (K)	θ' (K)	S	F
A′	0.0	0.60	0.091	-0.06	2.5
B′	0.83	0.44	0.104	0.34	2.3
C′	-0.83	0.45	0.103	0.18	2.4
D′	-1.65	0.25	0.080	1.0	3.6
E′	-2.48	0.08	0.040	2.4	10.2
F′	-3.31	0.06	0.020	4.1	30.7
G′	-4.14	0.02	0.010	-	-

Table 5: Scalar field properties at the locations of the PDF shown in figure 14.

PLS field: At first glance, the PDF at all three locations in the PLS appear to be a combination of those in the UTG and the TML fields. They were sub–Gaussian on the cold side and nearly Gaussian on the warm side. The lowest measured temperatures at all three points were obviously bounded by values that were significantly higher than the unheated stream temperature. In contrast, the highest measured values at all points exceeded significantly the local peak mean temperature. Such high temperature values are necessarily remnants of the initial heating of the flow by the source. The effect of initial heating is examined in more detail in Figure 14, which shows the gradual change of the shape of the PDF of the local instantaneous temperature rise ΔT from the edge to the centre of the PLS; to assist in this task, Table 5 summarises some relevant scalar properties at the locations of PDF measurement. It is noted that the tails of the PDF at points D′, E′ and F′ show some scatter, as these PDF were based on records of $5.5{\times}10^5$ samples, which were much smaller than those used for the PDF at points A′, B′ and C′.

The effects of initial heating were clearly detectable at the plume centre (point A′) and the nearby points B′ and C′, where the warm tails of the PDF far exceeded the peak mean temperature. At point D′, which was off-centre by only $1.65L_{22,2}$, the local temperature only rarely exceeded the peak mean temperature, whereas at the more distant points E′ and F′ the temperature never came close to the peak value. One may speculate that most of the PLS was likely subjected to initial condition effects, but heat conduction reduced the maximum local temperature value in the outer PLS regions to levels below the centreline average.

Figure 14 may also be used to examine the transport of unheated ("cold") fluid into the PLS. A great deal of cold fluid was present at point F′, close to the PLS edge, and some cold fluid was found at point E′, but no cold fluid was detectable at point D′, which

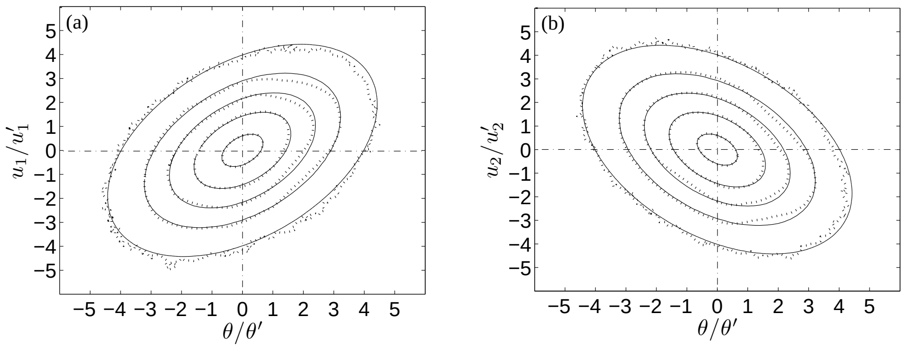

Figure 15: Isocontours of the JPDF of the scalar and (a) the streamwise and (b) the transverse velocity fluctuations in the UTG; dashed lines have been fitted to measured contours with values (from the outer one towards the inner one) equal to 0.00001, 0.001, 0.01, 0.05, 0.14; solid lines indicate the corresponding contours of a jointly Gaussian PDF with the same correlation coefficient as the measurements.

was half-way across the PLS. Once more, it appears that heat conduction reduced the difference between the temperature that a fluid particle had at the start of its random walk and the average local temperature at its current location.

On a final note, one may observe that the temperature skewness and flatness factors increased drastically from the centre towards the edges of the PLS, as a result of the corresponding PDF becoming increasingly one-sided and pointed. This is clear evidence against the use of a single PDF shape to describe the entire scalar field.

4.3. *Velocity–temperature JPDF*

Isocontours of the JPDF of the temperature and the streamwise and transverse velocity components for the UTG, TML and PLS fields are, respectively, shown in figures 15, 16 and 17. A general observation from these figures is that the orientations of the axes of all $u_2 - \theta$ contours, which are connected to the sign of $\overline{u_2\theta}$, are consistent with gradient transport. Moreover, the $u_1 - \theta$ contour sets are roughly mirror images (with respect to the velocity axis) of the corresponding $u_2 - \theta$ contour sets; this is attributed to the strong negative correlation of u_1 and u_2. Both velocity–temperature JPDF in the UGT field were approximately Gaussian, whereas in the TML and the PLS they were distinctly non-Gaussian.

At the TML centre (point A), the JPDF contours were nearly anti–symmetric. All contours could be fitted visually by axes with comparable inclinations, which means that at all JPDF levels the temperature–velocity correlations had the same signs as

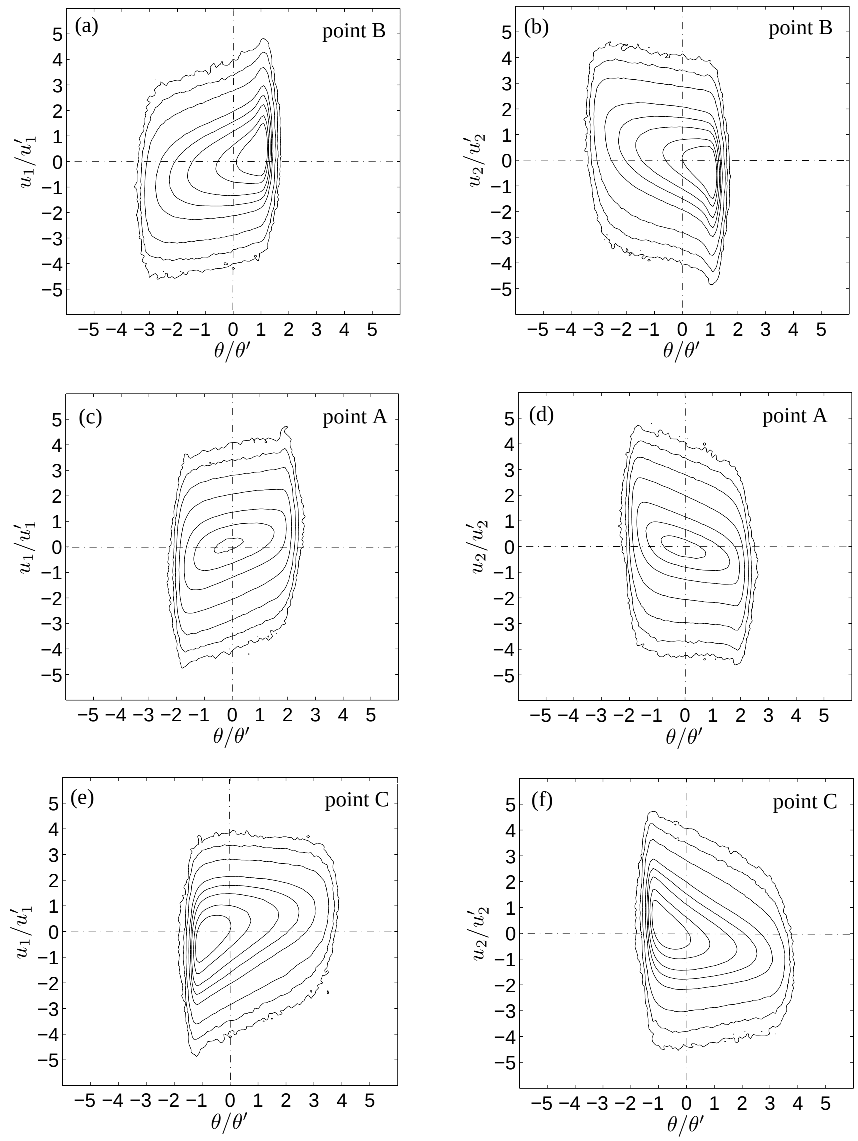

Figure 16: Temperature-velocity JPDF isocontours in the TML; solid lines have been fitted to measured contours with values (from the outer one towards the inner one) equal to 0.00001, 0.0001, 0.001, 0.0025, 0.005, 0.01, 0.1 and 0.14; for point A, contours with values 0.0025 are not shown in the plots.

the corresponding overall turbulent heat fluxes. The inner (high–value) contours were roughly elliptical (*i.e.*, Gaussian-like), but the contour shapes gradually evolved towards flat–sided ones as the contour values decreased so that, for large temperature fluctuations, the low–value contours were nearly parallel to the velocity axis. This means that, on rare

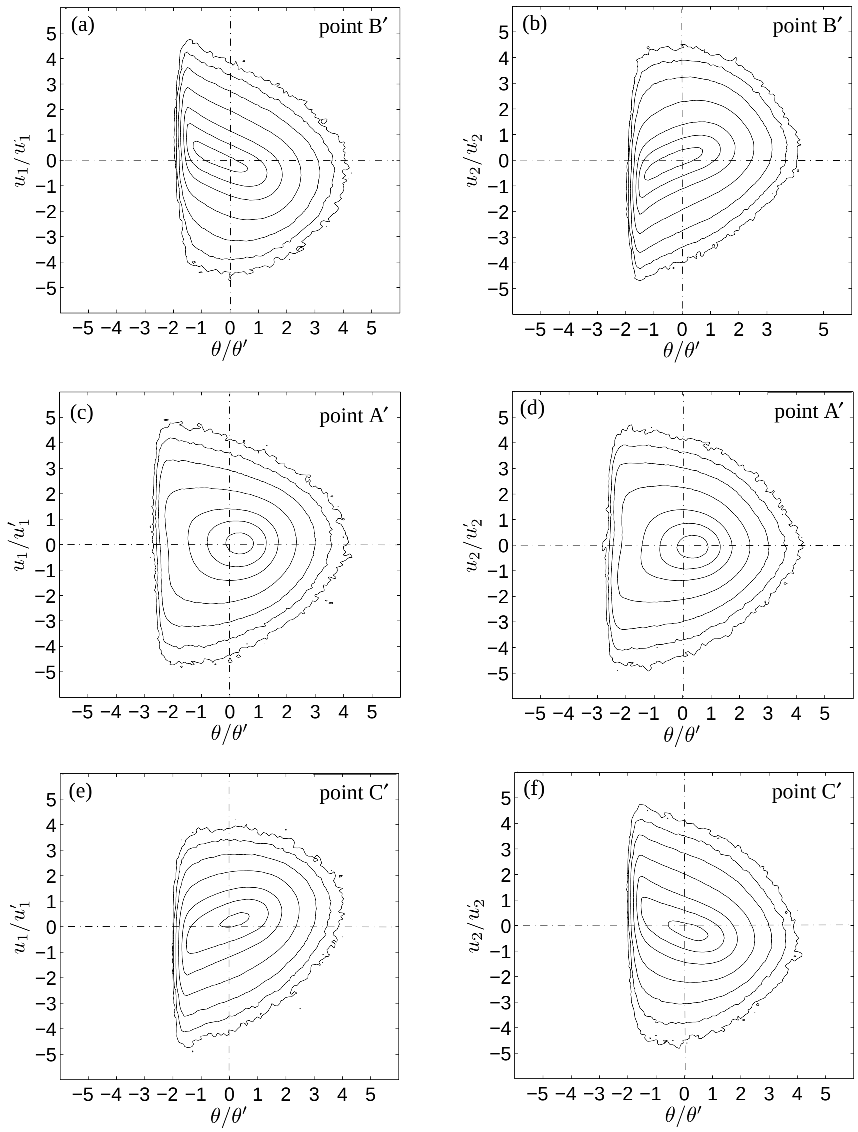

Figure 17: Temperature-velocity JPDF isocontours in the PLS; solid lines have been fitted to measured contours with values (from the outermost contour towards the innermost one) equal to 0.00001, 0.0001, 0.001, 0.005, 0.01, 0.1 and 0.14.

occasions, very warm or very cool fluid was transported to the TML centre by both strong upwards moving eddies and strong downward moving eddies. This appears to contradict the gradient transport premise that scalar fluctuations would correspond to differences between local means. However, it may be explained as the result of extreme instances of wandering of the instantaneous thermal mixing layer, such that, for example, warm fluid first wandered to an extremely low level and then returned to its average level (and possibly beyond it) by crossing the TML centre.

At point B of the TML, the JPDF isocontours were asymmetric: on the cool side they maintained elongated shapes until the contour values became very low, whereas on the warm side they were all flat–sided. At point C of the TML, the JPDF isocontours were roughly mirror images (with respect to the temperature axis) of those at point B. The shapes of the contours at points B and C can be explained by arguments similar to those used for point A. An interesting observation is that the temperature at any of these three points never reached either of the extreme values of the unheated or fully heated streams (see table 4). This issue will be further discussed in a following section.

The JPDF isocontours in the PLS resembled those in the TML on the cool side but had very different shapes on the warm side. Contours with high JPDF values were elongated and maintained elongated shapes towards the warm side at all contour values. In contrast, contours with low JPDF values were flat–sided on the cool side, which may be explained in the same fashion as for the TML. At the PLS mean peak (point A′), the contours were approximately symmetric with respect to the velocity axis, as may be expected by the near–symmetry of the mean scalar field and the near–homogeneity of the turbulence. Isocontours at point B′ were approximately mirror images of corresponding isocontours at point C′, which is also consistent with the mean property variation in this field.

4.4. *Velocity conditional expectations*

The velocity expectations, conditioned on the temperature value (VCE), for the three scalar fields are shown in figure 18. One may readily observe that the shapes of the streamwise VCE were essentially mirror images of the transverse VCE, a fact that is attributed to the strong correlation between the two velocity components. In the UTG field, these VCE were linear, in conformity with the previously observed joint normality of the corresponding velocity and temperature fluctuations. In the two inhomogeneous temperature fields, however, the VCE were strongly non-linear and had shapes that depended on the type of scalar field as well as on the location within this field. In the TML the VCE were monotonic but inflected, whereas in the PLS they seemed to have very mild extrema and were not inflected at all. In the UTG and the TML large temperature fluctuations of either sign were, on the average, transported by strong velocity

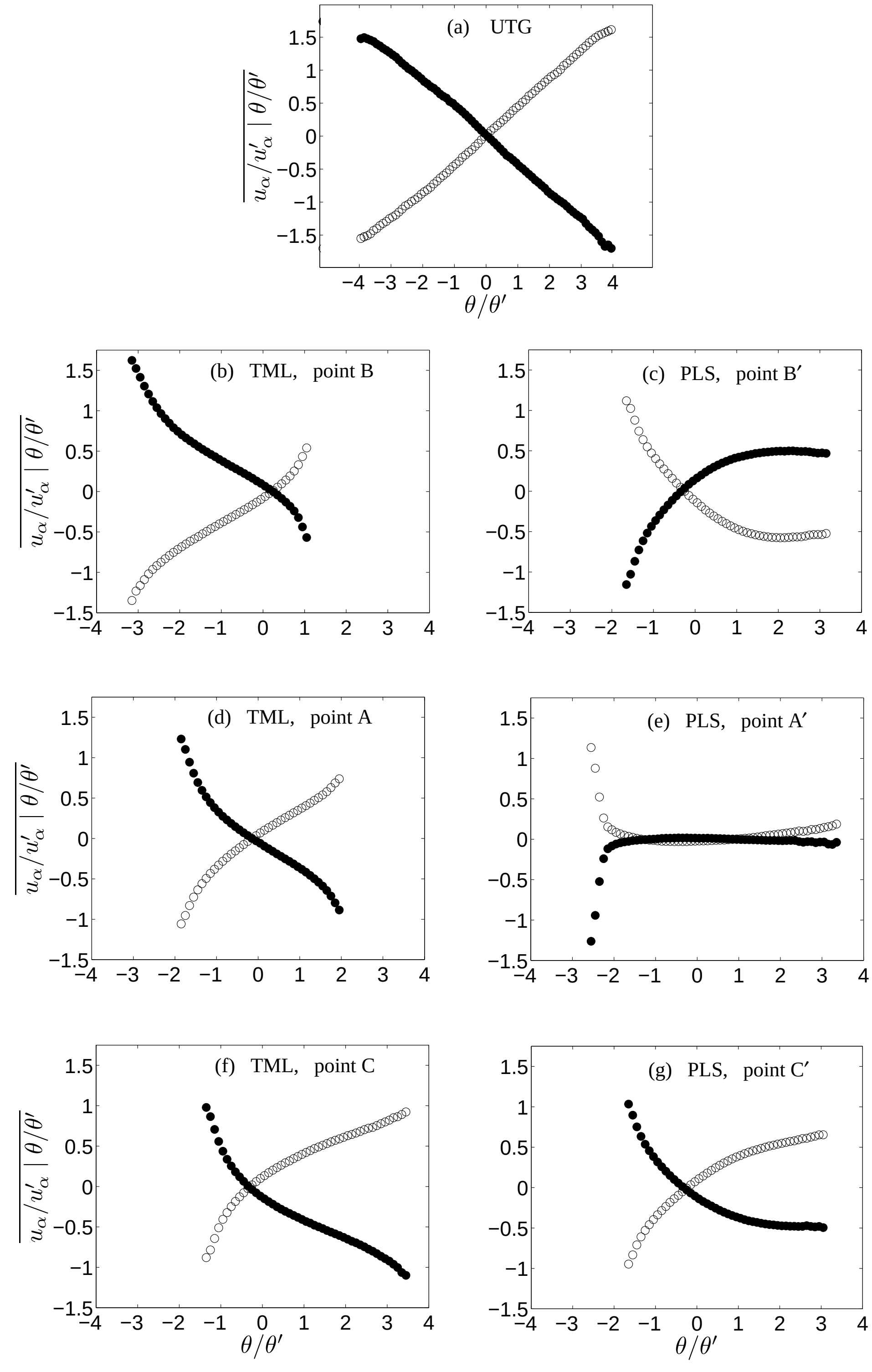

Figure 18: Velocity conditional expectations in the UTG, TML and PLS fields; ○: $\alpha = 1$; ●: $\alpha = 2$.

fluctuations, whose sign was consistent with gradient transport. In the PLS, this was also the case for large negative temperature fluctuations, but not for large positive ones; the average velocity fluctuations transporting large positive temperature fluctuations were nearly zero in the PLS centre and approached moderate asymptotes at the two off-centre positions.

4.5. *Events with strong transverse velocities*

To gain insight into the phenomena that are responsible for the observed shapes of the PDF and JPDF, we need to examine transport events with velocity and temperature fluctuations that are far from the corresponding averages, as averages cannot reveal the contributions of individual events and are insensitive to rare events. Towards this purpose, we have identified all events with large values of transverse velocity fluctuations and examined simultaneously the transverse and streamwise velocity fluctuation values and the temperatures of the corresponding fluid parcels. All events with strong transverse velocity fluctuations are shown as points in figure 19, together with the corresponding instantaneous streamwise velocity and temperature rise values. To identify such events, we used the condition $|u_2/u_2'| \geqslant 3$. These events were very rare, as their total frequency of occurrence (probability) was 0.8% (see figure 12a); the frequency of occurrence for events with $|u_2/u_2'| \geqslant 4$ was 0.03% and that for events with $|u_2/u_2'| \geqslant 5$ was 3.5×10^{-4}%. It is important to note that the statistical samples of signals used in this presentation were fully time–resolved and extended over times that were of the order of 10^6 integral timescales. Thus, we are confident that our measurements have captured all possible events, even the most rare ones.

In the UTG field, the warmest fluid parcels had mostly large negative transverse velocities and much larger than average streamwise velocities, whereas the coolest parcels had mostly large positive u_2 and large negative u_1. Events with the opposite properties may also be observed, but these were even more rare than the former events. In general, the distant migration of fluid parcels in UTG is compatible with gradient transport. Similar conclusions can be reached from figure 19 for the TML. In contrast, extreme temperature events in the PLS had a more complex behaviour. The motions of fluid parcels with very low temperatures were compatible with gradient transport as these parcels generally had large u_1 and u_2 of opposite signs. However, very warm parcels with large u_2 were extremely rare and those that existed had moderate u_1 in most cases. As also illustrated in

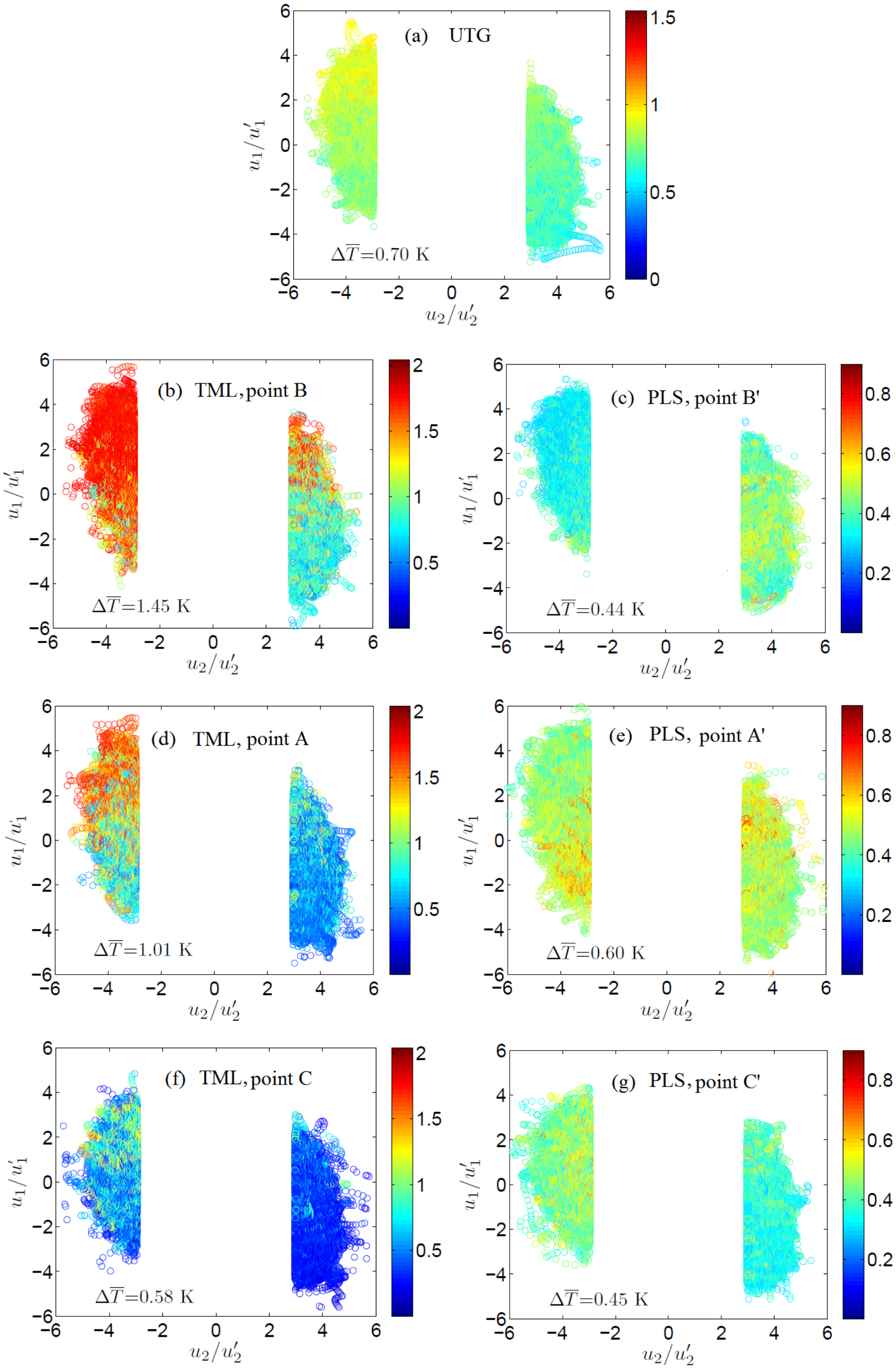

Figure 19: Typical maps of events with large values of the instantaneous transverse velocity fluctuation; the instantaneous values of temperature rise in K are indicated by the colour of each point. The unheated stream temperature was $\Delta\overline{T}_{cold} = 0$ for all cases, whereas $\Delta\overline{T}_{hot}$ was the highest mean temperature rise across the UTG profile (=1.51 K), the mean temperature of the heated stream for the TML (=2.04 K) and the peak mean temperature for the PLS profile (=0.60 K). The presented values in the plots are local mean temperatures.

the velocity–temperature JPDF (figure 17), parcels with the highest temperatures at the centre and at the two inflection points of the PLS had small velocity differences from the local averages and so likely originated in the central region of the PLS. At the PLS centre, where the mean temperature gradient vanished, this observation is compatible with gradient transport; however, at the two inflection points, where the mean temperature gradient had maxima, gradient transport is contradicted by the observations.

5. Additional discussion

5.1. *Maximum turbulent mixing length and its connection to scalar transport*

In this subsection, we will introduce a random walk model to estimate the maximum mixing distance across the USF, which will be consequently used to explain the observations that were made in the previous section. This model is only approximate and meant to be used for qualitative analyses. For convenience, mean velocity and mean temperature profiles will be represented by the fitted analytical expressions, which were in all cases very close to the measurements.

Let us first consider a point P1 on the centreline of the USF and a second point P2 at the same streamwise distance from the origin as P1 but at a transverse distance δx_2 from it. Points P2 that are located above P1 (namely, towards the mean velocity gradient direction) would have $\delta x_2 > 0$ and points located below P1 would have $\delta x_2 < 0$. The ratio $\delta x_2 / L_{22,2}$ represents a relative mixing length and will be used as the independent variable. Let us now consider a fluid particle that performed a random walk such that at the origin of time it was located at an upstream position having the same level as point P2, whereas at the current time it was located at point P1. During this time, the particle would, of course, have moved spanwise as well, but this is of no consequence to the present analysis, because all fields of interest are two-dimensional on the mean. Because the streamwise rate of change of all mean fields was much weaker than their transverse rate of change, one may approximate the values of the mean fields on the plane of particle origin by those on the plane of current location. Following classical turbulent mixing arguments, one may assume that the particle maintained its original velocity (or, more appropriately, its original momentum), which is taken to be the mean velocity at P2, while located at P1, where the mean velocity is equal to the USF centreline velocity. Then, this particle would appear to have an instantaneous streamwise "nominal velocity fluctuation" δu_1

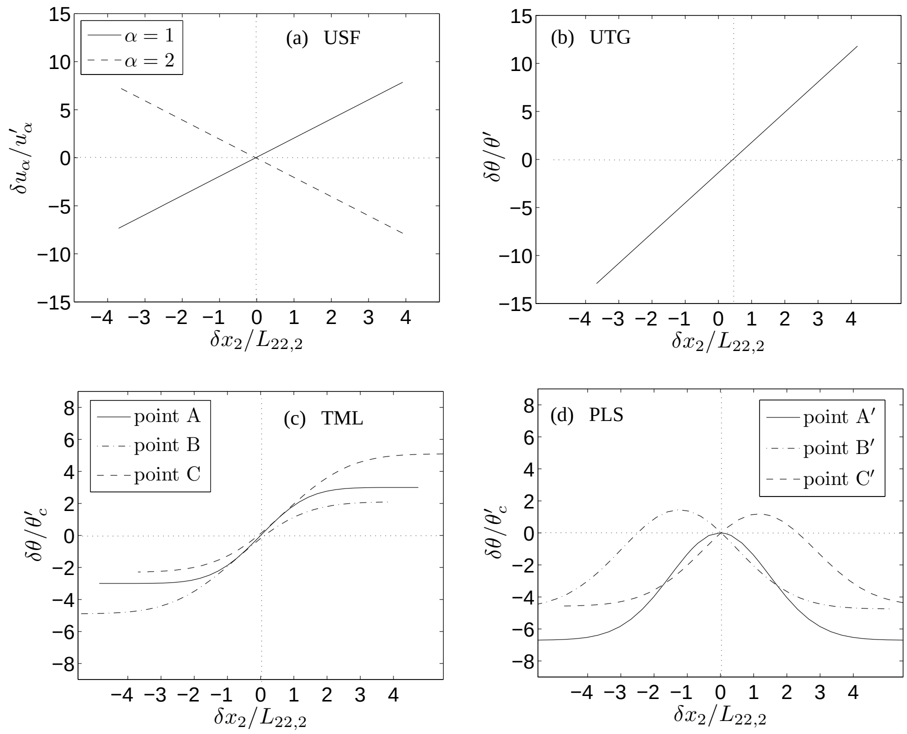

Figure 20: (a) Normalized nominal velocity fluctuations vs. normalized turbulent mixing distance in the USF; the lines have slopes ± 2.1. (b-d) Normalized nominal temperature fluctuations in the three fields vs. normalized turbulent mixing distance. (b) The plotted line has a slope of 3.1; (c) the lines represent fitted error functions; θ'_c is the temperature standard deviation at the centre of the TML (point A); and (d) the lines represent fitted Gaussian functions; θ'_c is the temperature standard deviation at the centre of the PLS (point A′).

that would be equal to the difference between the mean velocities at points P2 and P1. This and subsequent fluctuations will be normalised by the corresponding measured standard deviations at the current particle location. In the present USF, $\delta u_1/u'_1$ would be an increasing linear function of $\delta x_2/L_{22,2}$, as illustrated in figure 20a. Although $\delta u_1/u'_1$ should have no upper and lower bounds in an ideal USF, the PDF shown in figure 12a demonstrates that, in the present flow, this parameter was confined within the range from approximately -5 to 5. The ± 5 limits in figure 20a intersect the fluctuations at approximately $\delta x_2/L_{22,2} \approx \pm 2.3$. This observation is consistent with the well–accepted notion that, at least in nearly homogeneous turbulence, turbulent eddies would travel as far as approximately two integral length scales.

Although gradient transport notions dictate that particles arriving at P1 with a positive δu_1 would typically have a negative nominal transverse velocity fluctuation δu_2, it is not possible to estimate directly the magnitude of the latter. Nevertheless, one may take advantage of the fact that u_1 and u_2 are strongly negatively correlated in USF, particularly when they have large magnitudes, as the result of actions of horseshoe–shaped coherent structures (Vanderwel & Tavoularis 2011). Assuming a perfect correlation between the two velocity components, one may plot a roughly estimated $\delta u_2/u_2'$ *vs.* $\delta x_2/L_{22,2}$, as in figure 20a. The fact that the $\delta x_2/L_{22,2}$ values corresponding to $\delta x_2/L_{22,2} = \pm 2$ are close to the extreme values in the PDF of u_2 (figure 12a) indicates that the present random walk model is fairly realistic.

Now, we will apply the same random walk model to explain previous observations on scalar transport. We will assume that a particle that originated at the P1 level maintains its temperature at a value equal to the mean temperature at P1 and so, when it reaches the P2 level, it appears to have a "nominal temperature fluctuation" $\delta\theta$, which is equal to the difference between the mean temperatures at points P2 and P1. The variations of $\delta\theta/\theta'$ across the three scalar fields of interest are shown in figures 20b–d. In the UTG and TML cases (figures 20b and c), values of $\delta\theta/\theta'$ corresponding to $\delta x_2/L_{22,2} = \pm 2$ were close to the extreme values in the corresponding scalar PDF (figures 13a and b), which supports the plausibility of the presented random walk model for the scalar mixing in those two cases. Similar arguments also apply to the two edges of the PLS, where the nominal temperature fluctuations are bounded by the temperature of the unheated flow. In sharp contrast, however, gradient transport arguments fail drastically to describe the nominal temperature fluctuations in the PLS central region: at point A′ (PLS centre), such arguments predict no positive temperature fluctuations at all, whereas at points B′ and C′, the highest $\delta\theta$ are much lower than the highest observed local temperature fluctuations. This observation supports our postulate that high positive temperature fluctuations in the PLS core are remnants of the heat source near-field.

5.2. *Estimates of heat conduction effects*

In a previous section, we observed that the cold tail of the temperature PDF at an intermediate location in the PLS, where fluid particles originating in the unheated flow stream would be expected to penetrate occasionally, did not reach as far as the unheated fluid temperature. Similar observations would likely apply to locations at moderate distances from an edge of any scalar field that is bounded by fluid with a uniform scalar value.

In this section, we present a rough evaluation of the hypothesis that heat conduction (a phenomenon that is entirely the result of molecular random motions in the fluid) would introduce sufficient local mixing to explain this apparent paradox. Although this analysis is necessarily quantitative, its results were meant to be used for qualitative purposes only.

From the outset of this analysis, it is clear that we are concerned with rare, exceptionally strong transport incidents, during which a fluid particle travels to a far transverse distance from its location of origin. In USF, such incidents have been found by Vanderwel & Tavoularis (2011) to occur as the result of the actions of hairpin vortices, whose legs are elongated and only moderately inclined with respect to the streamwise direction. The average distance between the legs of the hairpin vortices was found to be about $1.6\lambda_{11}$, which is consistent with the hypothesis of Tennekes (1968) that the distance between the branches of looping vortex tubes is comparable to λ_{11}. In view of these observations, we may consider a rare transport event that consists in the "ejection" of an unheated cylindrical fluid particle with a diameter λ_{11} (which in the present flow is 6.8 mm) by a hairpin vortex towards regions of warmer fluid in the PLS (or the TML, as this case is covered as well). While the fluid particle moves transversely, let's say with the extreme transverse velocity $5u'_2$, it would also be convected streamwise, let's say with the centreline velocity $\overline{U}_c$. Therefore, during the time it would take it to traverse a transverse distance Δx_2, the particle would also be convected by a streamwise distance Δx_1, such that the transport time would be $\Delta t \approx \Delta x_2/(5u'_2) \approx \Delta x_1/\overline{U}_c$. During this time, the particle would be subjected to heat conduction with its surroundings, which we may assume have a temperature equal to the local mean temperature.

As a representative example of the application of this approach, consider a fluid particle that originated at the level of point G′ in the PLS, namely at the edge of the unheated fluid, and at the current time was found to be at the level of point D′, where the mean temperature rise was 0.25 K and the lowest measured value of the temperature rise was 0.04 K. The distance between the levels of points G′ and D′ is $\Delta x_2 \approx 2.5L_{22,2} \approx$ 57 mm and so the transport time would be $\Delta t \approx \Delta x_2/(5u'_2) \approx 0.040$ s. The streamwise convection distance of the particle would be $\Delta x_1/ \approx \overline{U}_c\Delta t \approx 0.30$ m, which is very plausible for the present facility, in which the heating screen was located 1.67 m upstream of the main measuring plane.

For a very rough estimate of heat conduction, let's assume that the cylindrical fluid particle had an initial temperature equal to that of the unheated flow and was during its migration surrounded by fluid with a temperature rise of 0.25 K. Assume that heat transfer between this fluid particle and its surroundings takes place only by conduction; it is noted that, if some convective heat transfer were present at the same time, its effect would be to further raise the temperature of this particle. An exact solution is readily available for this transient heat conduction problem (Ozisik 1993). This solution predicts that, following time $\Delta t \approx 0.040$ s, the temperature on the axis of this particle would be 0.04 K. This value is comparable to the lowest measured temperature of 0.05 K at point D$'$. Despite its crude approximations, this analysis is sufficient to demonstrate, at least qualitatively, that heat conduction was strong enough to truncate the tails of the temperature PDF, especially near the edges of the scalar fields. Of course, molecular effects would depend strongly on the value of the Prandtl (or Schmidt) number and would weaken with an increase in the value of this parameter.

6. Conclusions

The present study has examined experimentally several issues related to the shape of the scalar PDF in inhomogeneous scalar fields transported by turbulent shear flows. Simultaneous measurements of the fluctuating velocity and temperature fields have been made in uniformly sheared turbulence, in which a homogeneous temperature fluctuation field, or one of two inhomogeneous ones, were superimposed passively. These temperature fields included one with a uniform mean temperature gradient (UTG), a thermal mixing layer (TML) and the plume of a heated line source (PLS). The scalar PDF and the velocity-scalar joint PDF, as well as velocity conditional expectations, were measured and analysed. Because all three scalar fields were superimposed on the same nearly homogeneous turbulent flow, it was possible to evaluate the effects of the mean scalar profile and scalar initial conditions. The availability of extremely long data records in this work also permitted the detection of rare events.

The scalar PDF was essentially Gaussian in the UTG field, as the result of thorough mixing of fluid with practically unbounded temperatures on both the warm and cold sides. In contrast, the scalar PDF was distinctly non-Gaussian in the TML and the PLS. At the centre of the TML, both tails of the scalar PDF were bounded by values set by the warm and cold streams, whereas, at the centre of the PLS, the cold tail was bounded while the warm tail was nearly Gaussian, a phenomenon attributed to sustained temperature fluctuations introduced by the heating source. It was thus concluded that the reasons for the approximate Gaussianity of the scalar PDF in the UTG field and the warm side of the PLS are fundamentally different. The joint velocity-temperature PDF were nearly Gaussian in the UTG field but strongly non-Gaussian in the TML and the PLS. The shapes of the JPDF could be explained by arguments similar to those made for the corresponding scalar PDF. In conformity with the previous observations concerning Gaussianity of the scalar and joint fluctuation fields, the velocity expectations, conditioned upon the scalar values, were linear in the UTG field and strongly non-linear in the TML and the PLS. However, the non-linearity characteristics were different in the two inhomogeneous scalar fields. In the TML, the conditional velocity expectations were inflected, as temperature fluctuations on both the cool and the warm sides were restricted by the temperatures of the two far streams. On the cool side of the PLS, the conditional velocities were similar to those in the TML. In contrast, on the warm side, it was the velocity expectations that appeared to be bounded; this may be attributed to the fact that warmer fluid was transported from a range of intermediate distances, including some short distances on both sides of the measurement points and so the average conditional velocity for a given temperature value was relatively small.

Financial support by the Natural Sciences and Engineering Research Council of Canada (NSERC) is gratefully acknowledged. We thank Professor Petar Vukoslavčević for fabricating our hot- and cold-wire probes.

REFERENCES

Browne, L. W. B., Antonia & R. A., Chua, L. P. 1989 Calibration of x-probes for turbulent flow measurements. *Exp. Fluids* **7**, 201–208.

Feng, H., Olsen, M, G., Hill, J. C. & Fox, R. O. 2007 Simultaneous velocity and concentration field measurements of passive-scalar mixing in a confined rectangular jet. *Exp. Fluids* **42**, 847–862.

Feng, H., Olsen, M. G., Fox, R. O. & Hill, J. C. 2008 Conditional statistics of passive-scalar mixing in a confined wake flow. *Phys. Fluids* **20**, 077105.

Ferchichi, M. & Tavoularis, S. 1992 Evolution of a thermal mixing layer in uniformly sheared turbulent flow. *Phys. Fluids A* **4**, 997–1006.

Ferchichi, M. & Tavoularis, S. 2000 Reynolds number effects on the fine structure of uniformly sheared turbulence. *Phys. Fluids* **12** (11), 2942–2953.

FERCHICHI, M. & TAVOULARIS, S. 2002 Scalar probability density function and fine structure in uniformly sheared turbulence. *J. Fluid Mech.* **461**, 155–182.

GARG, S. & WARHAFT, Z. 1998 On the small scale structure of simple shear flow. *Phys. Fluids* **10**, 662–673.

GYLFASON, A. & WARHAFT, Z 2004 On higher order passive scalar structure functions in grid turbulence. *Phys. Fluids* **16**, 4012–4019.

KAILASNATH, P., SREENIVASAN, K. R. & SAYLOR, J. R. 1993 Conditional scalar dissipation rates in turbulent wakes, jets, and boundary layers. *Phys. Fluids A* **5**, 3207–3215.

KARNIK, U. & TAVOULARIS, S. 1987 Generation and manipulation of uniform shear with the use of screens. *Exp. Fluids* **5**, 247–254.

KARNIK, U. & TAVOULARIS, S. 1989 Measurements of heat diffusion from a continuous line source in a uniformly sheared turbulent flow. *J. Fluid Mech.* **202**, 233–261.

LARUE, J. C., DEATON, T. & GIBSON, C. H. 1975 Measurement of high-frequency turbulent temperature. *Rev. Sci. Instrum.* **46**, 757–764.

LARUE, J. C. & LIBBY, P. A. 1981 Thermal mixing layer downstream of half-heated turbulence grid. *Phys. Fluids* **24**, 597–603.

LAVERTU, R. A. & MYDLARSKI, L. 2005 Scalar mixing from a concentrated source in turbulent channel flow. *J. Fluid Mech.* **528**, 135–172.

LEMAY, J., BENAISSA, A. & ANTONIA, R. A. 2003 Correction of cold-wire response for mean temperature dissipation rate measurements. *Exp. Therm. Fluid Sci.* **27**, 133143.

LEPORE, J. & MYDLARSKI, L. 2011 Lateral dispersion from a concentrated line source in turbulent channel flow. *J. Fluid Mech.* **678**, 417–450.

LI, J. D. & BILGER, R. W. 1994 A simple theory of conditional mean velocity in turbulent scalar-mixing layer. *Phys. Fluids* **6**, 605–610.

LI, J. D., J. D. & BILGER, R. W. 1996 The diffusion of conserved and reactive scalars behind line sources in homogeneous turbulence. *J. Fluid Mech.* **318**, 339–372.

MA, B. & WARHAFT, Z. 1986 Some aspects of the thermal mixing layer in grid turbulence. *Phys. Fluids* **29**, 3114–3120.

MYDLARSKI, L. 2003 Mixed velocity–passive scalar statistics in high-reynolds-number turbulence. *J. Fluid Mech.* **475**, 173–203.

MYDLARSKI, L. & WARHAFT, Z. 1998 Passive scalar statistics in high-péclet-number grid turbulence. *J. Fluid Mech.* **358**, 135–175.

OZISIK, M. N. 1993 *Heat Conduction, 2nd E.*. John Wiley & Sons Inc., NewYork.

POPE, S. 2000 *Turbulent Flows*. Cambridge University Press, New York.

POPE, S. B. 1985 Pdf methods for turbulent reactive flows. *Prog. Energy Combust. Sci.* **11**, 119–192.

TAVOULARIS, S. 1983 Simple corrections for the temperature sensitivity of hot wires. *Rev. Sci. Instrum.* **54**, 741–743.

Tavoularis, S. 1985 Asymptotic laws for transversely homogeneous turbulent shear flows. *Phys. Fluids* **28** (3), 999–1001.

Tavoularis, S. 2005 *Measurement in Fluid Mechanics*. Cambridge University Press, New York.

Tavoularis, S. & Corrsin, S. 1981 Experiments in nearly homogeneous turbulent shear flow with a uniform mean temperature gradient. Part 1. *J. Fluid Mech.* **104**, 311–347.

Tavoularis, S. & Karnik, U. 1989 Further experiments on the evolution of turbulent stresses and scales in uniformly sheared turbulence. *J. Fluid Mech.* **204**, 457–478.

Tennekes, H. 1968 Simple model for the small-scale structure of turbulence. *Phys. Fluids* **11**, 669–671.

Tong, C. & Warhaft, Z. 1995 Passive scalar dispersion and mixing in a turbulent jet. *J. Fluid Mech.* **292**, 1–38.

Uberoi, M. S. & Corrsin, S. 1953 1952 Diffusion of heat from a line source in isotropic turbulence. *Tech. Rep.*. NACA Rep. no. 1142. (See also NACA TN no. 2710.).

Vanderwel, C. & Tavoularis, S. 2011 Coherent structures in uniformly sheared turbulence. *J. Fluid Mech.* **689**, 434–464.

Vanderwel, C. & Tavoularis, S. 2014 Measurements of turbulent diffusion in uniformly sheared flow. *J. Fluid Mech.* **754**, 488–514.

Venkataramani, K. S. & Chevray, R. 1978 Statistical features of heat transfer in grid-generated turbulence: constant-gradient case. *J. Fluid Mech.* **86**, 513–543.

Warhaft, Z. 2000 Passive scalars in turbulent flows. *Annu. Rev. Fluid Mech.* **32** (1), 203–240.

5.2 Passive scalar fine structure in uniformly sheared turbulence

This section contains a draft for the second manuscript, entitled "Measurements of non-homogeneous scalar fine structure in homogeneous turbulence" which is intended to be submitted for publication in the Journal of Fluid Mechanics.

Under consideration for publication in J. Fluid Mech.

Measurements of scalar fine structure in homogeneous turbulence

A. Behnamian, S. Tavoularis †

Department of Mechanical Engineering, University of Ottawa, Ottawa, Ontario, Canada

(Received —)

Previous measurements of statistical properties of three temperature fluctuation fields embedded passively in uniformly sheared turbulence are complemented in this article with measurements pertaining to their fine structures. These temperature fields were a nearly homogeneous one, generated by a uniform mean temperature gradient, and two inhomogeneous ones, a thermal mixing layer and the plume of a heated line source. Simultaneous measurements of the local temperature and all its derivatives were made with fine resistance thermometers (cold wires). The probability density functions (PDF) of the scalar dissipation rate and its three parts departed from the log-normal PDF in all fields. The expectation of the scalar dissipation rate, conditioned upon the scalar value, was found to be anisotropic in all scalar fields. In the homogeneous scalar field, all conditional dissipation parts had approximately similar shapes, which justifies the use of the streamwise part as a surrogate for the total; in contrast, in the two inhomogeneous scalar fields, the transverse part had a very different shape from those of the other two, which means that the total cannot be surrogated by any of its parts. The scalar dissipation rate was found to be approximately independent of the scalar fluctuation value only in the UTG field, whereas in the two other fields the former was strongly dependent on the latter in ways that were specific to each field and the location of measurement.

Key Words: Turbulence, Homogeneous Turbulence, Uniformly Sheared Flow, Homogeneous Shear Flow, Turbulent Mixing, Intermittency

---

† Email address for correspondence: stavros.tavoularis@uottawa.ca

1. Introduction

In a companion article (Behnamian & Tavoularis 2015), hereafter referred to as Part 1, we have reported results of experimental investigations of turbulent transport of three temperature (as representative of a transported scalar property) fluctuation fields superimposed passively on a uniformly sheared flow (USF). These fields included a nearly homogeneous one that was generated by a uniform mean temperature gradient (UTG) and two inhomogeneous temperature fields, namely a thermal mixing layer (TML) and the plume of a heated line source (PLS). In that article we presented measurements of overall statistical properties of these fields, including temperature probability density functions (PDF), joint velocity-scalar probability density functions (JPDF) and expectations of the velocity components conditioned upon the scalar fluctuation values. The objective of Part 1 was to contribute to the available database for the development of realistic models that permit the solution of the scalar PDF equation (Pope 1985) as well as to our general understanding of turbulent transport and mixing. The choice of the three scalar fields was such it became possible to evaluate separately the effects of scalar inhomogeneity and scalar initial conditions on turbulent transport: the UTG fluctuation field was both homogeneous and free of initial effects; the TML was inhomogeneous, yet also essentially free of initial effects; in contrast, the PLS was both inhomogeneous and with sustained initial effects. The observed significant differences among the scalar PDF and joint properties in the three scalar fields were explained by consideration of the differences in the mean scalar fields and the residual effects of initial heat injection. In the present Part 2, we complement the results of Part 1 with measurements of the PDF of all three scalar derivatives, the PDF of the scalar dissipation rate, expectations of the scalar dissipation rate and its components, conditioned upon the scalar value, and other scalar fine structure properties in the same three scalar fields and the same uniformly sheared turbulence. This is one of very few experimental documentations of simultaneous statistics of all three scalar derivatives; together with results in Part 1, results in Part 2 provide measurements of all terms in the scalar PDF equation that require modelling.

2. Literature review

Among the most important indicators of the scalar fine structure are various statistical properties of the spatial derivatives of the scalar fluctuation field (Tavoularis & Corrsin

1981b). Local isotropy of the scalar (Kolmogorov 1941; Obukhov 1949; Corrsin 1951) would strictly require that all odd-order moments of all scalar derivatives should vanish; however, the skewnesses of scalar derivatives in many experimental configurations have been found to be non-zero, a phenomenon that has been attributed to the ramp-cliff shape of scalar variation (Sreenivasan & Antonia 1977). Even-order moments, such as the flatness of scalar derivatives, are indicators of the internal intermittency of scalar fields and generally attain values that are significantly larger than the Gaussian value of 3. In the presence of a turbulent/non-turbulent interface, scalar derivative statistics would also be complicated by external intermittency, the length scale of which would normally be much larger than that of internal regions with intense dissipative activity (Tong & Warhaft 1994). The present interest, however, focusses on fully turbulent flows that are free of external intermittency and solid wall effects.

Most experimental studies of scalar fine structure have reported mainly statistics of the streamwise scalar derivative, which is conveniently estimated from the temporal derivative of the scalar time history via Taylor's "frozen flow" approximation. Statistics of transverse scalar derivatives have also been reported by some authors for grid-generated turbulence (Tong & Warhaft 1994; Mydlarski & Warhaft 1998), boundary layers (Sreenivasan *et al.* 1977; Anselmet *et al.* 1994), USF (Tavoularis & Corrsin 1981b; Ferchichi & Tavoularis 2002), a plain jet (Antonia *et al.* 1986a), a round jet (Anselmet *et al.* 1994; Mi *et al.* 1995) and a fully developed turbulent channel flow (Germaine *et al.* 2014).

Several authors have reported measurements of non-zero skewnesses of streamwise and transverse scalar derivatives in shear flows. In a USF with UTG, Sreenivasan & Tavoularis (1980) showed that the magnitude of the streamwise skewness would depend directly on the mean scalar gradient and indirectly on the mean shear and it would approach an asymptotic value of near one; they also suggested that the sign of this skewness would be opposite to the product of the signs of the mean transverse scalar and velocity derivatives. Tavoularis & Corrsin (1981b) extended this argument to suggest that the sign of the skewness of the transverse scalar derivative would be opposite to that of the streamwise one. These relationships for the signs of the scalar derivative skewnesses were also found to apply to the wake of a heated cylinder, in which both the turbulence and the scalar field were inhomogeneous (Tavoularis & Sreenivasan 1981). The skewness of the spanwise scalar derivative (namely in the direction that was normal both to the flow and to the mean scalar gradient) has also been measured (Sreenivasan *et al.* 1977; Tavoularis & Corrsin 1981b); in these cases, however, this skewness was found to be negligible, as the result of the two-dimensionality of the flow and scalar fields. Sreenivasan (1991) and Sreenivasan & Antonia (1997) compiled measurements of the streamwise scalar skewness and plotted them *vs.* the turbulent Reynolds number. These results exhibited large scatter and had no discernible trend (see also Warhaft (2000)).

The flatness of scalar derivatives in shear flows was consistently found to be significantly larger than the Gaussian value. The streamwise derivative flatness was generally approximately 30% higher than the transverse and spanwise derivative flatnesses (Sreenivasan *et al.* 1977; Tavoularis & Corrsin 1981b; Mi *et al.* 1995). A compilation of results from different experiments (Sreenivasan & Antonia 1997) has shown that the flatness factors of all scalar derivatives increased with turbulent Reynolds number at approximately the same rate.

Some of the previously mentioned studies also presented PDF of scalar derivatives. The tails of these PDF were always stretched far beyond the Gaussian tails, in a quasi-exponential manner. Ching (1991) and Holzer & Siggia (1994) suggested that the tails of the streamwise scalar derivative PDF follow the expression $exp(-C_1 \mid \partial\theta/\partial x_1 \mid^{\alpha_1})$, where C_1 and α_1 are constants. Ferchichi & Tavoularis (2002) reported that the coefficients of fitted exponential expressions to each tail of both the streamwise and transverse scalar derivative PDF in a USF with UTG were in the ranges $1.9 \leqslant C_1 \leqslant 2.1$ and $0.72 \leqslant \alpha_1 \leqslant 0.87$.

The instantaneous value of the scalar dissipation rate (or, more accurately, the rate of destruction of scalar fluctuations by molecular motions) is defined as $\varepsilon_\theta = \varepsilon_{\theta 1} + \varepsilon_{\theta 2} + \varepsilon_{\theta 3}$, where, for example, $\varepsilon_{\theta 1} = \gamma\ (\partial\theta/\partial x_1)^2$ and γ is the molecular or thermal diffusivity. Statistical properties of ε_θ, including its time average $\overline{\varepsilon}_\theta$, have served as indicators of the scalar fine structure and have been used extensively in the modelling of turbulent mixing. In particular, the PDF of ε_θ is an indicator of the internal scalar intermittency, with rare events occurring with values $|\varepsilon_\theta - \overline{\varepsilon}_\theta| >> \varepsilon'_\theta$; for example, Ferchichi & Tavoularis (2002) showed that the tail of this PDF (estimated from measurements of $\varepsilon_{\theta 1}$) in a moderate Reynolds number USF with UTG extended to values with $|\varepsilon_\theta - \overline{\varepsilon}_\theta| > 25\varepsilon'_\theta$. The scalar dissipation PDF is commonly assumed to be log-normal (Gurvich & Yaglom 1967), as, for example, in large-eddy simulations of combustion problems (*e.g.*, Bushe & Steiner

(1999)). However, both experimental and numerical evidence suggests that the scalar dissipation PDF departs from log-normality. Plots of this PDF in linear axes (Eswaran & Pope 1988; Jayesh & Warhaft 1992; Schumacher & Sreenivasan 2005) reveal that the log-normal approximation is not good for low values of ε_θ, whereas plots in logarithmic axes show that the tails of the PDF also depart from log-normality (Su & Clemens 2003; Schumacher & Sreenivasan 2005; Markides & Mastorakos 2008; Sutton & Driscoll 2013). Analysis by Holzer & Siggia (1994) of a scalar field embedded in a 2-D synthetic Gaussian velocity field suggested a distribution for the tail of the PDF of ε_θ in the form $(C_2/\varepsilon_\theta^{1/2})exp(-C_3\varepsilon_\theta^{\alpha_2})$ where C_2 and C_3 are constants and $\alpha_2 = \alpha_1/2$. Ould-Rouis *et al.* (1995) determined experimentally that $\alpha_2 = 0.75$ in a heated boundary layer. Chertkov *et al.* (1998) derived analytically a similar relationship for scalar advection in "smooth and white-in-time flow" (Sreenivasan & Schumacher 2010) with an infinitely large Péclet number and found that $\alpha_2 = 0.33$. Finally, Schumacher & Sreenivasan (2005) reported a value $\alpha_2 = 0.43$ in a DNS at low Re_λ and a scalar with a Schmidt number of 32.

The corresponding statistical properties of the three components $\varepsilon_{\theta\alpha}, \alpha = 1, 2, 3$ of the scalar dissipation rate would be identical only for a perfectly isotropic scalar field, a condition that has never been met in practice. Thus, measurements of the statistics of ε_θ would, in principle, require simultaneously measurements of all its three components. So far, very few authors have reported such simultaneous measurements (Sreenivasan *et al.* 1977; Antonia *et al.* 1986a; Anselmet *et al.* 1994). As a consequence, comparisons of the characteristics of measured scalar dissipation rate components have not been reported widely.

The conditional expectation $\overline{\varepsilon_\theta \mid \theta}$ appears in a diffusion term of the scalar PDF transport equation (Pope 1985). This term is usually modelled by so-called mixing models, which account for the effects of molecular diffusion. The simplest approximation of $\overline{\varepsilon_\theta \mid \theta}$ is to assume that $\overline{\varepsilon_\theta \mid \theta} = \bar{\varepsilon}_\theta$, which means that ε_θ would be independent of θ, or, in other words, that the fine structure of the scalar field would be universal and independent of large-scale features (Ching 1993; Kailasnath *et al.* 1993). Due to the scarcity of direct measurements of this property, the available information on the shape of conditional scalar dissipation rates has mostly been based on surrogate measurements of one or two of its parts. The existing literature on the shapes of $\overline{\varepsilon_\theta \mid \theta}$ and its three parts is contradictory. In GT with a UTG, $\overline{\varepsilon_{\theta 1} \mid \theta}$ was found to be $\cup$-shape behind a conventional grid (Jayesh & Warhaft 1992) but ∩-shape behind an active grid (Mydlarski 2003). These two shapes have been associated with super- and sub-Gaussian scalar PDF (Jayesh & Warhaft 1992; Ching 1993; Mydlarski 2003). In a USF with a UTG (Ferchichi & Tavoularis 2002), $\overline{\varepsilon_{\theta 1} \mid \theta}$ was nearly uniform except for its two tails. In the wake of a heated cylinder (Kailasnath *et al.* 1993), $\overline{\varepsilon_{\theta 1} \mid \theta}$ was ∪-shape and diminished at negative fluctuations, thus resulting in a lobe shape on the cold side. In a jet of a fluorescent dye mixture (Kailasnath *et al.* 1993), the streamwise and transverse parts of the conditional dissipation rate had similar shapes and the authors argued that the shape of the total conditional expectation was the same as those of its parts.

Anselmet *et al.* (1994) presented measurements of $\overline{\varepsilon_{\theta 1} \mid \theta}$ and $\overline{\varepsilon_{\theta 2} \mid \theta}$ in a heated boundary layer. At an intermediate distance from the wall ($y^+ = 60$), both properties were found to be nearly uniform for both positive and negative temperature fluctuations. However, close to the wall ($y^+ = 3$), the temperature PDF was asymmetrical and these conditional expectations depended on θ: $\overline{\varepsilon_{\theta 1} \mid \theta}$ retained low values for positive θ but had much larger values for negative θ, whereas $\overline{\varepsilon_{\theta 2} \mid \theta}$ was nearly uniform for large positive and negative θ and decreased at lower $|\theta|$, reaching a minimum near zero. Without showing results, these authors noted that measurements of conditional scalar dissipation in a heated round jet agreed qualitatively with those in the heated boundary layer. Mi *et al.* (1995) measured all three parts of $\overline{\varepsilon_\theta \mid \theta}$, although not simultaneously, in a slightly heated round jet; they found that local anisotropy was weaker near the jet axis and that all three parts of $\overline{\varepsilon_\theta \mid \theta}$ were ∪-shape. Germaine *et al.* (2014) measured all three parts of $\overline{\varepsilon_\theta \mid \theta}$, also not simultaneously, in a two-dimensional PLS in a fully developed channel flow. Far downstream of the source, the scalar PDF was found to be quasi-Gaussian, but the shapes of the three parts of $\overline{\varepsilon_\theta \mid \theta}$ depended on the transverse location. Close to the wall, all three parts $\overline{\varepsilon_{\theta i} \mid \theta}$ increased with increasing θ for large positive values of the latter. In the centre of the channel, however, the streamwise component was ∩-shaped with a peak at $\theta/\theta' \approx 2$, whereas the two other components had shapes similar to the streamwise part on the negative fluctuation side but showed no clear trend on the positive side.

A deeper understanding of the dependence (or not) of ε_θ upon θ can be achieved by investigating the JPDF $P(\theta, \varepsilon_\theta)$ of these properties. Anselmet *et al.* (1994) presented such JPDF measurements in a heated boundary layer and a heated round jet and concluded that, in regions with a symmetric temperature PDF, the assumption of independence between the scalar and its dissipation would be fully justified; they suggested that the main parameter influencing this JPDF would be the asymmetry of the scalar fluctuations and, to a lesser degree, the asymmetry of the temperature derivative. Mi *et al.* (1995) compared isocontours of $P(\theta, \varepsilon_{\theta 2})$ in a heated round jet with the corresponding isocontours of the product $P(\theta)P(\varepsilon_{\theta 2})$ of the marginal PDF; they concluded that the dependence of the two parameters was weak in their experiment. Ferchichi & Tavoularis (2002) demonstrated that, in USF with a UTG, isocontours of $P(\theta, \varepsilon_{\theta 1})$ essentially collapsed on the contours of the product $P(\theta)P(\varepsilon_{\theta 1})$, which supported their conclusion that the scalar and its dissipation rate were independent.

In summary, measurements of scalar dissipation rate statistics have been conducted in several types of turbulent flows, including grid generated turbulence, USF, boundary layers, wakes and jets. Some of these flows were complicated by inhomogeneity of the turbulence and external intermittency, as well as inhomogeneity of the scalar field, which may have introduced strong asymmetries in the PDF of the scalar and its derivatives. The effects of such factors, as well as possible effects of measurement resolution, noise and turbulent Reynolds number, are difficult to separate, as different experiments have been conducted under different conditions and using different experimental procedures. The present study is an attempt to resolve some of the lingering questions on the scalar fine structure by measuring directly the scalar dissipation rate and other fine structure indicators in three different scalar fields superimposed on the same homogeneous turbulence.

3. Apparatus and instrumentation

As the facility and instrumentation have been described in Part 1, only details that are essential for Part 2 will be presented in this section. All experiments were conducted in an open loop wind tunnel, having a test section that had a height of h=0.305 m, a width of 1.50h and a length of 16.6h. Uniform mean shear was generated by a shear generator, which was followed by a flow separator, consisting of an array of parallel plates spaced by $M = 25.4$ mm to straighten the flow and impose initial uniformity of length scales. An array of electric heating ribbons was inserted in the fully developed flow (at $x_1/h = 4.5$) to generate passively the desired scalar field. A three-wire probe consisting of a cross-wire and a cold-wire (see Part 1) was used for simultaneous velocity and temperature measurements. The separations between neighbouring sensor planes were 0.5 mm. The velocity sensors were tungsten wires with a diameter $d = 2.5$ μm and a length to diameter ratio $l/d = 340$, and operated at a constant temperature with an overheat ratio of 1.5. The cold-wire sensor was made of 90%Pt-10%Rh and had $d = 0.63$ μm and $l/d \approx 950$. A second probe, consisting of two orthogonal pairs of parallel cold-wires, was used to measure simultaneously the three temperature derivatives. The sensors in this probe had $d = 0.63$ μm and $l/d = 635$ (those used for measuring the spanwise derivative) and 730 (those used for measuring the transverse derivative); the corresponding sensor separation distances were 0.66 and 0.60 mm, respectively. It is well-known that end conduction would introduce error for cold-wires with $l/d < 1500$ (Browne & Antonia 1987). However, tests similar to those done by Mydlarski & Warhaft (1998) showed that the dominant source of error for the derivative of temperature fluctuations in our measurements was the spatial resolution, and not end conduction effects (Behnamian 2015). The typical value of η_θ for our flows was about 0.3 mm, yielding $l/\eta_\theta = 1.3$ and 1.5 for the two pairs of parallel cold-wires. The results of Wyngaard (1971) showed that our temperature measurements with parallel cold-wires would resolve up to 95% of the scalar dissipation rate. The streamwise temperature derivative was calculated using Taylor's "frozen flow" approximation.

The operational amplifiers used in the cold-wire circuits provided r.m.s. signal to noise ratios that were higher than 50 in all long-run measurements so that the noise effect on the measurement of temperature was entirely negligible and no correction was deemed to be necessary for the calculation of the temperature variance. To keep errors in measurements of the spatial temperature derivatives as low as possible, all sensors of the four-wire probe were inspected under a microscope for straightness and parallel positioning prior to the experiments. It was verified that the spectra of temperatures measured by the two sensors of each pair essentially coincided and so did the spectra of the temporal derivatives of the temperature measured by the two sensors of each pair. To evaluate the effect of electronic noise, velocity sensitivity of cold-wire sensors and other undesirable influences on the measurements of spatial velocity derivatives, we compared measurements of the temperature derivatives in the unheated and heated flows. The mean square value in the unheated flow was subtracted from the corresponding value in the heated flow to provide a noise-corrected value, under the assumption that "noise" and temperature fluctuations were uncorrelated. Some typical examples of the magnitude of these corrections are as follows. The values of rms temperature derivatives $\sqrt{\overline{(\partial\theta/\partial x_\alpha)^2}}$ were typically 3.5 K/m in unheated flows or unheated regions of the three scalar fields. The ratios of the rms temperature derivatives at the centre of the TML to corresponding values in the unheated flow were about 43, so the noise-correction in this case was less than 0.1% and could be neglected. The same ratios were approximately 6 at a position in the TML where the temperature rise was about 0.1 K; in this case, the corrected mean square temperature derivatives were 3% lower than the uncorrected values.

The effect of wire spacing Δ on the accuracy of temperature derivatives measured by parallel sensors has been studied by several investigators. Antonia & Mi (1993) showed that this effect on $\overline{(\partial\theta/\partial x_\alpha)^2}$ would be negligible for $\Delta/\eta < 3$. Tong & Warhaft (1994) showed that for $1 < \Delta/\eta < 3$ the shapes of the PDF of derivatives and their their skewnesses and kurtoses were insensitive to Δ, but for $\Delta/\eta \geqslant 3$ the skewness and kurtosis tend to diminish with increasing Δ. The values of Δ/η for our four-wire probe were 2.4 and 2.6. To test the consistency between temperature derivatives measured by the two pairs, we compared measurements at the centre of the TML taken with the probe in one orientation and those taken with the same probe rolled by 90° about its streamwise axis. The PDF of scalar derivatives $\partial\theta/\partial x_\alpha$ measured by the two wire pairs essentially coincided. The temperature derivative variances measured by the two pairs of sensors were within 2% of each other; such precision is well within the measurement uncertainty of the sensor spacing, determined with the use of the microscope. During the same tests, the correlations between the temperature and its first derivatives in the transverse and spanwise directions were also found to be the same for the two pairs. These results demonstrate that there was no significant qualitative difference between the assumed and the actual probe geometries and that the ratio of spacings of the two wire pairs was represented accurately by the value of 1.1 used.

The cold-wire sensors were operated at a current of 0.15 mA. The hot- and cold-wire signals were low pass filtered at 10.4 and 8 kHz, respectively, and sampled simultaneously at a rate of 22 kHz. As in Part 1, before being processed, the time series were filtered digitally using a double-pass, seventh-order, Butterworth, low-pass filter, with a cut-off frequency that was adjusted at each location to the local Kolmogorov frequency $f_k = \overline{U}_1/(2\pi\eta)$. Time series consisting of 5.5×10^5 samples were recorded for calculating time-averaged profiles, whereas longer ones, consisting of 1.1×10^8 samples, were recorded separately for calculating the main PDF and conditional expectations of interest. Each of the latter time series extended over 83 min and was divided into 2.5×10^3 segments.

4. Results

4.1. *General properties of the scalar fields*

The characteristics of the USF and the three scalar fields (UTG, TML, and PLS) in this study were thoroughly documented in Part 1 and only necessary details are provided here. Downstream of the heating screen, the turbulence was fully developed and nearly homogeneous on transverse planes. The turbulent kinetic energy increased at an approximately exponential rate and the streamwise integral length scale evolution could also be fitted by an exponential expression. In the UTG, the non-uniformities of transverse profiles of normalized temperature fluctuations and the turbulent heat flux coefficients were sufficiently small for the scalar field to be considered as nearly homogeneous. The temperature variance grew at the same rate as the turbulent kinetic energy. The TML was generated by heating the upper half of the flow so that its mean temperature rise was $\Delta\overline{T}_h = 2.00$ K. The mean isotherms of the field evolved linearly in the streamwise direction. The TML penetrated deeper into the low-velocity side of the USF than the high-velocity side; however, the distance of the 50% isotherm from the wind tunnel centreline, denoted as x_{20}, was nearly zero in the range $5 \leqslant x_1/h \leqslant 10$. The PLS was generated by heating a pair of ribbons located on the centreline. Similar to the TML, the mean isotherms evolved linearly in the streamwise direction but with slightly higher slopes than those in the TML. The heated fluid penetrated deeper into the low-velocity side than the high-velocity side and the locus of the peak mean temperature rise $\Delta\overline{T}_m$ (also denoted as x_{20}) shifted towards the lower velocity region linearly in the range $5 \leqslant x_1/h \leqslant 10$. Figure 1 shows representative transverse profiles of the mean temperature rise $\Delta\overline{T}$ (normalized by the corresponding maximum $\Delta\overline{T}_h$ or $\Delta\overline{T}_m$), respectively, the temperature standard deviation θ' (normalized by the corresponding value θ'_c in the "centre" of the scalar field) and the turbulent heat flux correlation coefficients for the two inhomogeneous scalar fields at x_1/h=10. The profile of the mean temperature rise in the TML could be fitted by an error function and the one in the PLS could be fitted by a Gaussian function. Although the mean profiles of the TML and the PLS were very

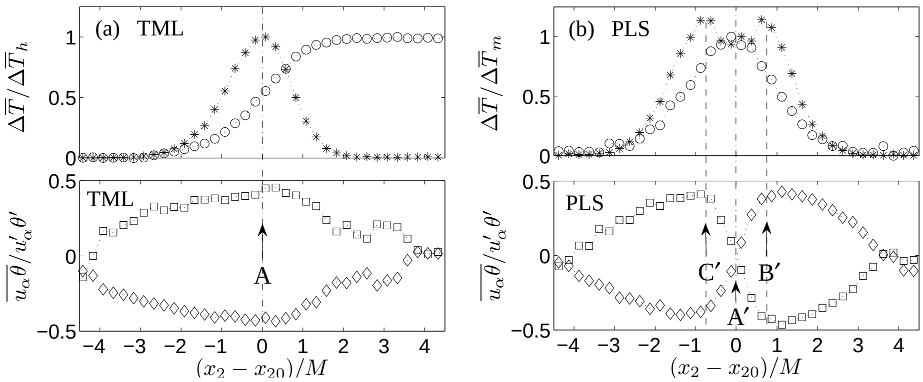

Figure 1: Time-averaged transverse profiles across (a) the TML and (b) the PLS; $x_1/h = 10$; ∘: non-dimensionalized mean temperature; ∗: θ'/θ'_c; □: $\overline{u_1\theta}/(u'_1\theta')$ and ⋄: $\overline{u_2\theta}/(u'_2\theta')$; dash-dot lines represent the centres of the scalar fields (A and A′, respectively); dashed lines show the locations of points B′ and C′ in the PLS.

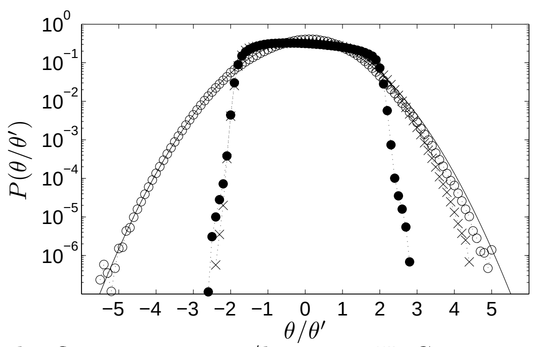

Figure 2: PDF of scalar fluctuations at $x_1/h = 10$; ∘: UTG, x_2=0; •: TML, point A; ×: PLS, point C′; solid line represents Gaussian PDF.

different, both scalar fields had maximum fluctuation levels at locations that essentially coincided with inflection points in the corresponding mean profiles and roughly maxima or minima in the turbulent heat flux profiles (point A in the TML and points B′ and C′ in the PLS). Consequently, the TML had a nearly Gaussian, single-peak θ' profile, whereas the PLS had two peaks of θ' and a minimum at its centre (point A′), where the mean temperature rise was maximum and the turbulent heat fluxes vanished. As shown in Part 1, no fluid from the unheated stream (or the high-temperature stream for the TML) reached any of these points.

The PDF of the scalar fluctuations at selected locations in the three scalar fields are shown together in figure 2. The scalar PDF was essentially Gaussian in the UTG, but distinctly non-Gaussian in the TML and the PLS. In the TML centre, the PDF appeared to be symmetric and sub-Gaussian with both tails bounded. At point C′ of the PLS, the scalar PDF was asymmetric: it had a nearly Gaussian tail on the warm side, and it was sub-Gaussian with a bounded tail on the cold side. The similarity between the cold tails of the PDF in the TML and the PLS is consistent with the similarity between the cold sections of the two mean temperature rise profiles. On the other hand, the apparent similarity between the warm tails of the PDF in the PLS and the UTG field is merely coincidental. Although Gaussianity is the consequence of scalar transport along the UTG, near-Gaussianity in the PLS warm side is attributed to sustained temperature fluctuations introduced by the heating source.

4.2. *PDF of scalar derivatives*

The PDF of the three scalar derivatives in the streamwise, transverse, and spanwise directions at $x_1/h = 10$ and selected transverse locations are shown in figure 3. A general observation is that the negative tail of the PDF of the streamwise derivative was more flared than the positive one, whereas the opposite can be said for the PDF of the transverse derivative; the tails of the spanwise derivative PDF appeared to be roughly symmetric.

Attempts were made to fit both tails of all PDF with exponential functions (Holzer & Siggia 1994), albeit with different coefficients for each tail for cases with large PDF skewnesses. All positive tails of the streamwise derivative PDF could be fitted well by the same function, having coefficients $C_1 = 0.85 \pm 0.03$ and $\alpha_1 = 1.99 \pm 0.11$. The negative tail for the UTG field was also nearly exponential, with coefficients $C_1 = 0.77$ and $\alpha_1 = 1.90$, in agreement with the results of Ferchichi & Tavoularis (2002). In the TML and the PLS, the negative tails had a roll-down shape at large fluctuations that made the fitting unsatisfactory. Such roll-down shapes have been previously observed by Holzer & Siggia (1994). Analogous observations can be made for the tails of the transverse derivative PDF. All negative tails of these PDF could be fitted by the same exponential function with $C_1 = 0.85 \pm 0.03$ and $\alpha_1 = 2.0 \pm 0.1$. The positive tail was exponential with coefficients 0.87 and 2.0, respectively, in the UTG, but had roll-down shapes in the TML and the PLS. Both tails of the spanwise derivative PDF for all three scalar fields had roll-down shapes (see also Germaine *et al.* 2014).

The skewness and flatness factors of the three temperature derivatives at selected locations are listed in table 1. The presently measured skewnesses were generally in conformity

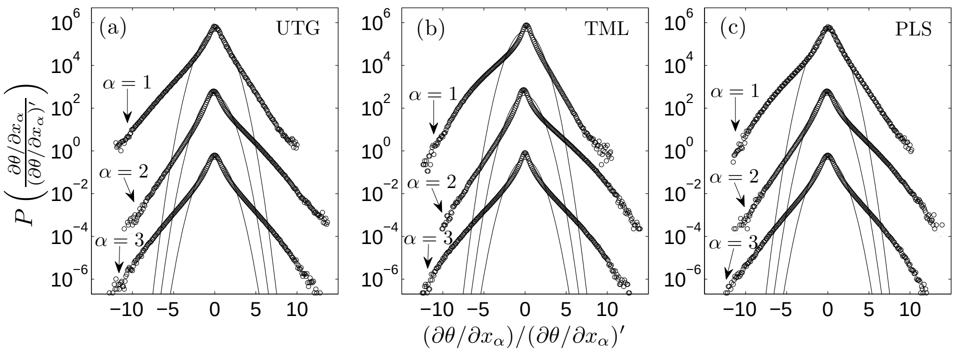

Figure 3: PDF of scalar derivatives normalized by the corresponding standard deviation in (a) the UTG, $x_2 = 0$, (b) the TML, centre, and (c) the PLS, point C′, at $x_1/h = 10$; within each plot the top (multiplied by 10^6), middle (multiplied by 10^3) and bottom sets of data correspond to the streamwise ($\alpha = 1$), transverse ($\alpha = 2$) and spanwise ($\alpha = 3$) derivatives; solid lines show Gaussian PDF; Greek indices are not summed.

	Skewness				Flatness			
Scalar field	UTG	TML	PLS	PLS	UTG	TML	PLS	PLS
Location	$x_2 = 0$	A	C′	A′	$x_2 = 0$	A	C′	A′
$\partial\theta/\partial x_1$	-0.91	-0.94	-0.71	-0.21	14.8	16.0	13.9	10.7
$\partial\theta/\partial x_2$	1.45	1.56	1.22	0.25	11.2	11.5	10.2	9.3
$\partial\theta/\partial x_3$	0.08	0.07	0.10	0.03	10.9	10.7	9.8	9.0

Table 1: Skewness and flatness factors of the scalar derivatives ($x_1/h = 10$).

with the qualitative models of Sreenivasan & Tavoularis (1980) and Tavoularis & Corrsin (1981b). The streamwise and transverse derivatives had significant negative and positive, respectively, skewnesses at all locations where the mean scalar gradient was strong, and much lower skewness magnitudes in the PLS centre, where the mean scalar gradient vanished. The spanwise derivative skewnesses were universally negligible, as a consequence of the spanwise statistical symmetry of all scalar fields. The streamwise derivative skewnesses were comparable to the asymptotic value suggested by Sreenivasan & Tavoularis (1980) and the transverse derivative skewnesses had magnitudes that were consistently about 50% higher in agreement with the measurements of Ferchichi & Tavoularis (2002). A possible explanation for the difference in magnitude of the two skewnesses is that, for a transverse mean temperature gradient, the very large and rare temperature excursions (cliffs) would be more prevalent in the transverse direction than in the streamwise direc-

	Skewness			Flatness		
Scalar field	UTG	TML	PLS	UTG	TML	PLS
Location	$x_2 = 0$	A	C′	$x_2 = 0$	A	C′
	-0.03	-0.03	-0.04	3.2	3.1	3.2

Table 2: Skewness and flatness factors of the logarithm of the PDF of the scalar dissipation rate at selected points in the three scalar fields.

tion (Tong & Warhaft 1994); we were not able to test this hypothesis as we could not obtain instantaneous temperature traces in the transverse direction.

It is worth noting that the scalar derivative skewness magnitudes tended to rise to large values toward the edges of the TML and the PLS; for example, the streamwise derivative skewness at $(x_2 - x_{20})/M = -1.2$ in the TML and at $(x_2 - x_{20})/M = -1.6$ in the PLS was -1.2, whereas the transverse derivative skewness at the same locations was 2.7. Because scalar fluctuations near the edges of these fields were affected strongly by large–scale scalar intermittency, we will not consider these results in the present discussion.

All flatnesses were much higher than the Gaussian value of 3, pointing to the strong intermittent character of the scalar field in all directions. The flatnesses of the streamwise scalar derivatives were consistently about 30% larger than those of the transverse and spanwise derivatives, which were roughly equal. These observations are consistent with previous scalar experiments in shear flows (Sreenivasan & Antonia 1997; Sreenivasan *et al.* 1977; Tavoularis & Corrsin 1981b; Antonia *et al.* 1986a; Mi *et al.* 1995; Ferchichi & Tavoularis 2002).

4.3. *PDF of the scalar dissipation rate*

Figure 4 shows the PDF of the measured scalar dissipation rate and its logarithm in standardised form. The plots include data from all three scalar fields, at locations having strong mean scalar gradients. Differences among values in the three fields were relatively small in much of the PDF; the largest difference was in the negative tail of the PDF of $\log \varepsilon_\theta$, where the values in the PLS were larger than those in the two other fields.

All fields exhibited strong internal intermittency, as demonstrated by the fact that they all had large fluctuations of ε_θ, with values that could reach up to 40 times the corresponding standard deviations. All data in the PDF tails were bounded by two exponential functions having exponents $\alpha_2 = 0.64$ and 0.68. (Holzer & Siggia 1994; Chertkov

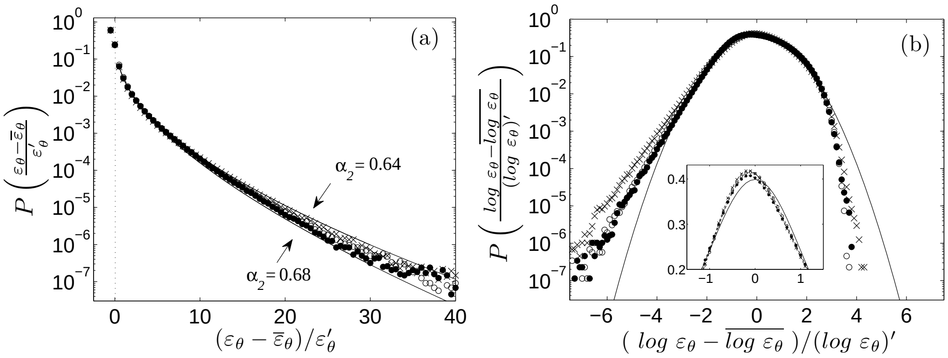

Figure 4: Standardised PDF of the normalized scalar dissipation rate (a) and its logarithm (b) in the three scalar fields, at points having strong mean scalar gradients (symbols as in figure 2). Solid lines in the left plot represent two exponential fits to the PDF tail and the solid line in the right plot represents a Gaussian function.

et al. 1998). The PDF of the standardized logarithm of the scalar dissipation rate at the points of concern in the three scalar fields were visibly non-Gaussian, despite the fact that the corresponding skewness and flatness factors, listed in table 2, were not very different from the Gaussian values. Deviations from log-normality could be observed both in the cores (see insert in figure 4a) and the tails of all PDF, in conformity with previous studies. In particular, the high-dissipation tails were sub-log-normal, whereas the low-dissipation tails were flared, a fact that is consistent with the small negative skewness of these PDF. Such deviations from a log-normal distribution, particularly the low-dissipation tails, have been attributed previously to the effects of measurement resolution, noise, low Reynolds number and the presence of unmixed scalar field, which would tend to increase the population of low ε_θ values. Su & Clemens (2003) showed that the PDF of the scalar dissipation rate could become closer to the log-normal PDF by an improvement of measurement resolution or an increase in Re_λ. We have presently observed that very low dissipation values were more frequent at point C′ of the PLS than in the UTG and TML fields. This difference cannot be caused by effects of measurement resolution or turbulent Reynolds number, which were the same (or very close) for all three scalar fields. It may be explained, however, by the presence of high-temperature unmixed scalar patches originating in the source of the PLS (see Part 1); such patches of unmixed scalar were not present in the two other fields, in which scalar fluctuations were produced by the mean scalar gradient. Lepore & Mydlarski (2012) investigated the influence of the turbulent Péclet number Pe (defined as $u'_1 L_{\theta\theta,1}/\gamma$, where $L_{\theta\theta,1}$ is the

Scalar field	UTG	TML	PLS
Location	$x_2 = 0$	A	C′
$\overline{\varepsilon}_{\theta 1}/\overline{\varepsilon}_\theta$	0.22	0.22	0.20
$\overline{\varepsilon}_{\theta 2}/\overline{\varepsilon}_\theta$	0.395	0.48	0.46
$\overline{\varepsilon}_{\theta 3}/\overline{\varepsilon}_\theta$	0.385	0.30	0.24
$\overline{\varepsilon}_\theta$ ($\mathrm{K^2 s^{-1}}$)	0.094	0.91	0.052

Table 3: The scalar dissipation rates and the relative magnitudes of its parts at selected points in the three scalar fields.

streamwise thermal integral length scale and γ is the thermal diffusivity) on the small-scale statistics of passive scalar increments in a heated wake, in which Pe was varied by changing the initial thermal length scale of the scalar field. In the present study, the scalar integral length scale, and thus the Péclet number, varied by less than 5% in the three scalar fields at $x_1/h = 10$ (see figure 10 in part 1) and so, if there is any Pe-effect, it is not expected to be discernible.

4.4. *Conditional expectations of the scalar dissipation rate*

The variations of the conditional scalar dissipation rates and their three parts in the three scalar fields are shown in figure 5a-c, whereas the relative magnitudes of the three scalar dissipation parts are shown in figure 5d-f.

In the UTG field, all functions had relatively flat shapes and were slightly $\cap$-shape for small scalar fluctuations. The near-uniformity of $\overline{\varepsilon_\theta \mid (\theta/\theta')}/\overline{\varepsilon}_\theta = 1$ indicates an essential independence of ε_θ from θ, in agreement with the findings of Ferchichi & Tavoularis (2002). The similarity in the shapes of all scalar dissipation parts justifies the use of the streamwise part as a qualitative surrogate for the total in the UTG field. Nevertheless, the streamwise part had values that were roughly 40% lower than those of either the transverse or spanwise parts throughout the entire range of scalar fluctuations, which indicates that one should apply a correction to the locally isotropic estimate of $\overline{\varepsilon_\theta \mid (\theta/\theta')}$ from its streamwise part. The correction factor for $\overline{\varepsilon}_\theta$ was about 1.5, which is consistent with the value reported by Tavoularis & Corrsin (1981b).

In the TML, the conditional scalar dissipation and all its three parts were strongly non-uniform. Nevertheless, they all had similar shapes, as over most of the range of scalar fluctuations ($|\theta/\theta'| \leqslant 2$), they were $\cap$-shaped, but, for large scalar fluctuations, they turned locally $\cup$-shape. It is interesting to observe that the streamwise and spanwise

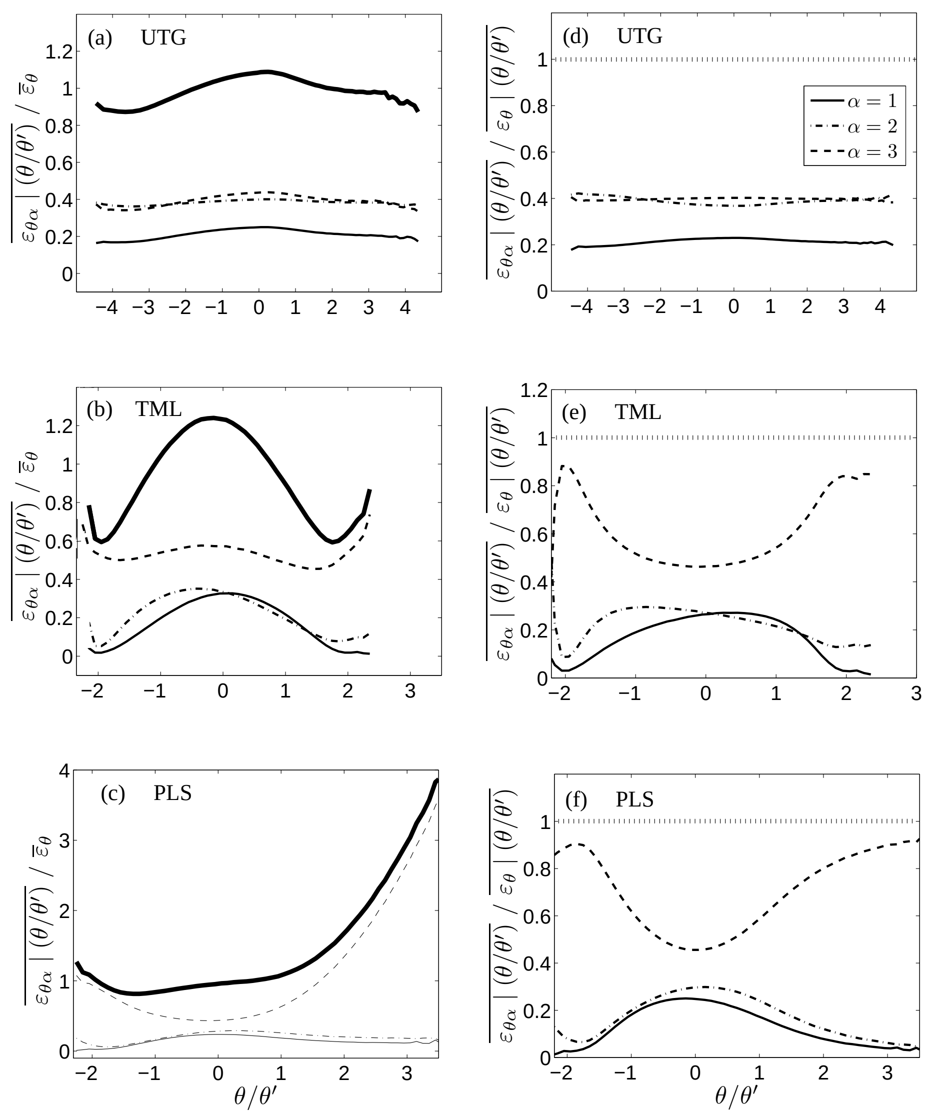

Figure 5: Conditional expectations of the scalar dissipation rate and its three parts (a-c) and relative magnitudes of the three conditional dissipation parts (d-f) in the UTG field at x_2=0, at the TML centre, and in the PLS at point C′; thick solid lines in a-c represent the total conditional expectation $\overline{\varepsilon_\theta \mid (\theta/\theta')}/\overline{\varepsilon}_\theta$; dotted lines in d-f indicate the value of 1.

parts had comparable values over the entire range of scalar fluctuations, whereas the transverse part was significantly larger. Most remarkably, for the largest θ of either sign, $\overline{\varepsilon_{\theta_1} \mid (\theta/\theta')}$ and $\overline{\varepsilon_{\theta_3} \mid (\theta/\theta')}$ were very small so that $\overline{\varepsilon_{\theta_2} \mid (\theta/\theta')}$ accounted for more than

80% of $\overline{\varepsilon_\theta \mid (\theta/\theta')}$. In summary, the conditional scalar dissipation rate in the TML was not, even very roughly, a multiple of any of its parts.

In the PLS, the differences among the conditional scalar dissipation parts were very strong, both quantitatively and qualitatively. As in the TML, the streamwise and spanwise parts had comparable values over the entire range of scalar fluctuations, being ∩-shape centrally and locally ∪-shape towards their two edges. Also in conformity with the TML results, the transverse part was much larger than either of the two other parts, especially for large θ of either sign, for which it accounted for more than 80% of the total. Unlike in the TML, however, the transverse part was strongly ∪-shape in the entire scalar range, in sharp contrast to the two other parts. The total dissipation shape was affected visibly by the former two parts in the central range, but at large scalar fluctuations it was dominated in value and shape by the transverse part. Consequently, the use of the streamwise (or any other) part as a surrogate for the total scalar dissipation rate would be grossly inappropriate for the PLS. This is in agreement with the observation of Germaine *et al.* (2014) that in a PLS in a channel flow away from the wall the shape of the streamwise part of the scalar dissipation differred from the shapes of the two other parts.

A comparison of the previous results in the three scalar fields makes it clear that the shapes of the scalar conditional expectation rate and its three parts vary widely from one field to another and so a simple representation of these properties by a universal model (Gaussian or otherwise) would be inaccurate.

4.5. *Further discussion on the dependence of the scalar dissipation rate upon the scalar value*

The conditional expectations of the scalar dissipation rates shown in the previous section indicated a weak dependence of this property upon the scalar fluctuation value for the UTG field and a strong dependence for the TML and the PLS. To further investigate this dependence in our experiments, we have plotted iso-probability contours of the JPDF $P(\theta, \varepsilon_\theta)$ and $P(\theta, \varepsilon_\alpha)$ in figure 6, together with the product of the corresponding marginal PDF. Statistical independence requires that $P(\theta, \varepsilon_\theta) = P(\theta)P(\varepsilon_\theta)$, with similar equalities also applying to the three scalar dissipation parts. Another feature of interest in these JPDF is their degree of asymmetry with respect to scalar fluctuations. This can be quantified by a comparison of the correlation coefficients $\overline{\theta\varepsilon_\theta}/(\theta'\varepsilon'_\theta)$ for positive and negative θ. Although an equality of the values of these coefficients is not proof of JPDF

	$\overline{\theta\varepsilon_{\theta 1}}/(\theta'\varepsilon'_{\theta 1})$		$\overline{\theta\varepsilon_{\theta 2}}/(\theta'\varepsilon'_{\theta 2})$		$\overline{\theta\varepsilon_{\theta 3}}/(\theta'\varepsilon'_{\theta 3})$		$\overline{\theta\varepsilon_{\theta}}/(\theta'\varepsilon'_{\theta})$		$\overline{\theta\varepsilon_{\theta}}/(\theta'\varepsilon'_{\theta})$
	$\theta < 0$	$\theta > 0$	$\theta < 0$	$\theta > 0$	$\theta < 0$	$\theta > 0$	$\theta < 0$	$\theta > 0$	θ
UTG, $x_2 = 0$	-0.153	0.109	-0.197	0.176	-0.147	0.102	-0.226	0.195	-0.031
TML centre	-0.097	0.095	-0.181	0.166	-0.128	0.083	-0.198	0.173	-0.025
PLS, point C′	-0.098	0.140	-0.120	0.191	-0.091	0.156	-0.149	0.234	0.085

Table 4: Correlation coefficients between the scalar value and the scalar dissipation rate.

symmetry or of statistical independence between ε_θ and θ, their inequality may reveal some features of the scalar field structure. The values of these correlation coefficients and the total correlation coefficients in the three scalar fields are presented in table 4.

In the UTG field, the JPDF iso-contours followed closely the corresponding iso-contours of the marginal PDF products. This is consistent with the previously demonstrated near-Gaussianity of the scalar field, which is a necessary and sufficient condition for statistical independence between ε_θ and θ (Ching 1993; Ferchichi & Tavoularis 2002). Nevertheless, all JPDF showed small asymmetries, in conformity with the observed skewness of the dissipation distribution, the correlation coefficients in table 4 and the results by Ferchichi & Tavoularis (2002).

In both the TML and the PLS, the significant qualitative and quantitative differences between the iso-contours of the JPDF and the marginal PDF products provided further evidence for the strong dependence of ε_θ upon θ. In both fields, the JPDF value was larger than the marginal PDF product value for a range of small (positive or negative) scalar fluctuations and the order was reversed for relatively large scalar fluctuations. All contours were somewhat asymmetric in the TML (less so for the streamwise scalar dissipation part) and strongly asymmetric in the PLS, in conformity with our previous observations.

In summary, our observations demonstrate conclusively that the scalar dissipation rate in inhomogeneous scalar fields depends strongly on the scalar value and that this dependence is not universal but particular to each field and also depends on the location within the field. Moreover, we have also demonstrated that a zero scalar skewness or a symmetry in the scalar PDF does not necessarily imply statistical independence of the fine and large scalar structures; this result contradicts the suggestion of Anselmet *et al.* (1994).

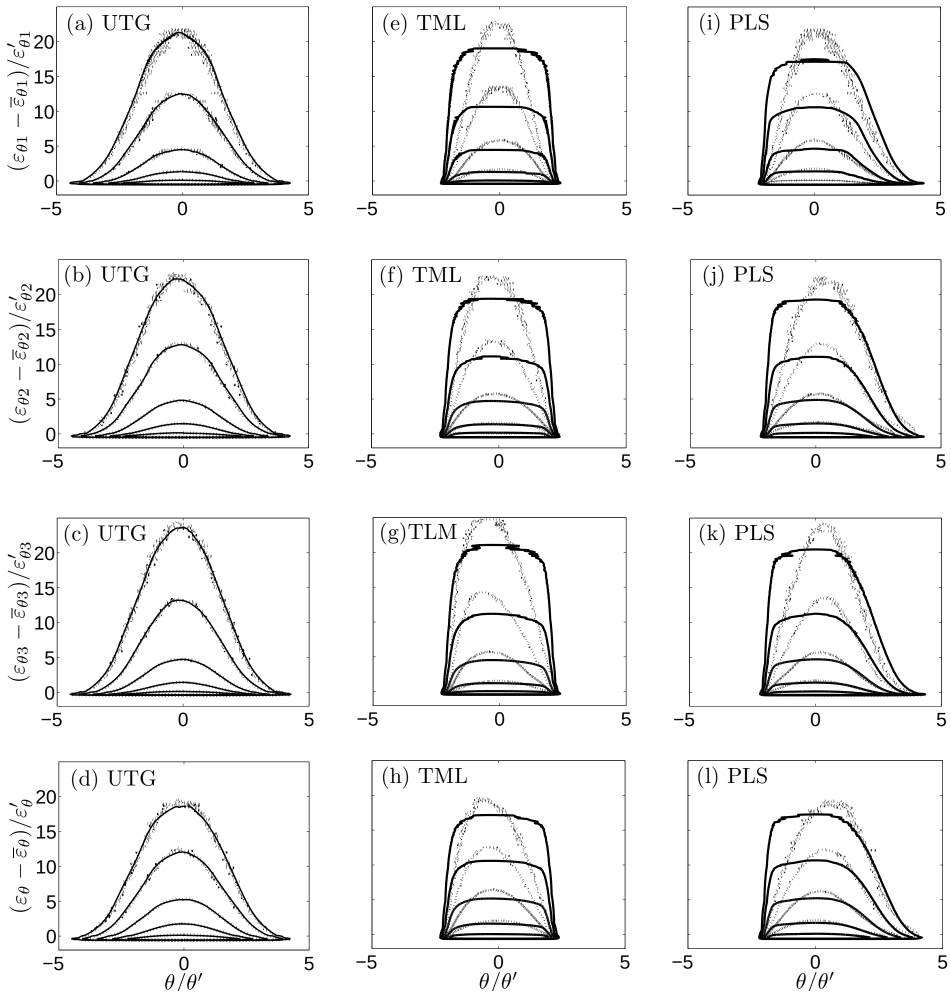

Figure 6: Comparison of iso-contours of JPDF of the scalar fluctuations and the scalar dissipation rates (scattered dots) and iso-contours of the products of the corresponding marginal PDF (solid lines) in the UTG at $x_2 = 0$, the TML centre and the PLS, point C′; iso-contour values from the outer one to the inner one are 0.00001, 0.0001, 0.001, 0.01 and 0.1.

5. Conclusions

In this article, we have reported simultaneous measurements of the three scalar derivatives in three different scalar fields in nearly homogeneous, sheared turbulence. The fine structures of these scalar fields were compared at locations that were not subjected to external intermittency. The PDF of the logarithm of the scalar dissipation rate departed clearly from log-normality in all three scalar fields: the high–dissipation tails were sub-log-normal, whereas the low–dissipation tails were flared. The low-dissipation values in a thermal plume that contained the remnants of thermal patches introduced at the source were higher than those in a homogeneous scalar field and in a thermal mixing layer. Analysis of conditional scalar dissipation results in our study revealed that the use of a single part of the scalar dissipation rate as a surrogate for the total would be appropriate for a homogeneous scalar field but quite inappropriate for inhomogeneous ones, in which the dependence of this conditional expectation on the scalar fluctuation value would be specific to each field. Finally, comparison between the JPDF of the scalar and its dissipation rate and isocontours of the products of the corresponding marginal PDF showed that these properties were approximately independent from each other in the homogeneous scalar field, but dependent in the inhomogeneous fields, irrespectively of the degree of symmetry of the scalar PDF.

Acknowledgement

Financial support by the Natural Sciences and Engineering Research Council of Canada (NSERC) is gratefully acknowledged. We thank Professor Petar Vukoslavčević for constructing our hot- and cold-wire probes.

REFERENCES

Anselmet, F., Djeridi, H. & Fulachier, L. 1994 Joint statistics of a passive scalar and its dissipation in turbulent flows. *J. Fluid Mech.* **280**, 173–197.

Antonia, R. A., Anselmet, F. & Chambers, A. J. 1986a Assessment of local isotropy using measurements in a turbulent plane jet. *J. Fluid Mech.* **163**, 365–391.

Antonia, R. A. & Mi, J. 1993 Temperature dissipation in a turbulent round jet. *J. Fluid Mech.* **250,**, 531–551.

Behnamian, A. & Tavoularis, S. 2015 Measurements of scalar probability density functions and velocity conditional expectations in uniformly sheared turbulence. *In preparation for submission to the J. Fluid Mech.* .

Browne, L. W. B. & Antonia, R. A. 1987 The effect of wire length on temperature statistics in a turbulent wake. *Exps. Fluids* **5**, 426–428.

Bushe, W. K. & Steiner, H. 1999 Conditional moment closure for large eddy simulation of nonpremixed turbulent reacting flows. *Phys. Fluids* **11(7)**, 1896–1906.

Chertkov, M., Falkovich, G. & Kolokolov, I. 1998 Intermittent dissipation of a passive scalar in turbulence. *Phys. Rev. Lett.* **80**, 2121–2124.

Ching, E. S. C. 1991 Probabilities for temperature differences in rayleigh-benard convection. *Phys. Rev. A* **44 (6)**, 3622–3629.

Ching, E. S. C. 1993 Probability densities of turbulent temperature fluctuations. *Phys. Rev. Lett.* **70**, 283286.

Corrsin, S. 1951 On the spectrum of isotropic temperature fluctuations in isotropic turbulence. *J. Appl. Phys.* **22**, 46973.

Eswaran, V. & Pope, S. B. 1988 Direct numerical simulations of the turbulent mixing of a passive scalar. *Phys. Fluids* **31**, 506.

Ferchichi, M. & Tavoularis, S. 2002 Scalar probability density function and fine structure in uniformly sheared turbulence. *J. Fluid Mech.* **461**, 155–182.

Germaine, E., Mydlarski, L. & Cortelezzi, L. 2014 Evolution of the scalar dissipation rate downstream of a concentrated line source in turbulent channel flow. *J. Fluid Mech.* **749**, 227–274.

Gurvich, A. S. & Yaglom, A. M. 1967 Breakdown of eddies and probability distributions for small-scale turbulence, boundary layers and turbulence. 10, s5w5. *Phys. Fluids Suppl.* **10**, 59–65.

Holzer, M. & Siggia, E. D. 1994 Turbulent mixing of a passive scalar. *Phys. Fluids* **6**, 1820–1837.

Jayesh & Warhaft, Z. 1992 Probability distribution, conditional dissipation, and transport of passive temperature fluctuations in grid-generated turbulence. *Phys. Fluids* **4**, 2292–2307.

Kailasnath, P., Sreenivasan, K. R. & Saylor, J. R. 1993 Conditional scalar dissipation rates in turbulent wakes, jets, and boundary layers. *Phys. Fluids* **5 (12)**, 3207–3215.

Kolmogorov, A. 1941 The local structure of turbulence in incompressible viscous fluid for very large reynolds' numbers. *Dokl. Akad. Nauk. SSSR* **30**, 301–305.

Lepore, J. & Mydlarski, L. 2012 Finite-pclet-number effects on the scaling exponents of high-order passive scalar structure functions. *J. Fluid Mech.* **713**, 453–481.

Markides, C. N. & Mastorakos, E. 2008 Measurements of the statistical distribution of the scalar dissipation rate in turbulent axisymmetric plumes. *Flow Turbul.Combust.* **81**, 221–234.

Mi, J., Antonia, R. A. & Anselmet, F. 1995 Joint statistics between temperature and its dissipation rate components in a round jet. *Phys. Fluids* **7**, 1665–1673.

Mydlarski, L. 2003 Mixed velocity–passive scalar statistics in high-Reynolds-number turbulence. *J. Fluid Mech.* **475**, 173–203.

Mydlarski, L. & Warhaft, Z. 1998 Passive scalar statistics in high-Péclet-number grid turbulence. *J. Fluid Mech.* **358**, 135–175.

Obukhov, A.M. 1949 Structure of themperature field in turbulent flows. *Izv. Akad. Nauk. SSSR, Geogr. Geofiz* **13**, 58–69.

Ould-Rouis, M., Anselmet, F. & Le Gal, P. andVaienti, S. 1995 Statistics of temperature increments in fully developed turbulence part ii. experiments. *Physica D* **85**, 405–424.

Pope, S. B. 1985 Pdf methods for turbulent reactive flows. *Prog. Energy Combust. Sci.* **11**, 119–192.

Schumacher, J. & Sreenivasan, K. R. 2005 Statistics and geometry of passive scalars in turbulence. *Phys. Fluids* **17**, 125107.

Sreenivasan, K. R. 1991 On the local isotropy of the passive scalars in turbulent shear flows. *Proc. R. Soc. London. Ser. A* **241**, 165–82.

Sreenivasan, K. R. & Antonia, R. A. 1977 Skewness of the temperature derivatives in turbulent shear flows. *Phys. Fluids* **20**, 1986–1988.

Sreenivasan, K. R. & Antonia, R. A. 1997 The phenomenology of small-scale turbulence. *Annu. Rev. Fluid Mech.* **29**, 435–472.

Sreenivasan, K. R., Antonia, R. A. & Danh, H. Q. 1977 Temperature dissipation fluctuations in a turbulent boundary layer. *Phys. Fluids* **20**, 1238–1249.

Sreenivasan, K. R. & Schumacher, J. 2010 Lagrangian views on turbulent mixing of passive scalars. *Phil. Trans. R. Soc. A* **368**, 1561–1577.

Sreenivasan, K. R. & Tavoularis, S. 1980 On the skewness of the temperature derivative in turbulent flows. *J. Fluid Mech.* **101**, 783–795.

Su, L. K. & Clemens, N. T. 2003 The structure of fine-scale scalar mixing in gas-phase planar turbulent jets. *J. Fluid Mech.* **488**, 129.

Sutton, J. A. & Driscoll, J. F. 2013 Measurements and statistics of mixture fraction and scalar dissipation rates in turbulent non-premixed jet flames. *Combust. Flame* **160**, 1767–1778.

Tavoularis, S. & Corrsin, S. 1981b Experiments in nearly homogeneous turbulent shear flow with a uniform mean temperature gradient. Part 2. *J. Fluid Mech.* **104**, 349–367.

Tavoularis, S. & Sreenivasan, K. R. 1981 Skewness of the temperature derivatives in an asymmetrically heated wake. *Phys. Fluids* **24(4)**, 778–779.

Tong, C. & Warhaft, Z. 1994 On passive scalar derivative statistics in grid turbulence. *Phys. Fluids* **6**, 2165–2176.

Warhaft, Z. 2000 Passive scalars in turbulent flows. *Annu. Rev. Fluid Mech.* **32** (1), 203–240.

Wyngaard, J. C. 1971 Spatial resolution of a resistance wire temperature sensor. *Phys. Fluids* **14**, 2052–2054.

Chapter 6

Conclusion

6.1 Summary of results

This work investigated the transport and mixing of homogeneous and inhomogeneous scalar fields in a uniformly sheared flow generated in a wind tunnel. The passive scalar fields were superimposed using slightly heated metallic ribbons positioned in the spanwise direction. Simultaneous measurements of velocity, temperature and temperature dissipation statistics were performed using a three-wire cold/hot-wire probe and a quadruple cold-wire probe. The temporal and spatial resolutions of the measurements were sufficient to resolve the fine structures of both the velocity and the scalar fields in our experiments.

The time-averaged properties of the flow and the three scalar fields (UTG, TML and PLS) were investigated. The turbulent flow in this study was free of complications arising from turbulence inhomogeneity, the proximity of walls and external intermittency, while, like most practical flows, it was subjected to turbulence production and strong anisotropy. A comparative analysis of mean temperature, r.m.s. fluctuations, heat fluxes, and triple correlation coefficients variations led to identification of similarities and differences in the three scalar fields. For example, the mean temperature, heat fluxes and triple correlation coefficient profiles across the TML showed resemblance to those across either of the halves of the PLS, if symmetry is taken into consideration. On the other hand, the comparison of r.m.s. fluctuation profiles clearly demonstrated the effects of initial condition in the PLS but not in the TML or UTG. Self-similarity and the evolution of scalar properties were also documented for all scalar fields.

The PDF and JPDF of velocity fluctuations were found to be Gaussian in the USF.

The PDF of scalar fluctuations was also Gaussian in the UTG, but in the TML and PLS the scalar PDFs were distinctly non-Gaussian. The most important observation in the PDFs can be summarized as follows. At the centre of the TML, both tails of the scalar PDF were bounded by values set by the warm and cold streams, whereas at the centre of the PLS the cold tail was bounded, while the warm tail was nearly Gaussian, a phenomenon attributed to sustained temperature fluctuations introduced by the heating source. It was thus concluded that the reasons for the approximate Gaussianity of the scalar PDF in the UTG field and the warm side of the PLS are fundamentally different. Supporting evidence for the presence of sustained initial effects in the PLS was provided by a comparative investigation of velocity-temperature JPDFs, velocity conditional expectations and events with strong transverse velocities in the three scalar fields. In particular, the velocity expectations conditioned on temperature values were found linear in the UTG and strongly non-linear in the TML and the PLS. The non-linearities were different in the two non-homogeneous scalar fields. In the TML, the conditional velocity expectations were inflected so that temperature fluctuations on both the cool and the warm sides were restricted by the temperatures of the two far streams. On the cool side of the PLS, the conditional velocity expectations were similar to those in the TML. In contrast, on the warm side of the PLS, these velocity expectations appeared to be bounded, although the velocity fluctuations themselves had no theoretical bound; this is attributed to the fact that the warmest fluid was likely transported not from distant but nearby locations and from either side of the measuring point, so that the average velocity of warm patches remained relatively small.

The fine structures of the three scalar fields were also investigated by direct measurements of scalar derivatives in the streamwise, transverse and spanwise directions. The form of the distribution of scalar dissipation rate statistics departed clearly from log-normality in all three scalar fields. The low-ε_θ tail of the logarithm of the scalar dissipation PDF in the PLS had higher values than those in the other two scalar fields. The level of anisotropy of the scalar dissipation rate in the UTG was nearly constant for the entire range of scalar fluctuations so that any of its three parts may be used as a surrogate for the total. In the non-homogeneous scalar fields, the transverse part was much stronger than the streamwise and spanwise parts and had a very different shape, which makes the use of one of the three parts as a surrogate of the total inappropriate. Finally, a comparison between the JPDFs of the scalar fluctuations and the scalar dissipation rate with the corresponding marginal PDFs suggested that symmetry of the scalar PDF does not necessarily imply independence of these properties.

6.2 Main contributions

The present study reported high–quality simultaneous measurements of velocity and temperature statistics in passively heated USF. The measurement accuracy of the temperature and its three derivatives was excellent throughout these fields, and the acquisition of extremely long data records allowed the detection of rare velocity-temperature events. Very few previous studies had comparable methodologies.

In this study, for the first time, three different scalar fields were investigated experimentally in the same turbulent flow, so that it was possible to examine scalar transport without concerns for differences among transporting mechanism characteristics. The present results were also capable of separating the effects of external scalar intermittency. The choice of scalar fields was made as to allow one to examine separately and in combination the effects of scalar inhomogeneity and those of initial conditions, namely the extent by which local scalar fluctuations were connected to the apparatus that generated each scalar field.

The results of this study can be used for tests of the accuracy of the mixing models in homogeneous turbulence, and in particular for estimating the errors resulting from the use of the Gaussian approximation. Additionally, the present results can be helpful in the development of new models that account for the effects of initial conditions in scalar fields. Due to technical and time limitations, the effects of turbulent Reynolds number on the dissipation range statistics have not been examined in this study.

6.3 Recommendations for future work

The present study has shed some light on the transport mechanisms that affect the shape of the scalar PDF in inhomogeneous scalar fields in homogeneous turbulence. An apparent extension of this work would be to examine scalar transport in various kinds of inhomogeneous turbulence. For example, it would be interesting to investigate scalar transport in the wake of a heated cylinder in a USF or GT. At the centre of the wake of a heated cylinder in a low–turbulence free stream, Kailasnath *et al.* (1993) showed that the tail of the scalar PDF was nearly Gaussian on the warm side and exponential on the cold side. In the proposed experiment, one would be able to determine the effects of multi–scale turbulence and the return to homogeneity away from the cylinder.

Appendix A

Power spectrum analysis

Figure A.1 presents the one-dimensional power spectrum of the streamwise velocity component. Three distinct ranges can be identified.

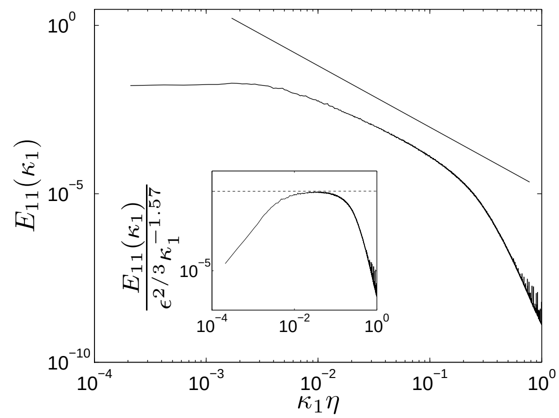

Figure A.1: Power spectrum of the streamwise velocity fluctuations measured at $x_1/h = 10$ as a function of wavenumber normalized by the Kolmogorov microscale; solid line has a slope of $-5/3$; the inset shows the optimal compensated spectrum, with a dashed line added to assist in the determination of the plateau; the ordinates are in arbitrary units.

- At relatively low wavenumbers ($\kappa_1\eta \lesssim 2 \times 10^{-3}$), there is an energy containing range, which is characterized by a relatively flat spectrum.

- At intermediate wavenumbers ($4 \times 10^{-3} \lesssim \kappa_1\eta \lesssim 10^{-1}$), there appears to be an inertial subrange, in which the spectrum decreases at a rate which is not very different from the Kolmogorov value of $-5/3$. As the inset in the same figure illustrates, the optimal spectral slope in this range is -1.57, which is in agreement with previous results in USF experiments at comparable turbulent Reynolds numbers (Ferchichi & Tavoularis, 2000; Garg & Warhaft, 1998).

- At high wavenumbers ($\kappa_1 \eta \gtrsim 10^{-1}$), there is a viscous subrange, which is characterized by an increasing rate of decrease with increasing wavenumber.

References

Adrian, R. J. & Moin, P. 1988 Stochastic estimation of organised turbulent structure: homo-geneous shear flow. *J. Fluid Mech.* **190**, 531–559.

Anselmet, F., Djeridi, H. & Fulachier, L. 1994 Joint statistics of a passive scalar and its dissipation in turbulent flows. *J. Fluid Mech.* **280**, 173–197.

Antonia, R. A. & Mi, J. 1993 Temperature dissipation in a turbulent round jet. *J. Fluid Mech.* **250**, 531–551.

Antonia, R. A. & Van Atta, C.W. 1978 Structure functions of themperature fluctuations in turbulent shear flows. *J. Fluid Mech.* **84**, 561–580.

Ashok, A., Bailey, S C. C., Hultmark, M. & Smits, A. J. 2012 Hot-wire spatial resolution effects in measurements of grid-generated turbulence. *Exp. Fluids* **53**, 1713–1722.

Bailey, S C. C. 2006 The interaction of a wing-tip vortex and free-stream turbulence. PhD thesis, Mechanical Engineering Department, University of Ottawa, Ottawa, Canada.

Bradshaw, P. 1971 *An introduction to turbulence and its measurement*. Pergamon Press, Oxford, New York.

Browne, L. W. B., Antonia & R. A., Chua, L. P. 1989 Calibration of x-probes for turbulent flow measurements. *Exp. Fluids* **7**, 201–208.

Browne, L. W. B. & Antonia, R. A. 1987 The effect of wire length on temperature statistics in a turbulent wake. *Exp. Fluids* **5**, 426–428.

Bruun, H. H. 1995 *Hot wire anemometry: principles and signal analysis*. Oxford Unversity Press, New York.

Budwig, R., Tavoularis, S. & Corrsin, S. 1985 Temperature fluctuations and heat flux in grid generated isotropic turbulence with stressamwise and transverse mean-temperature gradient. *J. Fluid Mech.* **153**, 441–460.

Castaing, B., Gunaratne, G., Kadanoff, L., Libchaber, A. & Heslot, F. 1989 Scaling of hard thermal turbulence in rayleigh-benard convection. *J. Fluid Mech.* **204**, 1–30.

Champagne, F. H., Harris, V. G. & Corrsin, S. 1970 Experiments on nearly homogeneous turbulent shear flow. *J. F* **41** (1), 81–139.

Ching, E. S. C. 1993 Probability densities of turbulent temperature fluctuations. *Phys. Rev. Lett.* **70**, 283286.

Corrsin, S. 1947 Extended application on hot-wire anemometer. PhD thesis, Guggenheim Aeronautical Laboratory, California Institute of Technology, Pasadena, California, USA.

De Souza, F. A., Nguyen, V. D. & Tavoularis, S. 1995 The structure of highly sheared turbulence. *J. Fluid Mech.* **303**, 155–167.

Dimotakis, Paul E. 2005 Turbulent mixing. *Annu. Rev. Fluid Mech.* **37** (1), 329–356.

Dopazo, C. & O'Brien, E. E. 1974 An approach to the autoignition of a turbulent mixture. *Acta Astronautica* **1**, 1239–1266.

Dunn, W. & Tavoularis, S. 2007 The use of curved screens for generating uniform shear at low reynolds numbers. *Exp. in Fluids* **42** (2), 281–290.

Feng, H., Olsen, M, G., Hill, J. C. & Fox, R. O. 2007 Simultaneous velocity and concentration field measurements of passive-scalar mixing in a confined rectangular jet. *Exp. in Fluids* **42**, 847–862.

Ferchichi, M. 1998 Measurement of small-scale statistics and probability density functions in passively heated shear flow. PhD thesis, Mechanical Enginnering Department, University of Ottawa, Ottawa, Canada.

Ferchichi, M. & Tavoularis, S. 1992 Evolution of a thermal mixing layer in uniformly sheared turbulent flow. *Phys. Fluids A* **4**, 997–1006.

Ferchichi, M. & Tavoularis, S. 2000 Reynolds number effects on the fine structure of uniformly sheared turbulence. *Phys. Fluids* **12** (11), 2942–2953.

Ferchichi, M. & Tavoularis, S. 2002 Scalar probability density function and fine structure in uniformly sheared turbulence. *J. Fluid Mech.* **461**, 155–182.

Fox, R. O. 1996 On velocity-conditioned scalar mixing in homogeneous turbulence. *Phy* **8**, 2678–2691.

Garg, S. & Warhaft, Z. 1998 On the small scale structure of simple shear flow. *Phys. Fluids* **10**, 662–673.

Germaine, E., Mydlarski, L. & Cortelezzi, L. 2014 Evolution of the scalar dissipation rate downstream of a concentrated line source in turbulent channel flow. *J. Fluid Mech.* **749**, 227–274.

Gylfason, A., Ayyalasomayajula, S. & Warhaft, Z. 2004 Intermittency, pressure and acceleration statistics from hot-wire measurements in wind-tunnel turbulence. *J. Fluid Mech.* **501**, 213–229.

Gylfason, A. & Warhaft, Z 2004 On higher order passive scalar structure functions in grid turbulence. *Phys. Fluids* **16**, 4012–4019.

Harris, V. G., Graham, J. A. H. & Corrsin, S. 1977 Further experiments in nearly homogeneous turbulent shear flow. *J. Fluid Mech.* **81** (4), 657–687.

Haworth, D.C. 2010 Progress in probability density function methods for turbulent reacting flows. *Progress in Energy and Combustion Science* **36**, 168259.

Holloway, A. G. L. 1989 The effects of curvature on sheared turbulence. PhD thesis, Mechanical Engineering Department, University of Ottawa, Ottawa, Canada.

Holzer, M. & Siggia, E. D. 1994 Turbulent mixing of a passive scalar. *Phys. Fluids* **6**, 1820–1837.

Isaza, J.C. & Collins, L.R. 2009 On the asymptotic behaviour of large-scale turbulence in homogeneous shear flow. *J. Fluid Mech.* **637**, 213–239.

Isaza, J.C., Warhaft, Z. & Collins, L.R. 2009 Experimental investigation of the large-scale velocity statistics in homogeneous turbulent shear flow. *Phys. Fluids* **21**, 065105.

Jayesh & Warhaft, Z. 1992 Probability distribution, conditional dissipation, and transport of passive temperature fluctuations in grid-generated turbulence. *Phys. Fluids A* **4**, 2292–2307.

Jones, F. E. 1995 *Techniques and Topics in Flow Measurement*. CRC Press, Florida.

Kailasnath, P., Sreenivasan, K. R. & Saylor, J. R. 1993 Conditional scalar dissipation rates in turbulent wakes, jets, and boundary layers. *Phys. Fluids A* **5 (12)**, 3207.

Karnik, U. & Tavoularis, S. 1987 Generation and manipulation of uniform shear with the use of screens. *Exp. Fluids* **5**, 247–254.

Karnik, U. & Tavoularis, S. 1989 Measurements of heat diffusion from a continuous line source in a uniformly sheared turbulent flow. *J. Fluid Mech.* **202**, 233–261.

Kida, S. & Tanaka, M. 1994 Dynamics of vortical structures in a homogeneous shear flow. *J. Fluid Mech.* **274** (12), 43–68.

KISLICH-LEMYRE, B. 2002 The large-scale structure of uniformly sheared turbulence and its distortion by a solid wall at rest or in motion. PhD Dissertation, Department of Mechanical Engineering, University of Ottawa, Ottawa, Canada.

KOLMOGOROV, A. N. 1933 *Grundbegriffe der Wahrscheinlichkeitsrechnung*. Springer, Berlin.

LARUE, J. C., DEATON, T. & GIBSON, C. H. 1975 Measurement of high-frequency turbulent temperature. *Rev. Sci. Instrum.* **46**, 757–764.

LARUE, J. C. & LIBBY, P. A. 1981 Thermal mixing layer downstream of half-heated turbulence grid. *Phys. Fluids* **24**, 597–603.

LARUE, J. C., LIBBY, P. A. & SESHADRI, D. V. R. 1981 Further results on the thermal mixing layer downstream of a turbulence grid. *Phys. Fluids* **24**, 1927–1933.

LAVERTU, R. A. & MYDLARSKI, L. 2005 Scalar mixing from a concentrated source in turbulent channel flow. *J. Fluid Mech.* **528**, 135–172.

LEE, M. J., KIM, J. & MOIN, P. 1990 Structure of turbulence at high shear rate. *J. Fluid Mech.* **216**, 561–583.

LEPORE, J. & MYDLARSKI, L. 2011 Lateral dispersion from a concentrated line source in turbulent channel flow. *J. Fluid Mech.* **678**, 417450.

LI, J. D. 2004 Dynamic response of constant temperature hot-wire system in turbulence velocity measurements. *Meas. Sci. Technol.* **15**, 18351847.

LI, J. D. 2006 Dynamic response of constant temperature hot-wire systems under various perturbations. *Meas. Sci. Technol.* **17**, 26652675.

LI, J. D. & BILGER, R. W. 1994 A simple theory of conditional mean velocity in turbulent scalar-mixing layer. *Phys. Fluids* **6**, 605–610.

LI, J. D., MCKEON, B. J., JIANG, W., MORRISON, J. F. & SMITS, A. J. 2004 The response of hot wires in high reynolds-number turbulent pipe flow. *Meas. Sci. Technol.* **15**, 789798.

LOHSE, D. & MULLER-GROELING, A. 1996 Anisotropy and scaling corrections in turbulence. *Phys. Rev. E* **54**, 395405.

LUNDGREN, T. S. 1967 Distribution functions in the statistical theory of turbulence. *Phys. Fluids* **10**, 969–975.

MA, B. & WARHAFT, Z. 1986 Some aspects of the thermal mixing layer in grid turbulence. *Phys. Fluids* **29**, 3114–3120.

MANUAL, A.A.LAB 1996 *Model AN-1003*. A.A. Lab Systems LTD., Ramat-Gan, Isreal.

MI, J. 2006 Correlation between non-gaussian statistics of a scalar and its dissipation rate in turbulent flows. *Phys. Rev. E* **74**, 016301.

MI, J., ANTONIA, R. A. & ANSELMET, F. 1995 Joint statistics between temperature and its dissipation rate components in a round jet. *Phys. Fluids* **7**, 1665–1673.

MYDLARSKI, L. & WARHAFT, Z. 1998 Passive scalar statistics in high-Péclet-number grid turbulence. *J. Fluid Mech.* **358**, 135–175.

PAPOULIS, A. 1991 *Probability, random variables and stochastic processes*. McGraw-Hill, New York.

POPE, S.B. 1985 Pdf methods for turbulent reactive flows. *Prog. Energy Combust. Sci* **11**, 119–192.

POPE, S. 2000 *Turbulent Flows*. Cambridge University Press, New York.

POPE, S. B. 2013 A model for turbulent mixing based on shadow-position conditioning. *Phys. Fluids* **25**, 110803.

POPE, S. B. & CHING, E. S. C. 1993 Stationary probability density functions an exact result. *Phys. Fluids A* **5**, 1529–1531.

ROGERS, M. M. & MOIN, P. 1987 The structure of the vorticity field in homogeneous turbulent flows. *J. Fluid Mech.* **176**, 33–66.

ROHR, J. J., ITSWEIRE, E. C., HELLAND, K. N. & ATTA, C. W. VAN 1988 An investigation of the growth of turbulence in a uniform-mean-shear flow. *J. Fluid Mech.* **187**, 1–33.

ROSE, W. G. 1966 Results of an attempt to generate a homogeneous turbulent shear flow. *J. Fluid Mech.* **25** (1), 97–120.

SHEN, X. & WARHAFT, Z. 2000 The anisotropy of the small scale structure in high reynolds number turbulent shear flow. *Phys. Fluids* **12** (11), 2976–2989.

SINAI, Y. G. & YAKHOT, V. 1989 Limiting probability distributions of a passive scalar in a random velocity field. *Phys. Rev. Lett.* **63**, 19621964.

SMITS, A. J., MONTY, J., HULTMARK, M., BAILEY, S. C. C., HUTCHINS, N. & MARUSIC, I. 2011 Spatial resolution correction for wall-bounded turbulence measurements. *J. Fluid Mech.* **676**, 41–53.

SREENIVASAN, K. R. 1991 On the local isotropy of the passive scalars in turbulent shear flows. *Proc. R. Soc. London. Ser. A* **241**, 165–82.

Sreenivasan, K. R. & Antonia, R. A. 1977 Skewness of the temperature derivatives in turbulent shear flows. *Phys. Fluids* **20**, 1986–1988.

Sreenivasan, K. R. & Antonia, R. A. 1997 The phenomenology of small-scale turbulence. *Annu. Rev. of Fluid Mech.* **29**, 435–472.

Sreenivasan, K. R. & Tavoularis, S. 1980 On the skewness of the temperature derivative in turbulent flows. *J. Fluid Mech.* **101**, 783–795.

Sreenivasan, K. R., Tavoulatis, S. & Corrsin, S. 1982 A test of gradient transport and ita generalizations. In *Turbulent shear flows 3, the third International Symposium on Turbulent Shear Flows , Davis, CA, USA*.

Swaminathan, N. & Bray, K. N. C. 2011 *Turbulent premixed flames*. Cambridge University Press, New York.

Tatarskii, V. I., Dubovikov, M. M., Praskovsky, A. A. & Karyakin, M. Yu. 1992 Temperature fluctuation spectrum in the dissipation range for statistically isotropic turbulent flow. *J. Fluid Mech.* **238**, 683–698.

Tavoularis, S. 1978 A circuit for the measurement of instantanious temperature in heated turbulent flows. *J. Phys. E: Sci. Instrum.* **11**, 21–23.

Tavoularis, S. 1983 Simple corrections for the temperature sensitivity of hot wires. *Rev. Sci. Instrum.* **54**, 741–743.

Tavoularis, S. 1985 Asymptotic laws for transversely homogeneous turbulent shear flows. *Phys. Fluids* **28** (3), 999–1001.

Tavoularis, S. 2005 *Measurement in Fluid Mechanics*. Cambridge University Press, New York.

Tavoularis, S. & Corrsin, S. 1981*a* Experiments in nearly homogeneous turbulent shear flow with a uniform mean temperature gradient. Part 1. *J. Fluid Mech.* **104**, 311–347.

Tavoularis, S. & Corrsin, S. 1981*b* Experiments in nearly homogeneous turbulent shear flow with a uniform mean temperature gradient. Part 2. *J. Fluid Mech.* **104**, 349–367.

Tavoularis, S. & Karnik, U. 1989 Further experiments on the evolution of turbulent stresses and scales in uniformly sheared turbulence. *J. Fluid Mech.* **204**, 457–478.

Taylor, G. I. 1935 Statistical theory of turbulence. *Proceedings of the Royal Society of London. Series A, Mathematical and Physical* **151**, 421–444.

Tong, C. & Warhaft, Z. 1994 On passive scalar derivative statistics in grid turbulence. *Phys. Fluids* **6**, 2165–2176.

Vanderwel, Christina & Tavoularis, Stavros 2011 Coherent structures in uniformly sheared turbulence. *J. Fluid Mech.* **689**, 434–464.

Villermaux, J. & Devillon, J. C. 1972 Representation de la coalescence et de la redispersion des domaines de segregation dans un fluide par un modele d'interaction phenomenologique. In *In Proceedings of the Second International Symposium on Chemical Reaction Engineering*.

Vukoslavcevic, P. & Wallace, J. M. 2002 The simultaneous measurement of velocity and temperature in heated turbulent air flow using thermal anemometry. *Meas. Sci. Technol.* **13**, 1615–1624.

Warhaft, Z. 2000 Passive scalars in turbulent flows. *Annu. Rev. Fluid Mech.* **32** (1), 203–240.

Warhaft, Z. & Shen, X. 2002 On the higher order mixed structure functions in laboratory shear flow. *Phys. Fluids* **14**, 2432–2438.

Williams, F. A. 1965 *Combustion theory: the fundamental theory of chemically reacting flow systems*. Addison-Wesley Publishing Company.

Wyngaard, J. C. 1971 Spatial resolution of a resistance wire temperature sensor. *Phys. Fluids* **14**, 2052–2054.